UNIVERSIDADE FEDERAL DO CEARÁ
CENTRO DE CIÊNCIAS
DEPARTAMENTO DE QUÍMICA ANALÍTICA E FÍSICO-QUÍMICA
PROGRAMA DE PÓS-GRADUAÇÃO EM QUÍMICA

ANA ALINE COÊLHO ALCANFOR

ESTUDO DA ELETRODEPOSIÇÃO DE ANTIMÔNIO E ESTANHO-ANTIMÔNIO EM MEIO DE CLORETO DE COLINA E ETILENOGLICOL

FORTALEZA
2024

ANA ALINE COÊLHO ALCANFOR

ESTUDO DA ELETRODEPOSIÇÃO DE ANTIMÔNIO E ESTANHO-ANTIMÔNIO EM MEIO DE CLORETO DE COLINA E ETILENOGLICOL

Tese apresentada ao Programa de Pós-Graduação em Química, do Centro de Ciências, da Universidade Federal do Ceará, como parte dos requisitos para obtenção do título de Doutora em Química. Área de concentração: Físico-Química.

Orientador: Prof. Dr. Pedro de Lima-Neto.

FORTALEZA

2024

Dados Internacionais de Catalogação na Publicação
Universidade Federal do Ceará
Sistema de Bibliotecas
Gerada automaticamente pelo módulo Catalog, mediante os dados fornecidos pelo(a) autor(a)

A317e Alcanfor, Ana Aline Coelho.
Estudo da eletrodeposição de antimônio e estanho-antimônio em meio de cloreto de colina e etilenoglicol / Ana Aline Coelho Alcanfor. – 2023.
122 f. : il. color.

Tese (doutorado) – Universidade Federal do Ceará, Centro de Ciências, Programa de Pós-Graduação em Química, Fortaleza, 2023.
Orientação: Prof. Dr. Pedro de Lima-Neto.

1. Sb. 2. SnxSb(1-x). 3. Eletrodeposição. 4. Corrosão. 5. Modelagem Molecular. I. Título.
CDD 540

ANA ALINE COÊLHO ALCANFOR

ESTUDO DA ELETRODEPOSIÇÃO DE ANTIMÔNIO E ESTANHO-ANTIMÔNIO EM MEIO DE CLORETO DE COLINA E ETILENOGLICOL

Tese apresentada ao Programa de Pós-Graduação em Química, do Centro de Ciências, da Universidade Federal do Ceará, como parte dos requisitos para obtenção do título de Doutora em Química. Área de concentração: Físico-Química.

Aprovada em: 13/12/2024.

BANCA EXAMINADORA

Prof. Dr. Pedro de Lima-Neto (Orientador)
Universidade Federal do Ceará (UFC)

Profa. Dra. Adriana Nunes Correia
Universidade Federal do Ceará (UFC)

Profa. Dr. Antoninho Valentini
Universidade Federal do Ceará (UFC)

Prof. Dr. Walney Silva Araújo
Universidade Federal do Ceará (UFC)

Prof. Dr. Francisco Wirley Paulino Ribeiro
Universidade da Integração Internacional da Lusofonia Afro-Brasileira (UNILAB)

A Deus.

Aos meus pais, Moisés e Luzia.

Aos meus irmãos, Ana Alice e Júnior.

E à minha tia Maria Coelho (*in memoriam*).

AGRADECIMENTOS

Neste momento de vitória pela conquista do meu doutorado, quero agradecer especialmente a Deus e à Virgem Maria. Obrigada, Senhor, por me iluminar com sabedoria e graça durante a realização deste trabalho, e à minha Mãe Maria Santíssima, por sua proteção. Esta conquista é a prova de que, com fé e perseverança, tudo é possível.

Aos meus queridos pais, Moisés e Luzia, pessoas honestas e íntegras, que me ensinaram a trilhar caminhos retos e a sempre confiar na misericórdia divina, agradeço por serem meu alicerce e meus maiores exemplos de fé, força, caráter, trabalho, responsabilidade e honestidade. Cada sacrifício que fizeram e cada palavra de encorajamento me motivaram a seguir em frente, mesmo nos momentos mais difíceis. Sou eternamente grata por tudo o que me ensinaram e por sempre estarem ao meu lado. Esta conquista é para vocês.

Aos meus familiares: meus irmãos Ana Alice e Júnior, minha amada tia Maria Coelho (*in memoriam*), minha tia Dinha, minha avó Alice, meus tios, meus primos, meus cunhados: Miriam e Douglas, e meus amados sobrinhos: Ana Virna, Ruan Pablo, Ana Luiza, Ana Beatriz, José Ravi, Luiz Felipe e meu sobrinho-neto Henri Emanuel, agradeço por serem meu incentivo e motivação.

Ao meu orientador, Prof. Dr. Pedro de Lima-Neto, agradeço por sua valiosa orientação, sabedoria, confiança e paciência, que foram fundamentais ao longo de toda a minha jornada acadêmica. Sou eternamente grata por tê-lo como orientador no mestrado e no doutorado.

À Profa. Dra. Adriana Correia, agradeço por acreditar em mim e por me guiar em cada etapa final deste processo. Sua dedicação, disponibilidade e paciência fizeram toda a diferença e me ajudaram a superar os desafios que enfrentei. Sou eternamente grata por tudo o que a senhora fez por mim e por minha família.

Agradeço ao Prof. Dr. Paulo Naftali pelos ensinamentos acadêmicos, pelo apoio no laboratório e pelas valiosas contribuições aos experimentos e resultados de corrosão (polarização e espectroscopia de impedância eletroquímica), essenciais para a obtenção do segundo manuscrito.

Expresso minha gratidão ao Grupo de Eletroquímica e Corrosão (GELCORR) da UFC pela oportunidade de integrar o laboratório, cuja convivência foi essencial para meu crescimento acadêmico, profissional e pessoal.

Aos alunos de graduação e pós-graduação com os quais colaborei – Emanuelle Marinho, Juliermes Pereira, Daniela Mirela, Ronnie Semedo, Deomar Nogueira, Matheus

Vasconcelos, Wanderson Crisóstomo, Gabrielle Abreu e João Francisco – agradeço pelas valiosas trocas de aprendizado.

De forma especial, agradeço às colegas Raissa Costa e Natalia Gomes pelo empenho incansável na realização dos experimentos finais, que tornaram possível a publicação dos artigos desta tese. Vocês foram fundamentais para essa conquista. Muito obrigada.

A todos os colegas com quem compartilhei momentos de amizade e conhecimento no GELCORR – Stefane, Mel, David, Joelson, Janevane, Alexandre e tantos outros que guardo em minha memória, obrigada.

Ao Prof. Dr. Othon Souto Campos pela paciência, sugestões e ensinamentos compartilhados ao longo dessa jornada, muito obrigada.

Aos meus amigos Ana Maria, Aurélio, Gabriel, Rodolfo, Diego, Flaviana, Salete, Ana Paula, Pedro, Franqueline, Raul, Henrique, Gabriela, Yara, Chiara, Joshua, Luis Gustavo, Letícia, Mateus, Alano, Selma, Beatriz, Alcides, Elisa, Gabriele e Luciana, agradeço imensamente pelo apoio, incentivo e amizade ao longo dessa jornada.

Ao Grupo de Química Teórica (GQT) da UFC, ao Prof. Dr. Norberto Monteiro e ao aluno Leonardo Silva, pelos cálculos computacionais do primeiro manuscrito.

À Central Analítica-UFC/CT-INFRA/MCTI-SISNANO/Pró-Equipamentos CAPES, pelos experimentos de Microscopia Eletrônica de Varredura e de Energia Dispersiva de Raios-X.

Ao Laboratório de Raios-X (LRX) da UFC, agradeço ao Prof. Dr. Sasaki e à técnica Isabela Oliveira pelas análises de Difração de Raios-X.

À Central Multiusuário de Pesquisa em Materiais e Biossistemas (CeMatBio) da Universidade Federal do Maranhão, ao Prof. Dr. Alan Menezes pelas análises de Difração de Raios-X.

Ao Laboratório de Caracterização de Materiais (LACAM) da UFC, ao Prof. Dr. Hamilton Abreu e ao técnico Édipo Silva pelas análises de Difração de Raios-X.

Agradeço ao Prof. Dr. Antoninho Valentini, ao Prof. Dr. Tércio Paulo e ao Prof. Dr. Paulo Naftali pela disponibilidade e pelas contribuições durante minha qualificação de doutorado.

Agradeço à Profa. Dra. Adriana Correia, ao Prof. Dr. Antoninho Valentini, ao Prof. Dr. Walney Silva e ao Prof. Dr. Wirley Ribeiro pela disponibilidade e pelas valiosas contribuições na defesa de tese.

Agradeço ao Departamento de Química Analítica e Físico-Química (DQAFQ), ao Programa de Pós-Graduação em Química (PGQUIM) e a todos os professores do programa.

Agradeço à Universidade Federal do Ceará pelos recursos humanos, estruturais e financeiros que tornaram possível a realização deste doutorado.

O presente trabalho foi realizado com apoio da Coordenação de Aperfeiçoamento de Pessoal de Nível Superior – Brasil (CAPES) – Código de Financiamento 001.

Agradeço à CAPES pela concessão da bolsa de doutorado, que possibilitou minha dedicação integral à pesquisa, contribuindo para minha formação acadêmica e para o avanço da ciência e educação no Brasil.

Agradeço a todos os professores que fizeram parte da minha trajetória, desde a educação infantil até o ensino superior.

Por fim, agradeço de coração a todos que, direta ou indiretamente, fizeram parte dessa jornada. Muito obrigada!

“Tudo posso naquele que me fortalece.”

Filipenses 4:13.

RESUMO

Este trabalho objetivou investigar o efeito da adição de água e da temperatura na eletrodeposição de antimônio (Sb) sobre platina (Pt), bem como a influência da composição da solução eletrolítica na eletrodeposição conjunta de estanho e antimônio ($Sn_xSb_{(1-x)}$) sobre substrato de cobre (Cu). As resistências à corrosão dos eletrodepósitos $Sn_xSb_{(1-x)}$ foram investigadas em meio de NaCl 0,1 mol L^{-1}. Todos os eletrodepósitos foram obtidos utilizando soluções eletrolíticas baseadas na mistura de cloreto de colina (ChCl) e etilenoglicol (EG). A morfologia, a estrutura cristalina e a composição química dos eletrodepósitos foram analisadas por Microscopia Eletrônica de Varredura (MEV), Difração de Raios X (DRX) e Espectroscopia por Dispersão de Elétrons (EDS), respectivamente. Adicionalmente, foram conduzidos estudos computacionais para compreender as interações entre os íons Sb^{3+} e os demais componentes das soluções eletrolíticas, empregando os métodos computacionais de Dinâmica Molecular (DM) e Teoria Quântica de Átomos em Moléculas (QTAIM). Os resultados voltamétricos dos íons Sb^{3+} indicaram que o aumento no teor de água do eletrólito catalisou a redução das espécies. Os eletrodepósitos obtidos na ausência e na presença de água apresentam diferentes morfologias. As simulações de DFT indicaram que a interação Sb-Cl é mais forte, o que sugere a formação de complexos Sb-Cl. A adição de H2O favorece a afinidade eletrônica dos sistemas, e os resultados de QTAIM sugerem que este aditivo diminuiu a densidade eletrônica dos íons Sb^{3+}. Para os eletrodepósitos de $Sn_xSb_{(1-x)}$, as imagens MEV revelaram que os revestimentos exibiram grãos e aglomerados. Os resultados de DRX indicaram a formação das fases SbSn, como Cu_2Sb, Cu_6Sn_5 e $Cu_6(Sn,Sb)_5$. As curvas de polarização potenciodinâmicas (PP) mostraram que todas as ligas de $Sn_xSb_{(1-x)}$ apresentaram uma região de dissolução ativa, seguida por uma região passiva. Os testes de imersão foram realizados por 24 h, e os resultados de DRX revelaram as fases Cu, Sn, SnO, SbSn e Sb_2O4. Para as amostras imersas por 48 h, as fases Cu, CuSn, SnO_2 e SnSb foram identificadas. Os valores de resistência à polarização (Rp) de 4.60, 14.69, 1.81 kΩ cm^2 foram alcançados para Sn, $Sn_{77}Sb_{23}$ e $Sn_{37}Sb_{63}$, respetivamente. Para os revestimentos $Sn_{77}Sb_{23}$, Sn e $Sn_{37}Sb_{63}$, os valores obtidos das respectivas resistências à transferência de carga (Rtc), obtidas por espectroscopia de impedância eletroquímica, foram: 10.5, 1.15 e 1.46 kΩ cm^2. Portanto, estes resultados mostram que a camada $Sn_{77}Sb_{23}$ é a mais resistente à corrosão.

Palavras-chave: Sb; $Sn_xSb_{(1-x)}$; eletrodeposição; corrosão; modelagem molecular.

ABSTRACT

The objective of this study was to investigate the effect of the addition of water and temperature on the electrodeposition of antimony (Sb) on platinum (Pt), as well as the influence of the composition of the electrolyte solution on the joint electrodeposition of tin and antimony ($Sn_xSb_{(1-x)}$) on copper (Cu) substrate. The corrosion resistance of the $Sn_xSb_{(1-x)}$ electrodeposits was investigated in 0.1 mol L^{-1} NaCl medium. All electrodeposits were obtained using electrolyte solutions based on the mixture of choline chloride (ChCl) and ethylene glycol (EG). The morphology, crystal structure and chemical composition of the electrodeposits were analyzed by Scanning Electron Microscopy (SEM), X-ray Diffraction (XRD) and Electron Scattering Spectroscopy (EDS), respectively. Additionally, computational studies were conducted to understand the interactions between Sb^{3+} ions and the other components of electrolyte solutions, using the computational methods of Molecular Dynamics (MD) and Quantum Theory of Atoms in Molecules (QTAIM). The voltammetric results of the Sb^{3+} ions indicated that the increase in the water content of the electrolyte catalyzed the reduction of the species. The electrodeposits obtained in the absence and presence of water have different morphologies. The DFT simulations indicated that the Sb-Cl interaction is stronger, which suggests the formation of Sb-Cl complexes. The addition of H_2O favors the electron affinity of the systems, and the QTAIM results suggest that this additive decreased the electron density of the Sb^{3+} ions. For the $Sn_xSb_{(1-x)}$ electrodeposits, SEM images revealed that the coatings exhibited grains and agglomerates. The XRD results indicated the formation of SbSn phases, such as Cu_2Sb, Cu_6Sn_5 and $Cu_6(Sn,Sb)_5$. The potentiodynamic (PP) polarization curves showed that all $Sn_xSb_{(1-x)}$ alloys had an active dissolution region, followed by a passive region. Immersion tests were performed for 24 h, and XRD results revealed Cu, Sn, SnO, SbSn, and Sb_2O_4 phases. For the samples immersed for 48 h, the Cu, CuSn, SnO_2 and SnSb phases were identified. Polarization resistance (R_p) values of 4.60, 14.69, 1.81 kΩ cm^2 were achieved for Sn, $Sn_{77}Sb_{23}$ and $Sn_{37}Sb_{63}$, respectively. For the coatings $Sn_{77}Sb_{23}$, Sn and $Sn_{37}Sb_{63}$, the values obtained from the respective charge transfer strengths (R_{tc}), obtained by electrochemical impedance spectroscopy, were: 10.5, 1.15 and 1.46 kΩ cm^2. Therefore, these results show that the $Sn_{77}Sb_{23}$ layer is the most resistant to corrosion.

Keywords: Sb; $Sn_xSb_{(1-x)}$; electroplating; corrosion; molecular modeling.

SUMÁRIO

1 INTRODUÇÃO

A eletrodeposição é uma técnica praticada há anos sendo reconhecida por sua versatilidade para as mais diversas aplicações. Esta técnica permite a formação de revestimentos com fins decorativos, para proteção contra corrosão, além de peças cromadas para uso automotivos, joias banhadas com metais nobres, como ouro, prata, platina e suas ligas, entre outros. Tradicionalmente, os eletrólitos formulados para o processo de eletrodeposição são obtidos a partir de soluções aquosas, que em sua grande maioria necessitam do uso de agentes complexantes para promover a estabilidade das espécies em solução, garantindo assim, um bom acabamento do revestimento. No entanto, alguns dos agentes complexantes são a base de cianeto o que resulta em soluções eletrolíticas prejudiciais para a saúde dos operadores e para o meio ambiente (GAMBURG; ZANGARI, 2011).

Assim, a substituição de eletrólitos aquosos por meios não aquosos é necessária para a otimização dos processos de eletrodeposição, considerando questões de segurança e ambientais. Nesse contexto, os solventes eutéticos têm ganhado destaque nas aplicações eletroquímica. Os solventes eutéticos representam uma nova geração de solventes verdes, caracterizados por seu fácil preparo, baixo custo, amplo intervalo eletroquímico, boa solvatação de sais e elevada condutividade iônica, o que os torna particularmente interessantes para aplicações eletroquímicas. Além disso, sua natureza ambientalmente amigável tem motivado um número crescente de pesquisas científicas e a adoção desses solventes (ABBOTT, 2022; DE OLIVEIRA VIGIER; JÉRÔME, 2019; PERNA; VITALE; CAPRIATI, 2020; RAMÓN, DIEGO J.; GUILLENA, 2019; TOMÉ *et al*., 2018).

Este trabalho está organizado em três seções. A primeira seção apresenta uma breve visão geral sobre os solventes eutéticos e suas aplicações em eletroquímica, principalmente direcionados ao processo de eletrodeposição. Discute-se a influência da adição de aditivos e água ao solvente eutético, bem como os principais aspectos que têm sido considerados na eletrodeposição de metais e ligas, além do uso de simulações computacionais para uma compreensão teórica do sistema experimental. Na segunda seção, é apresentado um manuscrito sobre o estudo da influência da adição de água no processo de eletrodeposição de antimônio a partir de uma abordagem experimental e teórica. Na terceira e última seção, são apresentados os resultados da investigação de Sn e $Sn_xSb_{(1-x)}$ eletrodepositados sobre substrato de cobre e estuda-se à resistência a corrosão dos revestimentos. É importante destacar que essas pesquisas foram conduzidas com sucesso em meio de solventes eutéticos. Por fim, são apresentadas as conclusões desta pesquisa.

1.1 Solventes eutéticos

O termo solventes eutéticos profundos, do inglês, *Deep Eutectic Solvents (DES)*, foi relatado pela primeira vez por Abbott e colaboradores para descrever uma nova geração de solventes verdes. Os *DES* são também considerados uma nova classe de líquidos iônicos (LI), por compartilharem características e propriedades semelhantes, como por exemplo: baixa pressão de vapor, alta estabilidade térmica, boa condutividade, entre outras. No entanto, os *DES* e os líquidos iônicos são dois tipos diferentes de solventes. Um líquido iônico é considerado como um composto formado exclusivamente de espécies iônicas, ou seja, pela associação de um cátion e um ânion, enquanto o *DES* é a combinação de dois ou mais componentes que, quando misturados em uma proporção molar adequada, formam uma mistura eutética líquida a uma temperatura de fusão inferior as dos seus componentes individuais. Além disso, a mistura é chamada de eutética por conta do ponto de fusão, a uma dada composição (ou fração) molar e possuir temperatura de fusão constante cuja composição não pode ser separada termicamente. O diagrama de fases temperatura-composição para os componentes fundamentais do DES é mostrado na Figura 1 (ABBOTT *et al*., 2001, 2003, 2004; RAMÓN, DIEGO J.; GUILLENA, 2019).

Figura 1 – Diagrama temperatura-fração molar dos componentes de um solvente eutético, em que a mistura do HBA (*hydrogen bond aceptor*, ou recebedor da ligação de hidrogênio) e HBD (*Hydrogen bond donator*, ou doador de ligação de hidrogênio) formam, a uma dada composição, um valor de temperatura de fusão constante.

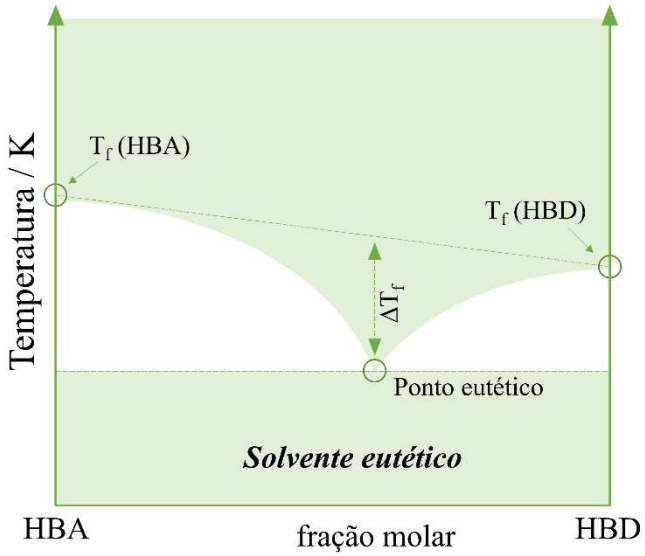

Fonte: Elaborada pela autora.

Em uma revisão posterior, a definição de *DES* e líquidos iônicos foi ampliada de forma a incluir a extensa variedade de espécies que podem formar ligações de hidrogênio. Com isso, o conceito de *DES* evoluiu e é agora considerado como compostos formados a partir de misturas eutéticas de ácidos e bases de Lewis ou de Brønsted, incorporando também diversas espécies aniônicas e/ou catiônicas. Dessa forma, os *DES* podem ser preparados a partir da mistura de dois ou mais componentes que interagem entre si por meio de ligações de hidrogênio, geralmente, formadas entre um aceitador de ligações de hidrogênio, do inglês, *Hydrogen Bond Aceptor* (HBA) e um doador de ligações de hidrogênio, do inglês, Hydrogen Bond Donor (HBD) (ABO-HAMAD *et al.*, 2015; GARCÍA-ÁLVAREZ, 2015; KUDŁAK; OWCZAREK; NAMIEŚNIK, 2015; LI; ROW, 2016; MARTINS; PINHO; COUTINHO, 2019; MBOUS *et al*., 2017; RAMÓN, DIEGO J.; GUILLENA, 2019; SMITH; ABBOTT; RYDER, 2014; TANG; ZHANG; ROW, 2015).

Em geral, os *DES* podem ser classificados de acordo com o HBA e HBD e ser descrito pela fórmula padrão (Cat^+X^-zY), em que o Cat^+ refere-se principalmente ao cátion amônio, mas também pode ser cátion fosfônio ou sulfônio, o X é um ânion haleto que funciona como uma base de Lewis, X e Y (um ácido de Lewis ou base de Brønsted) se combinam para gerar as espécies aniônicas complexas e por fim, a quantidade de moléculas de Y que interagem com o ânion é representada pelo símbolo *z*. De acordo com as definições mais recentes, os *DES* podem ser classificados em cinco tipos conforme a natureza dos seus constituintes. Os *DES* do tipo I, representados por $zMCl_x$ podem ser feitos a partir de sais de amônio quaternário e haletos metálicos; os do tipo II, $MCl_x{\cdot}zH_2O$, podem combinados de sais de amônio quaternário e haletos metálicos hidratados; os do tipo III, *z*RZ, sais de amônio quaternário e doadores de ligações de hidrogênio (HBDs); os do tipo IV, haletos metálicos e doadores de ligações de hidrogênio (HBDs); e por último, os *DES* do tipo V, formados exclusivamente pela mistura de um aceitador de ligações de hidrogênio (HBA) e um doador de ligações de hidrogênio (HDB). Entre os aceitadores de ligações de hidrogênio, o cloreto de colina, do inglês, *choline chloride (ChCl)* se destaca e é um dos componentes mais utilizados para produzir *DES*. O *ChCl* quando misturado com doadores de ligações de hidrogênio tem a capacidade de solvatar uma ampla gama de espécies de metais e metais de transição, incluindo cloretos e óxidos. Vale destacar que o cloreto de colina é um sal barato, biodegradável e não tóxico (ABBOTT *et al*., 2004; KUDŁAK; OWCZAREK; NAMIEŚNIK, 2015; LI; ROW, 2016; SMITH; ABBOTT; RYDER, 2014).

Tabela 1 – Fórmula geral para classificação dos DES em função do seu tipo.

Tipos	**Fórmula geral**	**Exemplo**
I	$Cat^+X^- + zMCl_x$	$ChCl + ZnCl_2$
II	$Cat^+X^- + MCl_x{\cdot}zH_2O$	$ChCl + CoCl_2{\cdot}6H_2O$
III	$Cat^+X^- + zRZ$	ChCl + Ureia
IV	$MCl_x + zRZ$	$ZnCl_2$ + Ureia
V	HBAs + HBDs	Timol + Mentol 1:1

Fonte: Elaborada pela autora.

Os *DES* são de fácil síntese e apresentam baixo custo de produção. Além disso, a possibilidade de ajustar suas propriedades os torna candidatos ideais para serem usados em uma ampla gama de aplicações. Apesar dos *DES* exibirem propriedades semelhantes aos líquidos iônicos, os *DES* são biodegradáveis e seguros, e economicamente mais baratos que os componentes necessários para a fabricação de líquidos iônicos. Com essas vantagens e características, os *DES* têm sido empregados em inúmeras aplicações, incluindo síntese, extração e eletroquímica. Além do crescente interesse em aplicações modernas, como em células solares, dispositivos de armazenamento de energia e obtenção de eletrocatalisadores. Na literatura há um expressivo número de excelentes artigos publicados sobre os *DES* e suas aplicações, a maioria referenciados nesta introdução (ABO-HAMAD *et al*., 2015; AZZOUZ; HAYYAN, 2023; GARCÍA-ÁLVAREZ, 2015; HANSEN *et al*., 2021; LI; ROW, 2016; MBOUS *et al*., 2017; Q. ZHANG, K. DE OLIVEIRA VIGIER, S. ROYER, 2012; SMITH; ABBOTT; RYDER, 2014; TANG; ZHANG; ROW, 2015; TROTER *et al*., 2016; WAGLE; ZHAO; BAKER, 2014).

Entre as áreas de pesquisa que utilizam os *DES* como solventes, a eletroquímica se destaca e apresenta um número crescente de publicações científicas. Isso se deve ao fato das características atrativas dos *DES* como solventes para o uso em eletroquímica, dentre as quais pode-se citar: alta condutividade iônica, amplo intervalo eletroquímico, boa solubilidade de íons metálicos, boa estabilidade térmica, baixo custo e fácil preparação. Além dos principais atributos para aplicações em eletroquímica, que são: os *DES* são solventes verdes e ambientalmente amigáveis, o que proporciona segurança aos operadores e diminui a quantidade de efluentes tóxicos lançados ao meio ambiente. São essas qualidades, que o torna um solvente promissor como alternativas verdes para a substituição de solventes convencionais empregados em eletroquímica.

1.2 Solventes eutéticos e o uso em eletroquímica

Em eletroquímica, a deposição de metais e ligas para a obtenção de revestimentos de superfícies é uma prática bem estabelecida e diversos processos são utilizados de modo a alcançar uma variedade de revestimentos com diferentes características e finalidades, desde decoração à proteção contra corrosão. No entanto, quando o processo de eletrodeposição é conduzido em meio aquoso, algumas limitações são encontradas. E embora a água tenha sido a escolha mais comum para formulação de eletrólitos de galvanização, alguns interferentes dificultam esse processo e devem ser considerados. Entre os principais inconvenientes em eletrólitos aquosos, pode-se citar: intervalo de potencial eletroquímico restrito, reatividade da água a metais específicos e a alta evolução de hidrogênio em potenciais de eletrodeposição negativos, o que compromete diretamente a eficiência do processo e provoca efeitos deletérios ao revestimento. Para contornar essas dificuldades encontradas em banhos aquosos, o uso de agentes complexantes como o íon cianeto tem sido utilizado para manter a estabilidade espécies eletroativas em solução (ABBOTT *et al*., 2015; BERNASCONI *et al*., 2017; SUDAGAR; LIAN; SHA, 2013; XUE; ZHAO; MU, 2019).

Nessa perspectiva, os *DES* são uma classe de solventes promissora para contornar todos esses problemas encontrados em sistemas aquosos. Além disso, os *DES* possuem características que afetam diretamente na composição e morfologia dos eletrodepósitos obtidos, o que consequentemente contribui para uma melhoria nas propriedades finais dos revestimentos, desde aplicações para proteção contra a corrosão, bem como aplicações em tecnologias modernas. No entanto, para o uso de *DES* como solventes em eletroquímica, alguns parâmetros operacionais devem ser ajustados de modo a garantir um processo de eletrodeposição viável nesse meio. Entre os principais parâmetros em meio de *DES*, pode-se destacar: temperatura, viscosidade, condutividade e o uso água e de aditivos no banho eletroquímico.

Dessa forma, dentre os parâmetros que influenciam a eletrodeposição de metais em meio de *DES*, a temperatura, a viscosidade e a condutividade têm sido exaustivamente investigadas devido à sua relevância prática e industrial na eletrodeposição de metais e ligas. Os *DES* apresentam elevada viscosidade em temperatura ambiente, o que pode ser atribuída à presença de extensas redes de ligações de hidrogênios entre os seus constituintes. Um dos efeitos práticos da elevada viscosidade dos *DES* é a menor mobilidade das espécies eletroquímicas em solução. Devido ao seu potencial como meio verde, o desenvolvimento de soluções baseadas em *DES* com baixa viscosidade é altamente desejável. Nesse sentido, a

influência da temperatura na eletrodeposição em meio de *DES* tem sido investigada em inúmeros trabalhos. Uma vez que o aumento da temperatura do sistema leva a uma diminuição da viscosidade, resultando em um aumento significativo da condutividade elétrica e da mobilidade dos íons no meio. O aumento da temperatura pode ainda influenciar na morfologia dos revestimentos obtidos. Em temperaturas mais altas a taxa de crescimento do eletrodepósito é elevada, favorecendo o crescimento de grãos na superfície do eletrodo (ABBOTT *et al.*, 2014; ALCANFOR *et al*., 2017; LI; ROW, 2016; RU *et al*., 2015; XIE *et al*., 2016).

1.3 O uso de aditivos e água nos solventes eutéticos

O uso de aditivos em eletrodeposição pode influenciar em várias propriedades dos eletrodepósitos, como tamanho de grão, brilho e composição química. Em *DES*, o uso de aditivos para melhorar a eletrodeposição de metais e ligas tem sido amplamente descrito na literatura. E entre os mais utilizados, pode-se citar: os aditivos moleculares (ácido nicotínico, nicotinato de metila, 5,5-dimetilhidantoína e ácido bórico); aditivos contendo amina (tioureia, amônia, etilenodiamina); e aditivos quelantes (EDTA, HEDTA e Idranal VII). Além do uso de surfactantes, como CTAB e SDS. A influência da água como aditivo também foi amplamente investigada. (ABBOTT *et al*., 2017; BEZERRA-NETO *et al*., 2018, 2020; MESSIER, 1994; PEREIRA *et al*., 2012; SONG *et al*., 2017; STEFANOVIC *et al*., 2017; ZHEKENOV *et al*., 2017).

1.4 O uso de simulação computacional em solventes eutéticos

Com a rápida evolução dos *DES* e sua ampla gama de aplicações em diversas áreas, tais como, nanotecnologia, eletroquímica, transformação de biomassa, produtos farmacêuticos, tecnologia de membrana, desenvolvimento de biocompósitos, impressão 3D moderna e muitos outros. A compreensão da relação fundamental entre a estrutura e as propriedades dos *DES* permitiu novas abordagens em técnicas de simulação computacional, fornecendo uma abordagem frutífera com inúmeros trabalhos na literatura. O emprego de simulação computacional para o entendimento do *DES* pode prever e revelar mecanismos físicos e serem facilmente vinculadas a experimentos. Assim, teoria e prática podem ser aliadas para o entendimento dos solventes eutéticos e o meio em que está sendo aplicado (AMORIM *et al*., 2023; BEZERRA-NETO *et* al., 2018, 2020; BEZERRA *et al*., 2022, 2024; KOVÁCS *et al*., 2020; PERKINS; PAINTER; COLINA, 2014; PINHEIRO *et al*., 2023; SOUSA *et al*., 2023;

TOLMACHEV *et al*., 2022; VELEZ; ACEVEDO, 2022; VERÍSSIMO DE OLIVEIRA *et al*., 2022).

1.5 Eletrodeposição de ligas meio em solventes eutéticos e suas aplicações

Em eletroquímica, a eletrodeposição de ligas é importante porque as ligas geralmente possuem propriedades superiores às dos metais individuais. A obtenção de revestimentos de ligas em relação aos seus elementos separados pode apresentar características de ser mais resistentes à corrosão, além de apresentar melhores propriedades catalíticas, por exemplo. Assim, o empenho na eletrodeposição de ligas em meio de *DES* está aumentando, especialmente porque o número de combinações de ligas é vasto. Em meio de *DES* já foram relatadas a obtenção de ligas binárias, ternárias e quartenárias, além da obtenção de ligas multicomponentes. Os parâmetros de eletrodeposição de ligas são semelhantes aos dos metais puros, e as características físicas e químicas dependem de fatores experimentais como composição do banho, a densidade de corrente aplicada, o sobrepotencial e temperatura de trabalho. Além disso, a aplicação da eletrodeposição pulsada e eletrodeposição de camadas, permite o controle do tamanho dos grãos e da composição dos depósitos obtidos. As principais aplicações de ligas obtidas em meio de *DES* têm sido como revestimentos para proteção contra corrosão. Mas as propriedades promissoras destes materiais também levaram à sua aplicação em outros campos de pesquisa, como a fabricação de semicondutores e recentemente muitas pesquisas no desenvolvimento de eletrocatalisadores (ALCANFOR *et al*., 2017; ANICAI *et al*., 2013; CASCIANO *et al*., 2017; DOS SANTOS *et al*., 2019; FASHU *et al*., 2014; GRAY; LUAN, 2002; LIU *et al*., 2016; OLIVEIRA *et al*., 2021, 2022; PEREIRA *et al*., 2022, 2021; RODRIGUES-JÚNIOR *et al*., 2023; SEMEDO *et al*., 2023; SIMKA; PUSZCZYK; NAWRAT, 2009; SMITH; ABBOTT; RYDER, 2014; SOUSA *et al*., 2019; URCEZINO *et al*., 2016; VIJAYAKUMAR *et al*., 2013).

Portanto, os DES constituem atualmente uma nova e essencial alternativa para a obtenção de eletrodepósitos inovadores e sofisticados, com aplicações nos mais diversos ramos de pesquisa. Além disso, os DES apresentam uma contribuição significativa para o desenvolvimento de novos processos eletroquímicos sustentáveis, eficientes, econômicos e ambientalmente amigáveis.

2 MANUSCRITO 1: ON THE ROLE OF WATER IN ANTIMONY ELECTRODEPOSITION FROM CHOLINE CHLORIDE/ETHYLENE GLYCOL/WATER MIXTURE

Disponível em: https://doi.org/10.1016/j.molliq.2024.124416

Resumo

Por meio de pesquisa experimental e cálculo teórico, investigou-se o efeito da adição de água e da temperatura na eletrodeposição de antimônio (Sb) em eletrodo de platina (Pt) utilizando uma solução de eletrodeposição preparada pela mistura de cloreto de colina (ChCl), etilenoglicol (EG) e água (W) com a adição de $SbCl_3$ 0,05 mol L^{-1}. As soluções de eletrodeposição foram preparadas misturando-se ChCl, EG e W na seguinte proporção molar: 1ChCl:2EG (banho 1), 1ChCl:2EG:0,45W (banho 2) e 1ChCl:2EG:1,62W (banho 3). Além disso, o revestimento Sb foi eletrodepositado a 297 e 338 K. A morfologia e a estrutura cristalina dos eletrodepósitos de Sb foram analisadas por microscopia eletrônica de varredura (MEV) e difração de raios-X (DRX). Além disso, para entender as interações das espécies de Sb^{3+} com os demais componentes da solução de eletrodeposição, modelos foram criados e calculados utilizando a teoria do funcional da densidade (DFT) e a teoria quântica de átomos em moléculas (QTAIM). Os resultados do comportamento voltamétrico das espécies de Sb^{3+} indicaram que o potencial de redução foi deslocado para valores mais positivos com o aumento do teor de água no eletrólito, indicando que a água catalisa a redução eletroquímica das espécies de Sb^{3+}. Os valores dos coeficientes de difusão para as espécies Sb^{3+} foram calculados aplicando-se a equação de Cottrell. Os eletrodepósitos de Sb obtidos na ausência e presença de água apresentam morfologias diferentes. Além disso, os revestimentos eletrodepositados de Sb foram obtidos com sucesso sem adição de um agente complexante, indicando que o procedimento adotado para a eletrodeposição de Sb é ecologicamente correto. Os resultados de DRX revelaram filmes de fases puras de Sb. As simulações DFT indicaram que a interação Sb-Cl é mais forte, o que sugere a formação de complexos Sb-Cl. A adição de moléculas de H_2O favorece a afinidade eletrônica dos sistemas, e os resultados do QTAIM sugerem que este aditivo diminuiu a densidade eletrônica dos íons Sb^{3+}.

Palavras-chave: Antimônio; Solvente eutético profundo; Teor de água; DFT; QTAIM.

Abstract

Through experimental research and theoretical calculation, it was investigated the effect of water and temperature on the electrodeposition of antimony (Sb) on a platinum (Pt) electrode. The plating solutions were prepared by the addition of 0.05 mol L^{-1} $SbCl_3$ to the mixtures of choline chloride (ChCl), ethylene glycol (EG) and water (W) in the following molar ratio: 1ChCl:2EG (bath 1), 1ChCl:2EG:0.45W (bath 2), and 1ChCl:2EG:1.62W (bath 3). Furthermore, the Sb coatings were electrodeposited at 297 and 338 K. The surface morphologies and crystalline structures of Sb electrodeposits were analysed by scanning electron microscopy (SEM) and X-ray diffraction (XRD), respectively. In addition, to understand the interactions of Sb^{3+} species with the other components of the plating solution, models were created and calculated using density functional theory (DFT) and quantum theory of atoms in molecules (QTAIM). The results of the voltammetric behaviour of Sb^{3+} species indicated that the reduction potential was shifted towards more positive values with increasing water content on the electrolyte, indicating that the water catalyses the electrochemical reduction of the Sb^{3+} species. The values of the diffusion coefficients for the Sb^{3+} species were calculated by applying the Cottrell equation, which increased with the addition of water and temperature increment. The water content and temperature increase affect the surface morphologies of the Sb electrodeposited coatings, which is attributed to the improvement of Sb electrodeposition rate. Moreover, Sb electrodeposited coatings were successfully obtained without adding a complexing agent, indicating that the procedure adopted for the Sb electrodeposition is environmentally friendly. The XRD results revealed the pure phase Sb films. DFT simulations indicated that the Sb-Cl interaction is stronger, which suggests the formation of Sb-Cl complexes. Adding H_2O molecules favours the electron affinity of the systems, and QTAIM results suggested that this additive decreased the electron density of Sb^{3+} ions.

Keywords: Antimony electrodeposition; Deep eutectic solvent; Water content; DFT; QTAIM.

1 Introduction

Antimony (Sb) and Sb-based alloys are promising materials due to the wide range of applications in modern technologies, such as semiconductors [1], thermoelectric [2], electrocatalysts for the CO_2 reduction reaction [3], and recently, increased interest has been given to the development of anodic materials for rechargeable batteries, such as Li/Na-ion batteries [4,5]. In general, electrodeposition is one of the most employed methods to produce Sb coatings, and it stands out for being an effective technique to produce coatings on a large scale, with low cost and easy control of deposition parameters such as coating thickness and coating composition.

The Sb electrodeposition is reported in aqueous baths, either in acid electrolytes [6–10] as well in alkaline solutions [11,12]. However, one of the disadvantages that aqueous solutions can present is a restricted electrochemical potential range that can promote a competition on the surface of the working electrode between the hydrogen evolution reaction (HER) and the electrodeposition of chemical species of interest [13]. In addition, some metals require complexing agents in aqueous electroplating solutions to facilitate deposition, but some conventional complexing agents are not environmentally friendly, which can lead, in an industrial practice, to a non-suitable wastewater discharge.

Other electrolytes have been employed to overcome the cited disadvantages of aqueous solutions, such as the ionic liquids used for the electrodeposition of Sb and Sb alloys [14–17]. Among advantages, ionic liquids have a wide electrochemical range, good salt solubility and high conductivity. Additionally, the last two decades of the 21st Century saw the increasing use of deep eutectic solvents (DES) as a solvent for the formulation of electroplating solutions for electrodeposition of metals and alloys [18]. In general, DES can be obtained by mixing a quaternary ammonium salt with hydrogen bond donors in appropriate proportions. In addition to offering advantages to ionic liquids, DES are easy to prepare, biodegradable, non-toxic and environmentally friendly, which is very attractive for market prospects. Furthermore, the real potential of DES for the formulation of industrial commercial plating solutions has been evaluated by pilot projects in the Abbott Group [19]. These authors demonstrated that DES has the potential to become actual electrolytes for the industrial electroplating process, with emphasis on the electroplating of Ni, Fe and Zn.

The electrodeposition of Sb from DES based on choline chloride has been studied in mixtures with urea [20,21], oxalic acid [22] and ethylene glycol [23–28]. Additionally, the effect of adding water to DES has been investigated in recent years, especially in the

electrodeposition of metals and metal alloys [29–31]. Some researchers have demonstrated that adding water promotes the electrodeposition process of the species of interest and a significant reduction of viscosity in the plating solution, thus producing improvements in electrodeposition processes [32–34]. Furthermore, computational modeling studies have helped to elucidate the influence of temperature and water addition on DES properties [35–37].

Although the electrodeposition of Sb in eutectic solvent medium has been studied, the effect of water addition to the medium has yet to be reported. Thus, this work focuses on studying the effect of water addition and the temperature increase on the electrodeposition of Sb from mixtures containing choline chloride and ethylene glycol in the absence and presence of water. In the theoretical approach, Molecular Dynamics (MD), Density Functional Theory (DFT) and Quantum Theory of Atoms in Molecules (QTAIM) were used to analyse the behaviour of the DES and $SbCl_3$ system with different amounts of H_2O molecules to verify the behaviour of the system without and with additive, analysing the results on the electronic affinity of all systems, in addition to the strength of the interactions, on the type of interactions (intramolecular or intermolecular) of Sb^{3+} ions.

2 Experimental

2.1 Chemicals and viscosity measurements

All chemicals were used without any further purification. The eutectic mixture was prepared by mixing choline chloride (ChCl, Sigma-Aldrich®, ≥99%) and ethylene glycol (EG, Sigma-Aldrich®, ≥99.8%) in a molar ratio of 1:2 (1ChCl:2EG) and heated at 353 K until the formation of a colourless liquid [38]. Then, a required amount of water, treated by the Milli-Q system (18.2 MΩ cm), was added to the 1ChCl:2EG to form solutions with a water molar ratio of 0.45 (1ChCl:2EG:0.45W) and 1.62 (1ChCl:2EG:1.62W). The plating solutions were prepared by the addition of 0.05 mol L^{-1} of anhydrous antimony (III) chloride ($SbCl_3$, Sigma-Aldrich®, ≥ 99%) in each one of the prepared solvents: 1ChCl:2EG, 1ChCl:2EG:0.45W and 1ChCl:2EG:1.62W, to form the baths 1, 2, and 3, respectively. Finally, the viscosity (η) of the electroplating solutions was measured at 297 and 338 K temperatures using an Anton Paar® viscodensimeter model SVM-3000.

2.2 Electrochemical measurements

All electrochemical experiments were carried out using a conventional three-electrode electrochemical cell and carried out at 297 and 338 K. A potentiostat/galvanostat (Autolab PGSTAT30, Metrohm) controlled by NOVA software version 2.1.4 were used for the acquisition and analyses of the electrochemical data. Two Pt electrodes were used as a working electrode for the electrochemical experiments. The first was a disk electrode with a diameter of 0.5 mm (geometric surface area of 0.0019 cm^2), which was used in the cyclic voltammetry and chronoamperometry measurements. The second was a foil, with 0.5 cm^2 of geometric area, which was used to obtain the Sb electrodeposits under potentiostatic control. Before each electrochemical experiment, the working electrodes were sanded on SiC silicon carbide 600 grit sandpaper, washed with Milli-Q water (18.2 MΩ cm), and dried with airflow. The auxiliary electrode was a Pt plate, with 1.0 cm^2, and an $Ag_{(s)}/AgCl_{(s)}$ wire immersed in 1ChCl:2EG mixture was used as the reference electrode. Using 25 mV s^{-1} at 297 and 338 K, the cyclic voltammetry (CV) results were achieved between +0.6 and –1.5 V to characterize the electrode surface in the choline chloride and ethylene glycol mixture in the absence and presence of water, while the electrochemical reduction of Sb^{3+} species was assessed by scanning the potential between +0.4 and –0.6 V. Chronoamperometric measurements were made to achieve the diffusion coefficients (D) of the Sb^{3+} species using Cottrell's Equation. The current-time transient curves were obtained by applying 0.4 V for 10 s, followed by a jump to –1.0 V for 60 s.

Lastly, the Sb electrodeposits were obtained by applying the values of cathodic peak potentials derived from the cyclic voltammograms of the Sb^{3+} species in electrolytic solutions in the absence and presence of water, such as –0.35 V; –0.33 V and –0.30 V at 297 K, and –0.29 V; –0.27 V and –0.24 V at 338 K, for the baths 1, 2 and 3, respectively. Finally, the electrodeposition time was fixed in 1800 s, and Faraday's Equation was used to estimate the amount of Sb electrodeposited.

2.3 Morphological and structural characterization

The surface morphology of the Sb electrodeposits was characterized by a field-emission scanning electron microscope (FEG-SEM FEI-Quanta 450). X-ray diffraction (XRD) analyses were conducted using a PANalytical® diffractometer model X-Pert PRO with CoKα (λ = 1.789 Å) radiation, operating at 40 kV and 40 mA in the range 10° to 100°. The

experimental data was treated using PANalytical® X'Pert HighScore Plus® software, and the crystalline phases presented in diffractograms were indexed in the crystallography PDF-22004 card files from the International Centre for Diffraction Data (ICDD).

2.4 Computational simulations

To describe the system without water, one molecule of $SbCl_3$, two molecules of EG and one molecule of ChCl were drawn. The number of water molecules (X = 3, 5, 10 and 15) was gradually added to describe the systems with water. To obtain the optimized geometries of the studied systems, the software XTB version 6.5.0 [39] was used, and molecular dynamics simulations were carried out, obtaining 2000 geometric structures (frames). Finally, the Molclus software version 1.9.9.7 [40] was used to rank the energy of the 2000 structures, and the system with the lowest energy was chosen for the geometries optimization at the DFT level. The DFT calculations were carried out in PBE-D3BJ/Def2-TZVP [39,41] and Def2/J auxiliary basis [42] in the ORCA 5.0.4 software [43,44]. The calculation of the vertical electron affinity energy (VEA) [45,46] in (Equation 1) was used to obtain a correlation between the addition of water and the susceptibility of the system to the reception of electrons, thus being associated with the reduction of antimony cation (Sb^{3+}) and addition of H_2O. Finally, the relative VEA was calculated (ΔVEA), where the reference value for energy is that of the system without water (Equation 2).

$$VEA = (G_{neutral}) - (G_{anion}) \quad (1)$$

$$\Delta VEA = (VEA_{System\ A}) - (VEA_{System\ X\ H_2O}) \quad (2)$$

In these equations, $G_{neutral}$ is the free energy of the uncharged system, G_{anion} is the free energy of the system after adding an electron; $VEA_{System\ A}$ is the electron affinity of the system without water, and $VEA_{System\ X\ H_2O}$ is the electron affinity of the system with X H_2O molecules.

Bader's "atoms in molecules" (AIM) theory, also referred to as the "quantum theory of atoms in molecules" (QTAIM), is utilized to analyse the electronic density [47]. The electron density gradient vector ($\nabla\rho$) is obtained by calculating the first derivative of ρ is 0 for potential effective electron density over all coordinates. A critical point (CP) is a point in space where each derivative of $\nabla\rho$ is zero ($\nabla\rho$ = 0). The second derivatives of electron density are used to

differentiate critical points from local minimums, local maximums, or saddle critical points. Four types of stable critical points exist, all having three non-zero eigenvalues. Two negative eigenvalues of the function's Hessian matrix characterize a second-order saddle point. The bond critical point (BCP), commonly found between attractive atomic pairs in electron density analysis, has a classification of (3,-1) [48]. The AIM data were obtained by the MULTIWFN 3.8 software [49] and visualized by the VMD software [50].

3 Results and discussion

3.1 Electrochemical studies

Initially, the cyclic voltammograms (CVs), shown in Fig. S1 (Supplementary Material), were achieved between +0.6 and –1.5 V, at 25 mV s^{-1} and 297 K (Fig. S1(a)) and at 338 K (Fig. S1(b)) to evaluate the addition of water on the electrochemical range of the 1ChCl:2EG mixture. In these CVs, it can be noted that any electron transfer reaction is observed between +0.6 and –0.8 V. For potentials more negative than –0.8 V, there is an increase in cathodic current density with the addition of water, which can be attributed to the reduction of hydroxyl groups of EG, choline ions (Ch^+) and water molecules [51]. An anodic process around –0.2 V is present for all scans towards more positive values. This process is attributed to the oxidation of water and groups of EG. Therefore, these results indicate that the water and the solvent molecules are simultaneously electrochemical reduced at potentials more negative than –0.8 V. Moreover, for applied potentials more negative than –0.8 V, the current density values, displayed in Fig. S1(b), are higher than those shown in Fig. S1(a), which means the electrochemical reduction rates of all chemical species increase with the temperature. These results agree with previously reported works investigating the electrochemical potential window onto Pt electrode on 1ChCl:2EG with water additions [30,31].

The effect of water addition on the electrochemical behaviour of Sb^{3+} species on the Pt electrode was investigated by the CVs shown in Fig. 1. The experiments were conducted at 25 mV s^{-1} between +0.4 and –0.6 V, at 297 K (Fig. 1(a)) and 338 K (Fig. 1(b)).

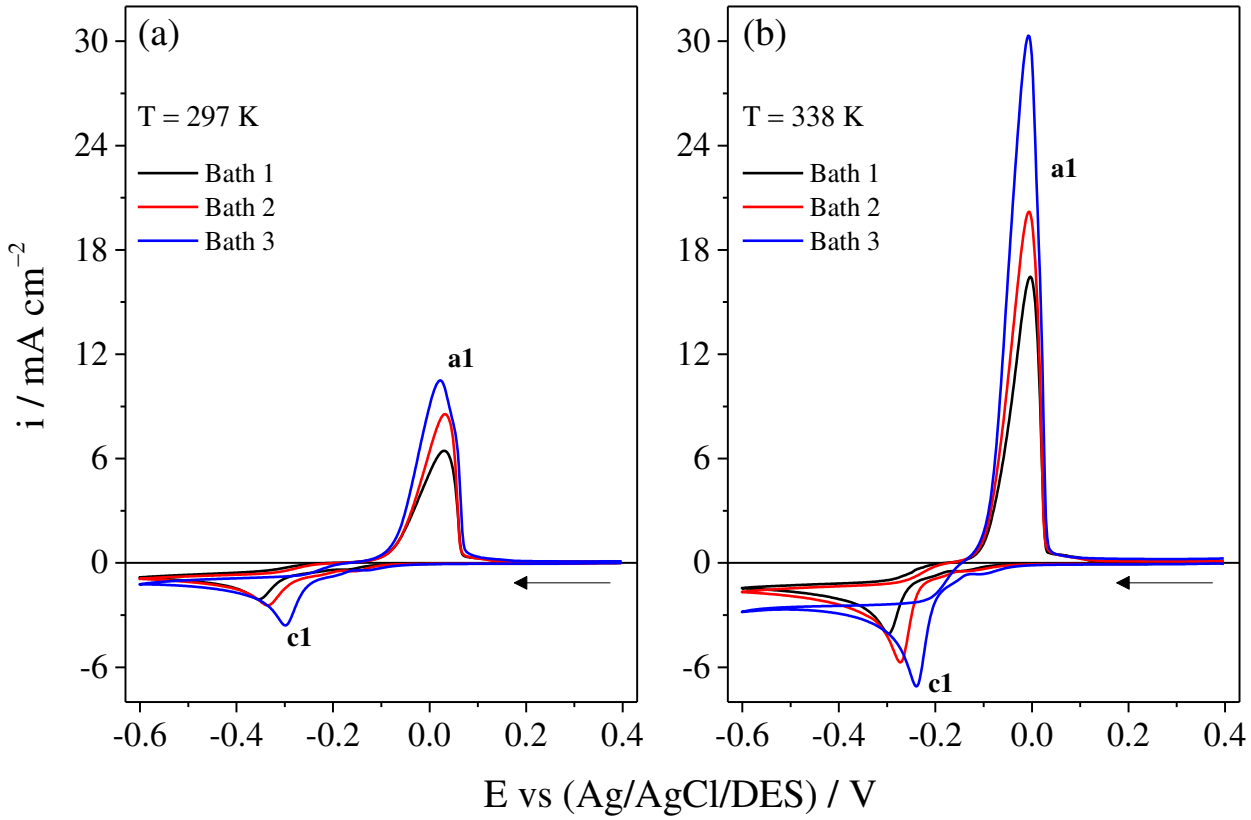

Fig. 1. Cyclic voltammograms obtained on Pt electrode in baths 1, 2 and 3 containing 0.05 mol L^{-1} $SbCl_3$ at 297 K (a) and 338 K (b). All cyclic voltammograms were obtained at 25 mV s^{-1}.

According to the results of Fig. 1(a-b), it is observed that all direct scans (scanning towards more negative potentials) presented a cathodic peak (c1), which is attributed to the reduction of the Sb^{3+} to Sb. The peak potentials are located at −0.35 (bath 1), −0.33 (bath 2), and −0.30 V (bath 3) at 297 K and −0.29 (bath 1), −0.27 (bath 2), and −0.24 V (bath 3) at 338 K, respectively. These results indicate that the water addition in the plating solutions catalyses the electrochemical reduction of the Sb^{3+} species, because, for both temperatures and in all plating solutions, the Sb electrodeposition potential shifts towards more positive values with the increase in the water content in the plating solutions. Furthermore, with increasing the water content from 0 up to 1.62 molar ratio, the peak reduction potential c1 of Sb^{3+} becomes less negative from −0.35 to −0.30 V at 297 K and from −0.29 to −0.24 V at 338 K. These results from Fig. 1(a-b) are listed in Table 1. Also, the cathodic peak current densities (i_{pc}) become increasingly pronounced with a further increase in water content in the electrolytic solution, which means that water improves the Sb electrodeposition rate.

Moreover, Table 1 also displays the viscosity for all tested plating solutions at both working temperatures. It can be noted in this table that at each working temperature, the

viscosity decreases with water addition, and consequently, this led to an increase in the plating solution conductivity with the increase of the water content. This fact was confirmed by the increase of the diffusion coefficient values of Sb^{3+} species (D) with the increase in the water content in each investigated temperature, which is displayed in Table 2. The D values were obtained from the experimental chronoamperometric curves, shown in Fig. S2. According to the values listed in Table 2, the D values obtained in this work increase with the addition of water, and the variation of 41 K promotes an increase of one order of magnitude in the D values. Moreover, the D values achieved in this work at 297 K are in the same order of magnitude as those D values published in the literature for eutectic solvents and ionic liquids. Besides that, for the electrolytic solution with the addition of water and at 338 K, the D values present the same order of magnitude as those reported in the literature for aqueous solutions. Therefore, there is a good agreement between the D values reported in this work and those already published in the literature. Thus, the changes in the D values with water content result in higher ionic mobility and, consequently, increase the electrochemical reduction rate of the Sb^{3+} species, which justifies the increase in the cathodic current density values.

Table 1. Effect of water addition on the voltammetric profiles during the reduction of Sb^{3+}/Sb on Pt electrode.

T / K	Water molar ratio in the plating solutions	E_{pc} / V	i_{pc} / mA cm^{-2}	η / mPa s
297	0.00	−0.35	−2.086	43.198
	0.45	−0.33	−2.438	32.841
	1.62	−0.30	−3.592	20.162
338	0.00	−0.29	−4.054	11.113
	0.45	−0.27	−5.717	8.9119
	1.62	−0.24	−7.108	5.9378

Table 2. Comparison of diffusion coefficients of Sb^{3+} obtained in this investigation with those already reported in the literature for plating solutions based-formulated in DES, ionic liquids and in water.

Reference	D / cm^2 s^{-1}	System	T / K
[9]	1.051×10^{-5}	H_2SO_4-NH_4F	298
[9]	2.120×10^{-5}	H_2SO_4-NH_4F	318
[55]	3.76×10^{-6}	Citrate Bath	293
[13]	5.27×10^{-6}	6 M HCl	318
[14]	2.98×10^{-7}	EMI–Cl–BF_4	303
[15]	6.07×10^{-7}	[EMIm]BF_4	298
[16]	1.23×10^{-7}	BMP-DCA	308
[56]	1.65×10^{-5}	LiCl–KCl molten salt	673
[21]	2×10^{-7}	1ChCl:2U	353
[27]	4.719×10^{-7}	1ChCl:2EG	333
[23]	8.86×10^{-7}	1ChCl:2EG	343
In this work	1.79×10^{-7}	1ChCl:2EG	297
In this work	3.13×10^{-7}	1ChCl:2EG:0.45W	297
In this work	4.76×10^{-7}	1ChCl:2EG:1.62W	297
In this work	1.01×10^{-6}	1ChCl:2EG	338
In this work	1.10×10^{-6}	1ChCl:2EG:0.45W	338
In this work	1.29×10^{-6}	1ChCl:2EG:1.62W	338

For the reverse scan, an anodic peak (a1) is observed in all cyclic voltammograms obtained at 297 K and 338 K. The a1 peak is ascribed to the electrochemical oxidation process of Sb to Sb^{3+} [23,25]. In addition, despite the electrochemical behaviour of the Sb^{3+} species being similar in the absence and the presence of water, it can be noted that the a1 peak is larger than the c1 peak, and it increases more than the c1 peak as the water content increases. The explanation for the a1 peak being larger and higher than the c1 peak is related to the fact that the total amount of Sb electrodeposited on the Pt surface is the sum of the Sb mass electrodeposited in the direct scan with the Sn mass electrodeposited in the reverse scan between –0.6 V and the potential in which the electric current becomes zero. Additionally, the Sb electrodeposition efficiencies (ε_{ed}), which are shown in Table 3, were estimated by the ratio between the electric charge related to electrochemical dissolution of Sb coating (peak a1, Q_{ecd})

and electrodeposition charge (Q_{ec}), which was calculated taking into consideration the electric charge related to the electrochemical reduction of Sb^{3+} species to Sb in the direct scan summed with that related to the formation of Sb coating in the reverse scan. The Table 3 shows that the ε_{ed} values are higher, varying from 91% up to 95%. Furthermore, the ε_{ed} values increase with the temperature and water addition, and for each tested temperature, the ε_{ed} values improve with the addition of water, which is explained by the increment in the ionic mobility related to the rise in the water content. Therefore, all these results evidence that the addition of water catalyses the electrochemical reduction of the Sb^{3+} species to form the Sb electrodeposited coating. Lastly, these results are in close agreement with research previously reported in the literature about the influence of water content and temperature for deep eutectic solvent-based electrochemical systems [31,33,34,37].

Table 3. Influences of water molar ratio and temperature on the electrodeposition efficiency of Sb from choline chloride/ethylene glycol/water mixture. The data listed in this table were derived from the cyclic voltammograms shown in Fig. 1.

T / K	Water malar ratio in the plating solutions	Q_{ecd} / C	Q_{ec} / C	ε_{ed} / %
297	0.00	0.061 ± 0.00141	0.067 ± 0.00152	91
	0.45	0.0735 ± 0.00212	0.0795 ± 0.00232	92
	1.62	0.101 ± 0.00283	0.107 ± 0.00354	94
338	0.00	0.120 ± 0.00111	0.130 ± 0.00121	92
	0.45	0.149 ± 0.00151	0.160 ± 0.00142	93
	1.62	0.167 ± 0.00212	0.175 ± 0.00283	95

It is known that the metal ions in DES can form complexes with chloride ions and ethylene glycol. For instance, Hartley et al. [52] investigated the speciation of 25 metal salts in four DES and five imidazolium-based ionic liquids using the EXAFS technique. The authors demonstrated that monovalent metal ions formed two complex species in solution $(MCl_2)^-$ and $(MCl_3)^{2-}$ complexes, while the divalent metal ions (M^{2+}) formed the $(MCl_4)^{2-}$ complexes. Furthermore, these authors also demonstrated that the addition of water did not affect the formation of these complexes. In addition, Oelkers et al. also used the EXAFS technique to identify the occurrence of Sb^{3+} species complexed with Cl^- ions in highly concentrated HCl solution from 25 up to 250 °C and at pressures corresponding to the liquid-vapor equilibrium

curve for water [53]. These authors pointed out that the stability of the $SbCl_3$ $[SbCl_4]^-$, $[SbCl_6]^{3-}$ complexes increased with temperature. Besides that, the Potential - pH diagram of the Sb-H_2O system [54] shows that the $[Sb(OH)_6]^-$ and $HSbO_2$ are the soluble complex species at pH 7. Therefore, from this reports [54–56], it is suggested that the mechanism of the electrochemical deposition of Sb is associated with the presence of these Sb complex species in the 1ChCl:2EG:0.45W and 1ChCl:2EG:1.62W plating solutions.

3.2 Morphological and structural characteristics of Sb films

Fig. 2 shows the SEM images of the antimony electrodeposits at 297 K (Fig. 2(a-c)) and 338 K (Fig. 2(d-f)) in the baths 1, 2 and 3. For the Sb coating obtained at 297 K and without the addition of water, the surface morphology is uniform without the presence of agglomerates (Fig. 2(a)). For those obtained the in presence of water from baths 2 and 3 (Figs. 2(b) and 2(c)), a dendrite-like morphologies can be observed. Additionally, with increasing water content, dendritic structures predominate. In contrast, for all electrodeposits obtained at 338 K, a hierarchical structure in sheets is observed, as shown in Fig. 3(d-f). For greater clarity of the description of Sb sheets, it is given the magnification of the samples obtained at 338 K in the Fig. S3 (Supplementary Material). The change in the surface morphology of the Sb electrodeposited coatings change with temperature and water content is attributed to the fact that the rate of the mass transport of the Sb^{3+} species from the solution to the electrode surface becomes greater with the increases of the temperature and water content, leading to an improvement in the kinetics of the Sb electrodeposition. The Table 4 shows that the Q_{ec} and, consequently, the Sb electrodeposited masses (m_{ed}) are increasing with the increases of water content and temperature, which is experimental evidence that the kinetics of the Sb electrodeposition became greater when the temperature and water content are increased. Therefore, the change in the surface morphology of the Sb electrodeposits with water and temperature is attributed to the improvement in the electrodeposition rate of the Sb electrodeposits related to the increase of both water and temperature.

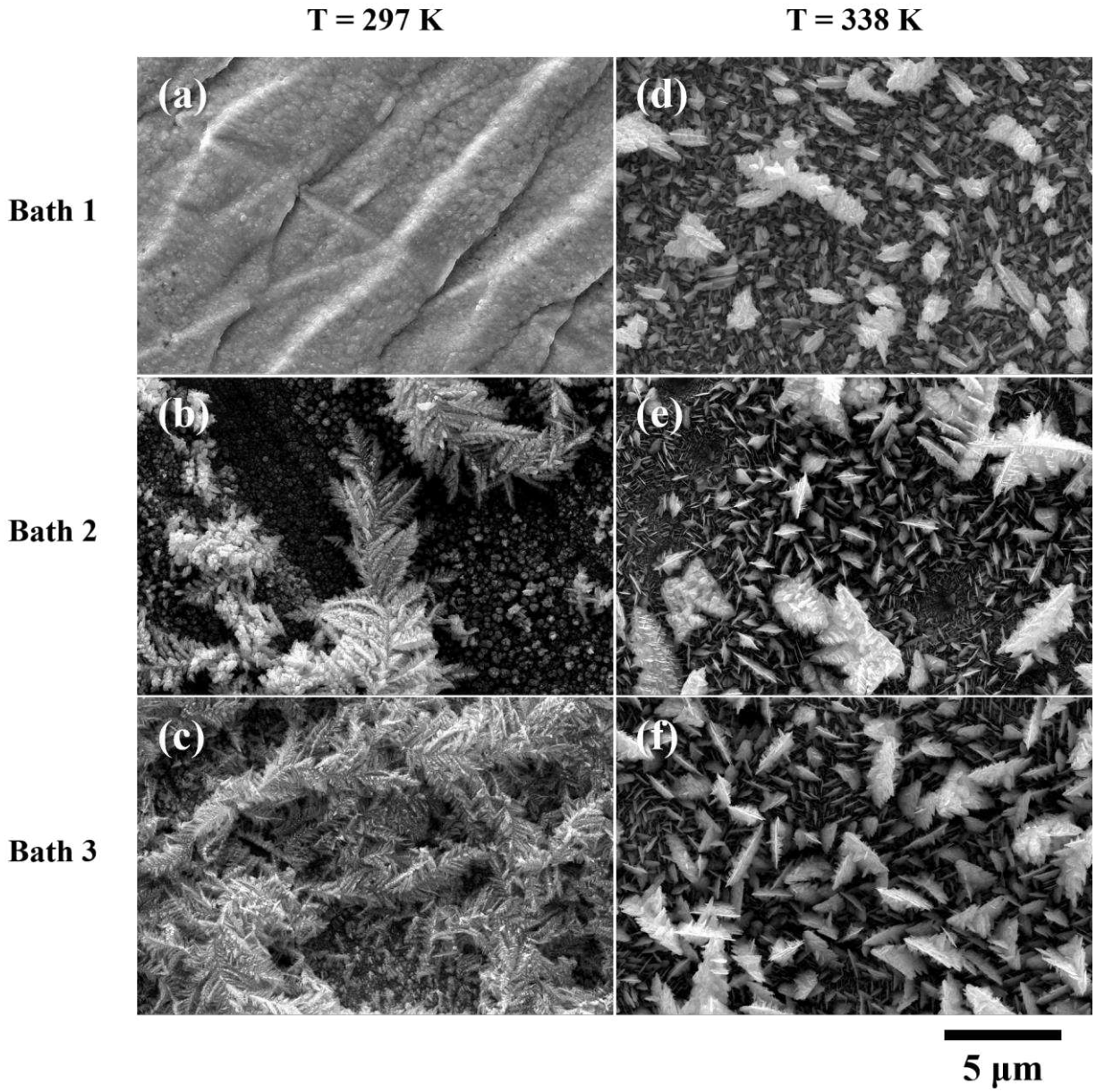

Fig. 2. SEM micrographs of Sb electrodeposits onto Pt electrode obtained at 297 K (a-c) and 338 K (d-f) in baths 1, 2 and 3 containing 0.05 mol L^{-1} $SbCl_3$, and under potentiostatic control at (a) –0.35 V, (b) –0.33 V, (c) –0.30 V, (d) –0.29 V, (e) –0.27 V and at (f) –0.24 V for 1800 s.

Tabel 4. Electrodeposition potential (E_{dep}), electrodeposition charge (Q_{ed}) and mass of the electrodeposited Sb coating (m_{ed}) at different temperatures and water contents. The Sb electrodeposited mass values were obtained from Faraday's Equation.

T / K	Water malar ratio in the plating solutions	E_{dep} / V	Q_{ec} / mC	m_{ed} / mg
297	0.00	− 0.35	2.98 ± 0.135	0.08 ± 0.060
	0.45	− 0.33	3.89 ± 0.063	0.11 ± 0.030
	1.62	− 0.30	5.61 ± 0.013	0.15 ± 0.006
338	0.00	− 0.29	34.89 ± 0.190	0.94 ± 0.080
	0.45	− 0.27	37.31 ± 0.120	1.00 ± 0.050
	1.62	− 0.24	39.32 ± 0.130	1.06 ± 0.050

The X-ray diffraction was accomplished to investigate the effect of water content and temperature on the crystalline structure of Sb films. The Fig. 3(a-f) presents the diffraction patterns for the Sb electrodeposits on the Pt surface obtained in baths 1, 2 and 3, at 297 and 338 K. For diffractograms of Fig. 3(a-f), peaks referring to the Sb phase of the rhombohedral crystal structure and space group (R-3mH, #166) at the 2θ positions of 27.57°, 29.29°, 33.45°, 49.15°, 56.92°, 57.00°, 60.73°, 70.26°, 74.74°, 81.87°, 90.81°, 91.57° and 92.07° were indexed. Additionally, Pt peaks referring to the substrate with the face-centered cubic crystal structure (FCC) and space group (Fm-3m, #225) at the 2θ positions of 46.57°, 54.29°, 80.32° and 98.26° were indexed. The phases of Sb and Pt were identified according to the patterns of ICDD #01-085-1323 and #01-087-0646 card files, respectively. No peaks resulting from contaminations were identified. Fig. 3 shows the diffraction peaks from metallic Sb phases. It can be observed that there is an increase in the number of metallic Sb phases with the addition of water and an increase in the bath temperature. This may suggest that Sb electrodeposition was favoured under these conditions.

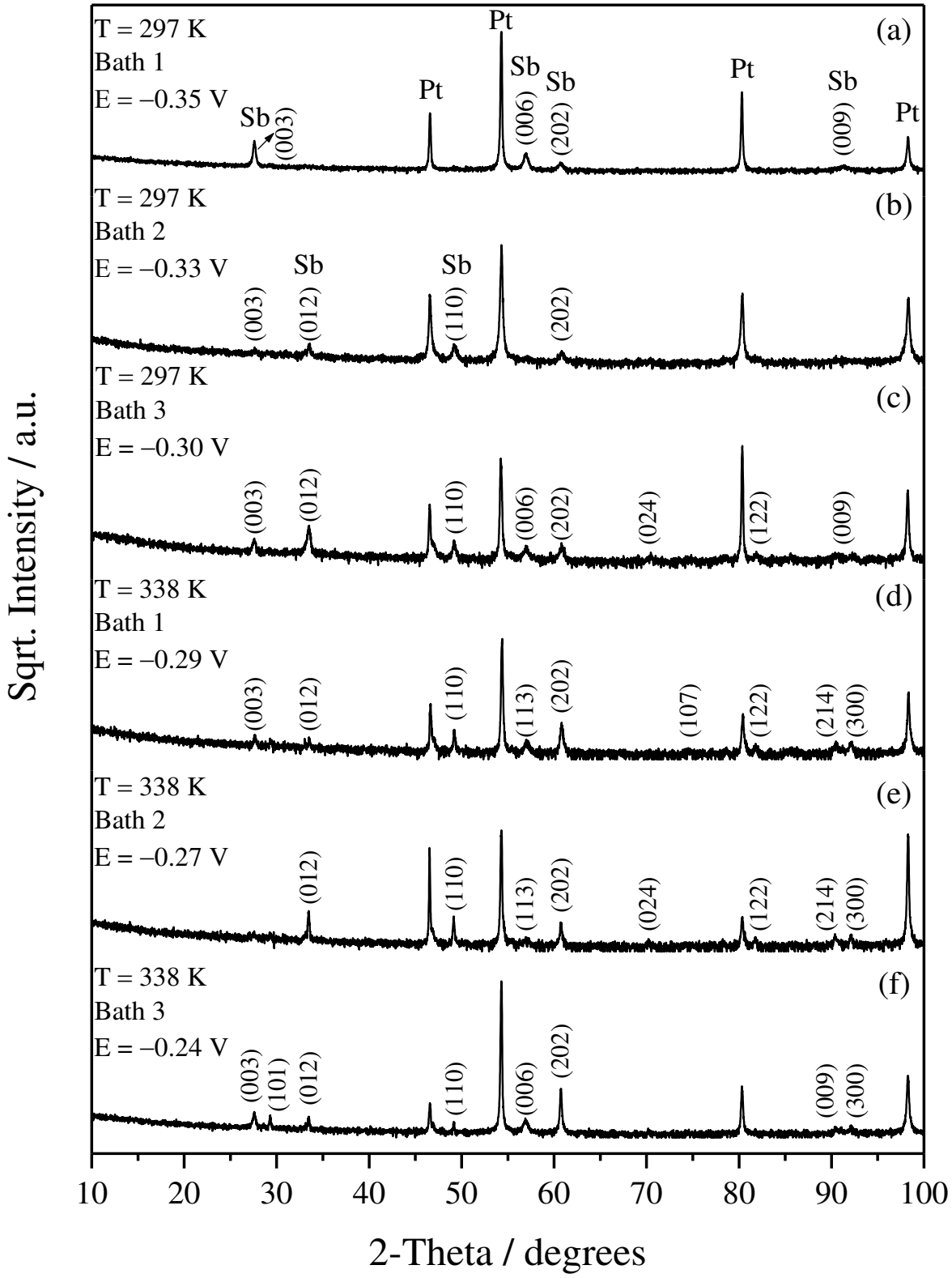

Fig. 3. X-ray diffraction pattern of Sb electrodeposits onto Pt electrode at 297 K (a-c) and 338 K (d-f) in baths 1, 2 and 3 containing 0.05 mol L^{-1} $SbCl_3$, obtained under potentiostatic control at (a) –0.35 V, (b) –0.33 V, (c) –0.30 V, (d) –0.29 V, (e) –0.27 V and at (f) –0.24 V for 1800 s.

3.4 Computational results

The molecular dynamics simulations were carried out using the XTB software, and after ranking the energy of each frame, the frame with the lowest energy was selected. The geometry was then optimized at the DFT- PBE-D3BJ/Def2-TZVP level of theory for System (A) (0 H_2O); System (B) (3 H_2O); System (C) (5 H_2O); System (D) (10 H_2O); and System (E) (15 H_2O) as can be seen in Fig. 4. The simulations work using the molecular dynamics approach tries to carry out its approach with the most faithful numbers of atoms and molecules possible in a box of nanometric dimensions, with numbers of atoms of approximately tens of thousands of units, in a molecular dynamic simulation box [33,37,57]. The simulation of a system is limited and is generally chosen through a relationship between precision and computational cost. An approach involving Density Functional Theory (DFT), such as in the simulation and prediction of material properties, as well as thermodynamic and electronic properties, depending on the levels of approximation and theory chosen, the maximum system size achieved is around 1000 atoms [58]. Increasing the size of the system is impractical due to the high cost associated with DFT (its computational cost is proportional to N^3). Applying a real system in reduced quantities, keeping the proper proportions of $SbCl_3$, ChCl, EG and H_2O, the number of atoms in the system is still around thousands of units. The configurations of the molecules and their respective conformations were obtained using the XTB and Molclus software, thus obtaining the best minimum energies for each system, and starting from this minimum energy conformation, the DFT calculations were carried out. Therefore, the aim was to apply a methodology that can describe a qualitative and approximate, but pioneering, result, applying a slight and gradual increase in the number of waters in the system to obtain a correlation of the effect of water in deep eutectic solvent (DES) for the Sb electrodeposition.

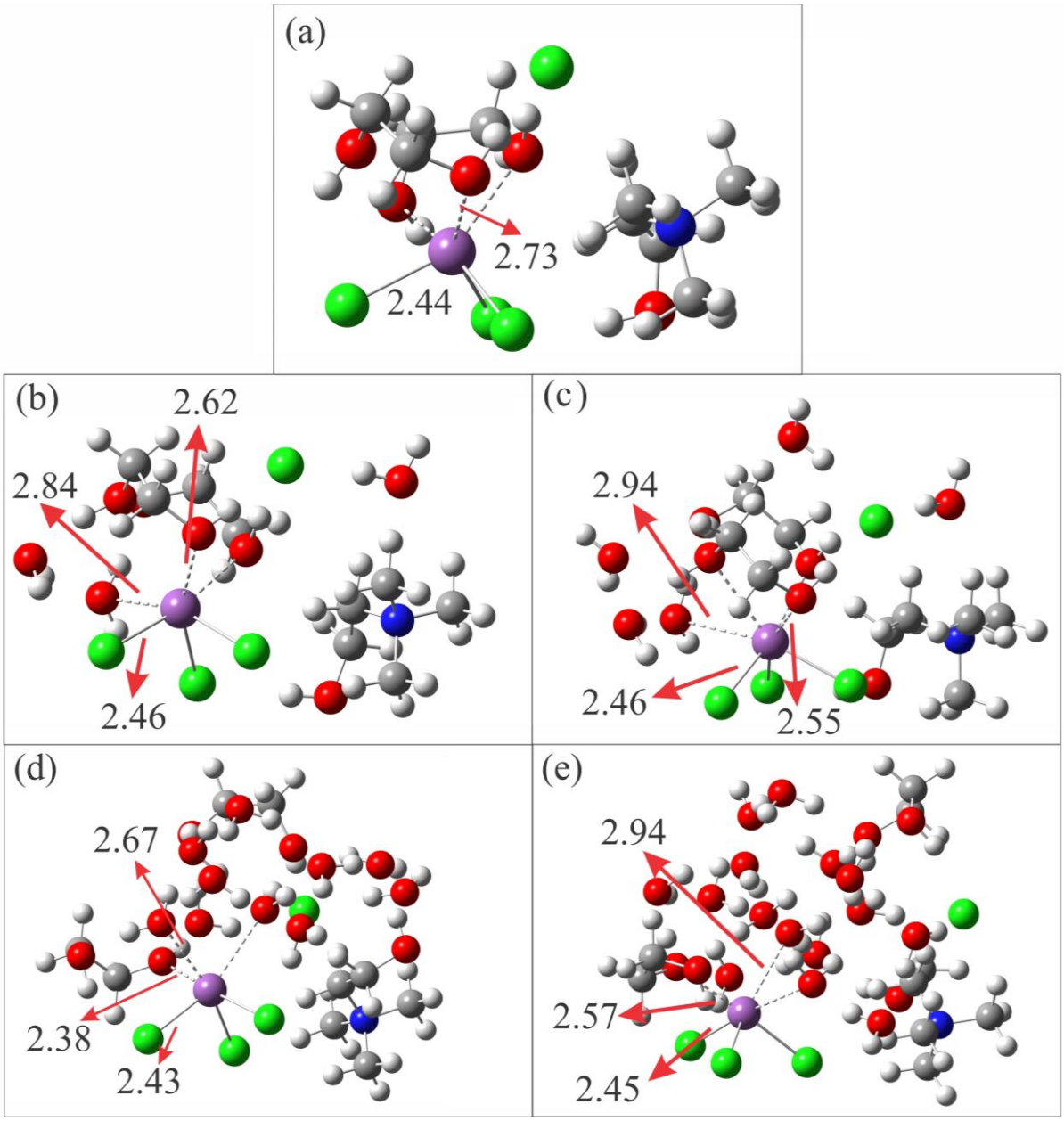

Fig. 4. Optimized geometries of the molecules of the system without H_2O molecules (a), 3 H_2O molecules (b), 5 H_2O molecules (c), 10 H_2O molecules (d), and 15 H_2O molecules (e). Bond lengths are in Angstroms.

To represent each system's electronic reception (reduction), 1, 2 and 3 electrons were added, referring to the reduction of $Sb^{+3,}$ and their respective energies were calculated at the DFT level. The difference between the neutral system and the anion system gives us the electronic affinity of the system (Equation 1). Table 5 provides the data obtained for the VEA of the systems. Table 5 shows that the VEA of the systems increases as the number of waters increases, so the trend is towards adding 1, 2 and 3 electrons. Furthermore, Table 6 shows the

ΔVEA (Equation 2), where the system without water is taken as a reference. Therefore, the inclusion of quantities of water in DES systems favours the electrodeposition of metals [33,35,59,60]. The model proposed by computational methods suggests an increase in the electron receptivity of the DES system with the addition of water due to the linear increase in ΔVEA with the increase in water in the system, compared to the system without water. The ΔVEA values for 1 electron are 14.50, 14.78, 22.25, and 24.84 kcal mol^{-1} for System B, C, D, and E, respectively (Table 6). The trend is also observed for 2 and 3 electron reduction. The tendency for the electronic affinity of systems to increase with increasing water content so that antimony can be favored for electronic reception it may explain its contribution to adding water to favor the electrochemical reduction process of Sb^{3+}. In addition, the coefficient of determination (R^2) between ΔVEA and the number of water molecules added to the systems is shown in Fig. 5. The $R^2 = 0.822$ represents a good correlation between the increase in electron affinity and the increase in water molecules in the systems studied.

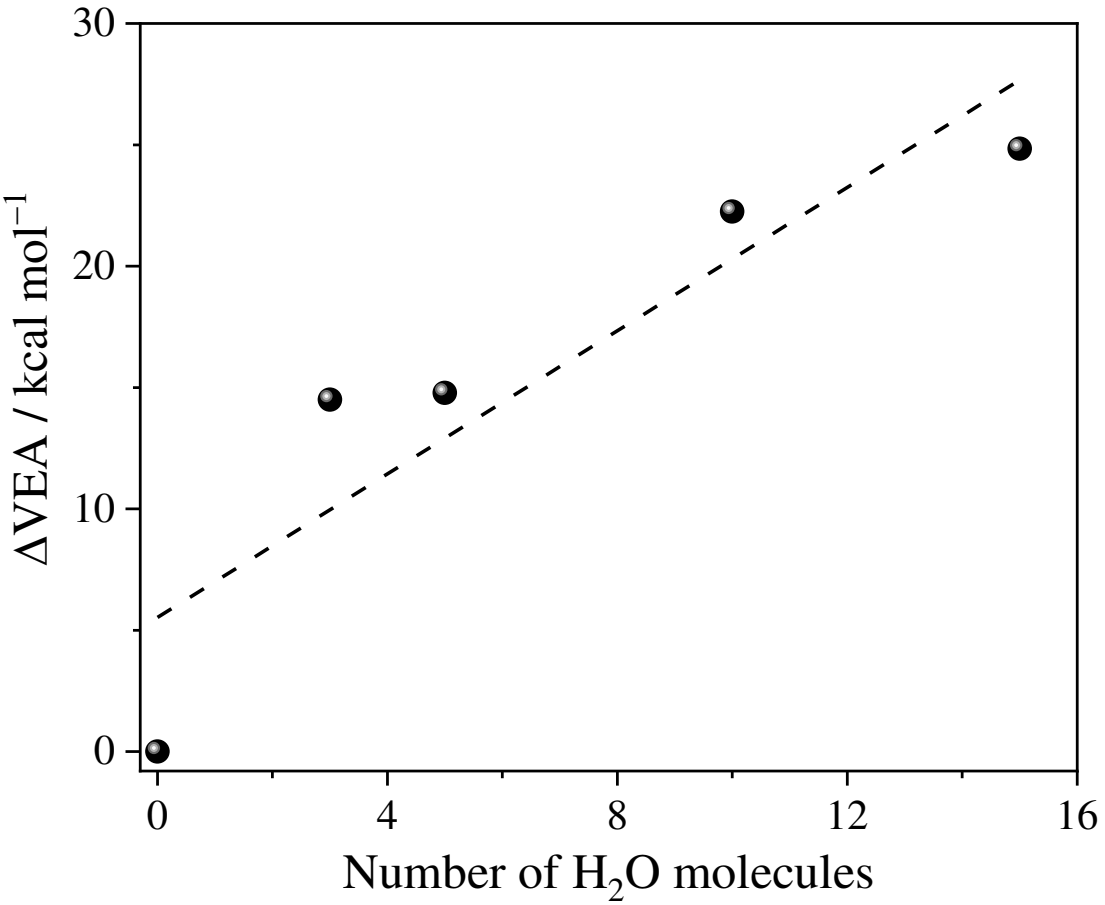

Fig. 5. Plot of ΔVEA (in kcal mol^{-1}) in function of the number of H_2O molecules.

QTAIM is a mathematical approach in computational chemistry that aims to provide insights into the nature of chemical bonding and molecular properties. The central concept of QTAIM is using mathematical functions to analyse the electron density in a molecule, which allows the identification of critical points, such as bonding critical points, that define the location of chemical bonds [61]. This study deals only with the antimony cations (Sb^{+3}) critical bond points (BCP). The analysis was carried out using the parameters All-Electron density (ρ_b), Laplacian of the electron density ($\nabla^2\rho_b$) and Energy density (Hb). If the $\nabla^2\rho_b$ and Hb are less than zero, this indicates a strong covalent interaction between the antimony and the molecules in the system (EG, ChCl and water). On the other hand, if the values are more significant than zero, there is a weak electrostatic interaction between them. Notably, the interaction can be partially covalent when $\nabla^2\rho_b$ is more significant than zero, but H_b is less than zero [62]. The QTAIM analysis indicates that in all systems $\nabla^2\rho_b$ has a positive value and H_b has a negative value, indicating that the BCP interactions of the molecules in the system (EG, ChCl and water) around Sb^{3+} are partially covalent. Moreover, the electron density values (ρ_b) of the chlorine BCPs (BCPs 1, 2 and 3) have higher ρ_b values ($\approx 7 \times 10^{-2}$ a.u.) than the other interactions in BCPs 4, 5, 6 and 7 ($\approx 2 \times 10^{-2}$ a.u.) (see Tables S1-S5 in the Supplementary Material), as evidenced by the that the Sb-Cl bond lengths are closer than the others (Fig. 4), and, consequently, the Sb-Cl interaction is the stronger which suggest the formation of Sb-Cl bond. The $SbCl_3$ complex has an experimentally favourable formation constant, and possible bonds between EG and H_2O with the $SbCl_3$ complex can also be considered for the system [63–65]. However, the gradual addition of H_2O decreased the electronic density with Sb^{3+}, seen at 0.319 a.u. for System A (without H_2O), and there is a downward trend until 0.311 a.u. for System E (15 H_2O molecules) (see Tables S1-S5 Supplementary Material). Plotting the R^2 between the number of water molecules added and the sum of the electronic density ($\Sigma\rho_b$) shown in Fig. 6, we obtained a R^2 of 0.932, indicating a very good correlation. In addition, after the addition of 3 waters, shown in Fig. 7, there is a substitution of the bonds of the $SbCl_3$ complex with EG, being replaced by bonds with H_2O, and just as in the 10 H_2O system, there is another substitution of EG for H_2O, and maintaining these bonds with 15 molecules of H_2O.

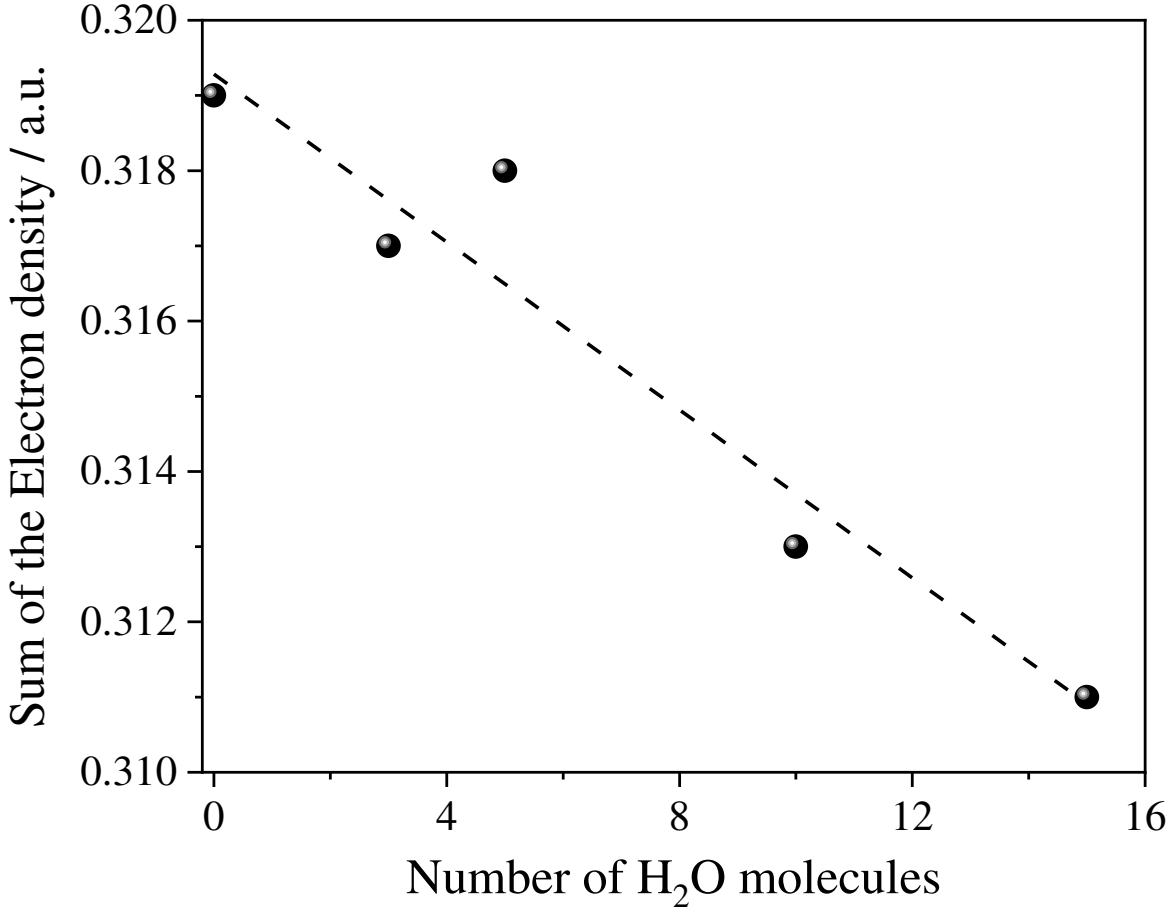

Fig. 6. Plot of sum of the electronic density ($\Sigma\rho_b$) in function of the number of H_2O molecules.

The QTAIM results obtained in this study may corroborate the efficiency of water in weakening the interaction of Sb^{3+} ions with the H_2O molecules in the system, thus facilitating its electrodeposition. This can be associated with a more easily displacement of the Sb^{3+} ions in the solution to be deposited on the electrode surface, corroborating the diffusion coefficient results. The idea of the QTAIM study is to associate the mobility of Sb^{3+} to electrodeposition, in which this lower electronic density due to the higher number of H_2O molecules would facilitate the ionic mobility.

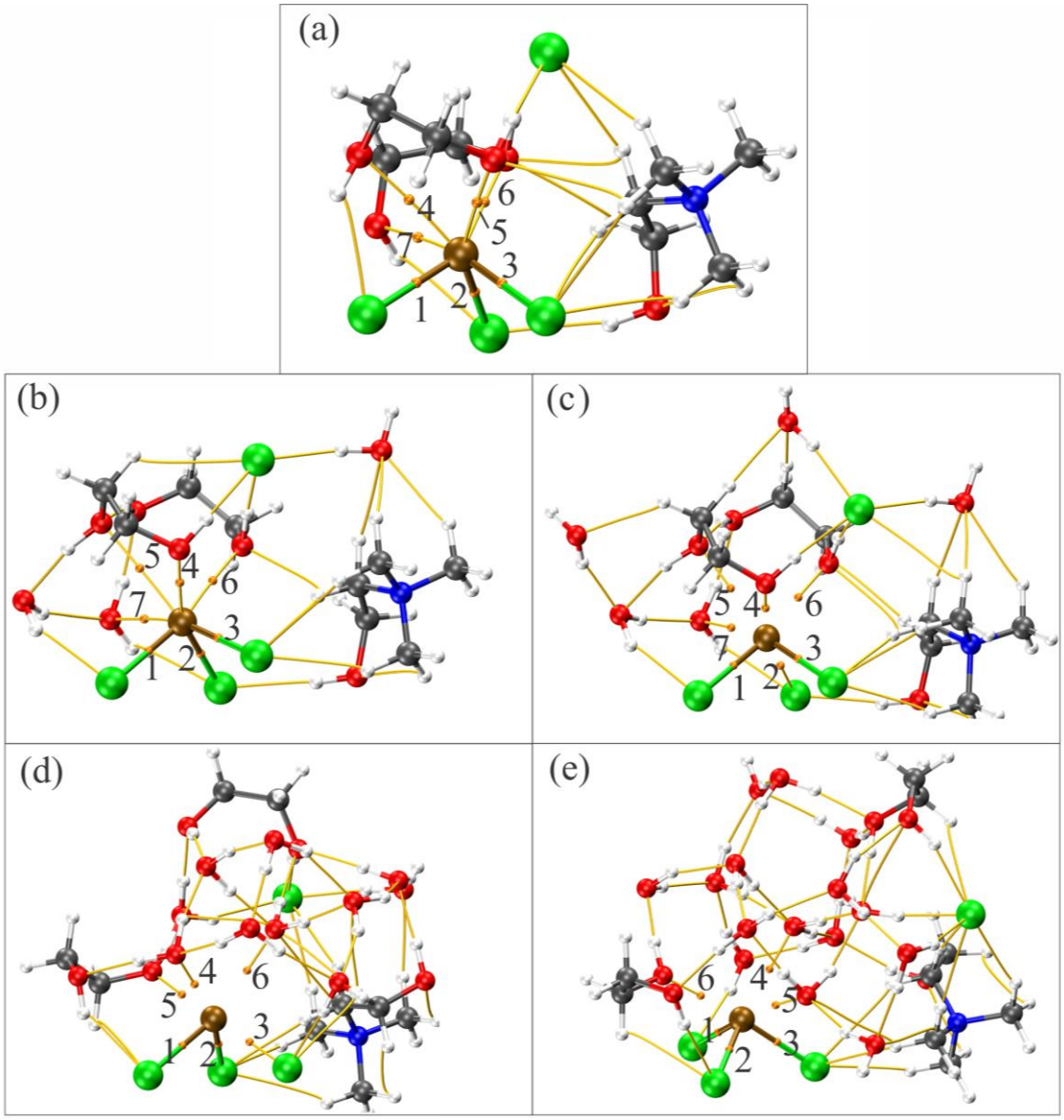

Fig. 7. The molecular graphs Sb^{3+} BCPs of the studied system without H_2O molecules (a), 3 H_2O molecules (b), 5 H_2O molecules (c), 10 H_2O molecules (d), and 15 H_2O molecules (e) were obtained by QTAIM analysis.

The NCI study was carried out to ascertain each system's intermolecular interactions. Comparing each system, initially in the system without water (Fig. 8(a)), a greater amount of green isosurfaces was observed, indicating a predominance of Van der Waals forces. With the addition of H_2O to the systems Fig. 8(b), Fig. 8(c), Fig. 8(d) and Fig. 8(e), the most significant number of strong intermolecular interactions is highlighted by the blue density, following an upward trend up to system E (Fig. 8(e)). This is related to the addition of intermolecular interactions of the hydrogen bond type carried out by H_2O - H_2O and H_2O - HO in EG [62]. In addition, H_2O carries out moderate-strength Van der Waals-type interactions with

the $SbCl_3$ complex in systems D (Fig. 8(d)) and E (Fig. 8(e)). The increase in H_2O also ensures an increase in the number of strong interactions with the Cl^- ion in DES.

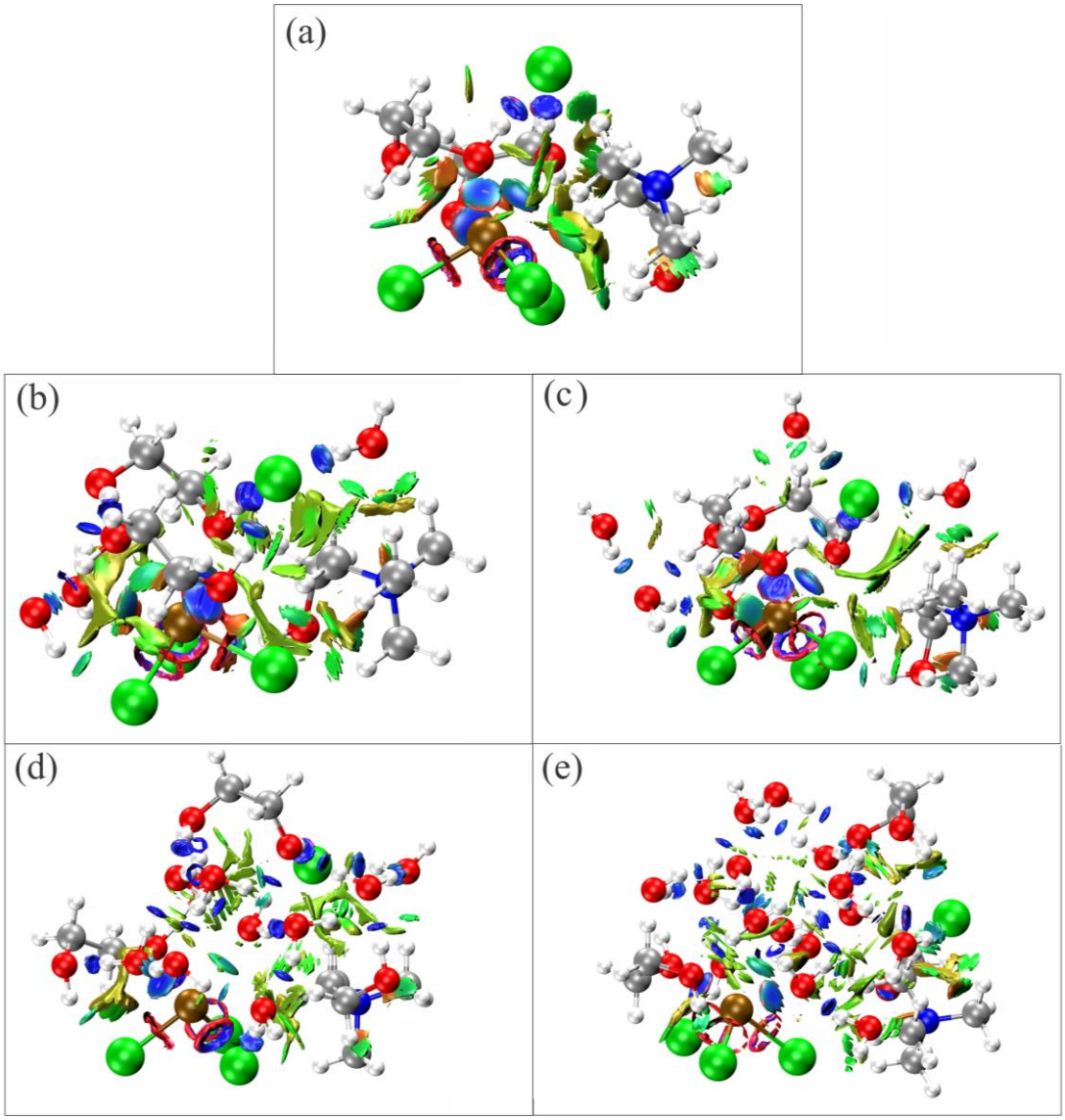

Fig. 8. RDG isosurface for Intermolecular interactions for molecules of the system without H_2O molecules (a), 3 H_2O molecules (b), 5 H_2O molecules (c), 10 H_2O molecules (d), and 15 H_2O molecules (e).

The Cl^- ion performs strong interactions in the system, being related to its negative charge, interacting with the partially positive hydrogens of the hydroxyls of EG (Fig. 8(a)), remaining with the addition of H_2O. The DES urea molecule has moderate Van der Waals interactions in all systems. The map of RDG vs. (λ_2) ρ on the X and Y axes, respectively, Fig. 9, indicates a decrease in the repulsive effect with increasing H_2O, represented with red dots

highlighted in the yellow circles, with a higher density of points up to 0. 015 a.u (Fig. 9(a)), the density decreasing with an increase of 3 H_2O (Fig. 9(b)), remaining at an increase of 5 and 10 H_2O (Fig. 9(c-d)), reaching a minimum of 0.010 a.u. at 15 H_2O (Fig. 9(d)). There was also an increase in the strong intermolecular effect, represented with blue dots highlighted in the purple circles, with a higher density of dots at −0.040 a.u (Fig. 9(a)), with the density increasing to −0.045 a.u. with an increase of 3 H_2O (Fig. 9(b)), remaining at an increase of 5 H_2O (Fig. 9(c)), reaching a maximum of value −0.050 a.u., in the system with 10 and 15 H_2O with RDG 0.2 (Fig. 9(d-e)).

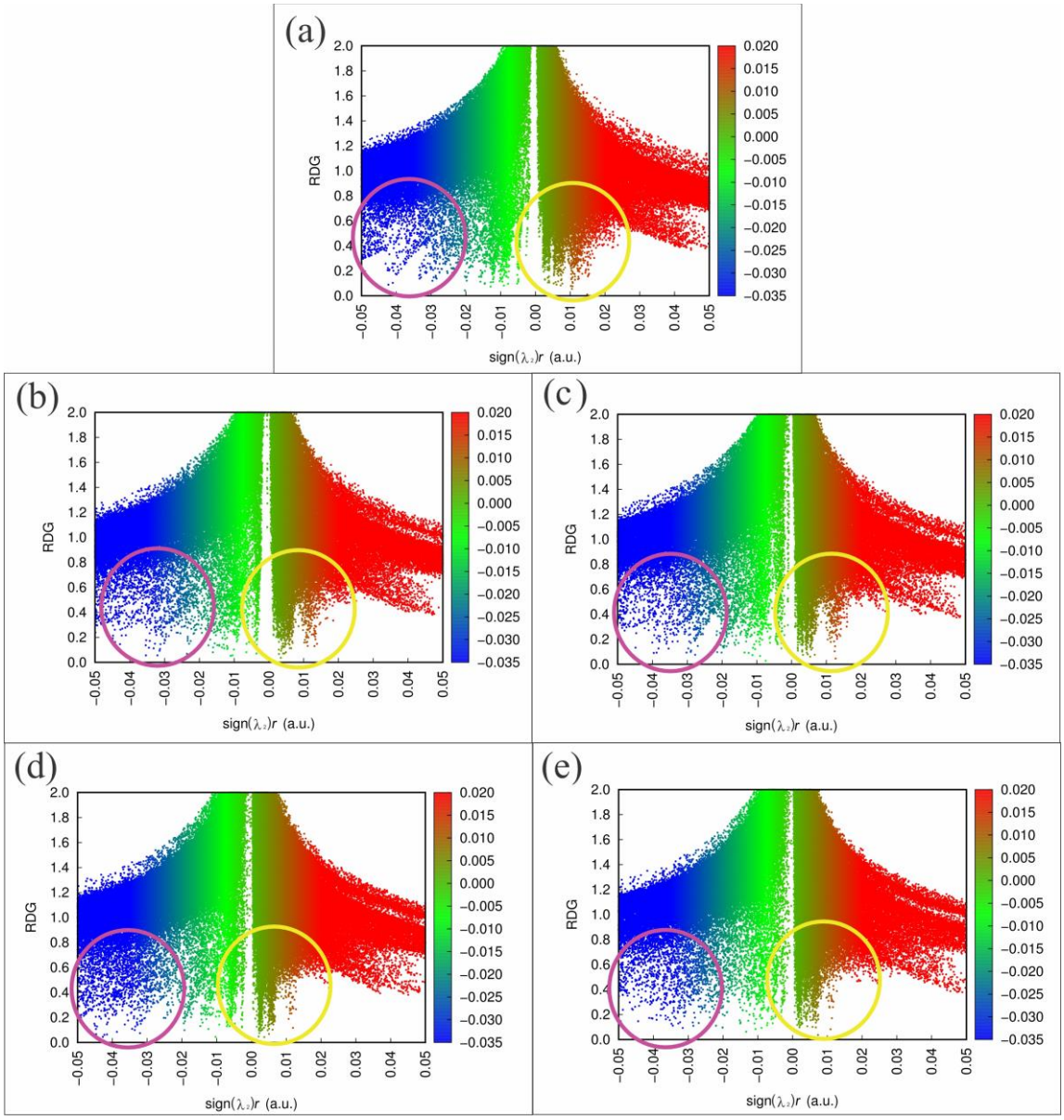

Fig. 9. RDG vs. sign(λ_2)ρ from the results of the NCI of the molecules of the system without H_2O molecules (a), 3 H_2O molecules (b), 5 H_2O molecules (c), 10 H_2O molecules (d), and 15 H_2O molecules (e).

4 Conclusions

The eutectic mixture based on choline chloride-ethylene glycol in the absence and presence of water was successfully used in this study for electrodeposition of Sb on Pt surface at 297 K and 338 K without the necessity to add complex additives. The cyclic voltammogram performed on the Pt electrode of the electrolyte solution containing the Sb^{3+} showed, in the direct scan, a well-defined cathode peak corresponding to the reduction of Sb^{3+}/Sb. SEM analysis showed similar dendritic morphologies for Sb films obtained with water addition at 297 K. Meanwhile, sheet structures for all Sb films at 338 K were obtained. Finally, XRD characterization revealed that the Sb electrodeposits had a rhombohedral crystalline structure with pure phases for all samples. The DFT simulations for DES and $SbCl_3$ systems without H_2O and with varying amounts of H_2O molecules favoured the system in increasing electron affinity. Furthermore, there was a strong tendency for H_2O to be added, causing a decrease in the electronic density of the Sb^{3+} ions with the atoms in all the studied systems. These results indicated a possible explanation for electrodeposition being favoured in this type of system's presence of H_2O molecules. This work is also expected to serve as a basis for obtaining Sb films with varied structures with promising properties and potential applications in the wide range of uses of Sb and its alloys. Lastly, the quantum computational simulations indicated that the Sb-Cl interaction is stronger, which suggests the formation of Sb-Cl complexes and that the addition of water molecules favours the electron affinity of the systems, and QTAIM results suggested that this additive decreased the electron density of Sb^{3+} ions.

Acknowledgements

This study was financed in part by the Coordenação de Aperfeiçoamento de Pessoal de Nível Superior - Brasil (CAPES) – Finance Code 001. The authors thank the financial support given by the following Brazilian funding agencies: Coordenação de Aperfeiçoamento de Pessoal de Nível Superior (CAPES), Conselho Nacional de Desenvolvimento Científico e Tecnológico (CNPq) and Fundação Cearense de Apoio ao Desenvolvimento Científico e Tecnológica (FUNCAP). A.N. Correia gratefully acknowledges the funding provided by CNPq (proc. 305103/2022-9). P. de Lima-Neto thanks the financial support received from CNPq (proc. 302825/2022-3). Ana. A. C. Alcanfor thanks CAPES for her grants. The authors thank the Central Analítica-UFC/CT-INFRA/MCTI-SISANO/Pró-Equipamentos CAPES and Laboratório de Raios-X (UFC) for their support. The authors also thank Centro Nacional de Processamento de Alto Desempenho (CENAPAD) of the Federal University of Ceará (UFC) for providing computational resources.

Data availability

The raw/processed data required to reproduce these findings, cannot be shared at this time as the data also forms part of an ongoing study.

Credit authorship contribution statement

Pedro de Lima Neto: conceptualization, methodology, validation, investigation, Writing - original draft review & editing, funding acquisition. **Adriana N. Correia:** investigation, review the original draft, funding acquisition. **Ana Aline C. Alcanfor**: methodology, investigation, data analyses and review the original draft. **Leonardo P. da Silva**: methodology, validation, investigation. **Raíssa C. de Oliveira**: methodology, validation, investigation. **Gabrielle A. Paulo**: investigation, methodology and data analyses. **Othon S. Campos**: investigation, data analyses and review the original draft. **Diego F. Dias**: methodology, validation, and data analyses. **Filipe X. Feitosa**: methodology, validation, investigation. **Hosiberto B. de Sant'Ana**: methodology, validation, and investigation. **Norberto K. V. Monteiro**: methodology, validation, investigation.

Declaration of Competing Interest

The authors report no declarations of interest.

References

[1] A.W. Black, W. Zhang, Y.J. Noori, G. Reid, P.N. Bartlett, Temperature effects on the electrodeposition of semiconductors from a weakly coordinating solvent, J. Electroanal. Chem. 944 (2023) 117638. https://doi.org/10.1016/j.jelechem.2023.117638.

[2] S. Cho, J. Lim, Y. Seo, Fabrication of Bismuth-Antimony-Telluride Alloy/Poly(3,4-ethylenedioxythiophene) Hybrid Films for Thermoelectric Applications at Room Temperature by a Simple Electrochemical Process, Chem. Mater. 35 (2023) 3196–3205. https://doi.org/10.1021/acs.chemmater.3c00001.

[3] F.W.S. Lucas, F.H.B. Lima, Electrodeposited Tin-Antimony Alloys as Novel Electrocatalysts for Selective and Stable Carbon Dioxide Reduction to Formate, ChemElectroChem 7 (2020) 3733–3742. https://doi.org/10.1002/celc.202000769.

[4] K. Nieto, D.S. Windsor, A.R. Kale, J.R. Gallawa, D.A. Medina, A.L. Prieto, Structural Control of Electrodeposited Sb Anodes through Solution Additives and Their Influence on Electrochemical Performance in Na-Ion Batteries, J. Phys. Chem. C (2023). https://doi.org/10.1021/acs.jpcc.3c01086.

[5] H.R. Shen, X.Y. Han, X.M. Zheng, B. Muniyandi, J.K. Wang, Q.L. Kang, M.G. Chen, Q. Wu, P.Y. Zhang, One-step electrochemical synthesis and optimization of Sb-Co-P alloy anode for sodium ion battery, Electrochim. Acta 438 (2023) 141529. https://doi.org/10.1016/j.electacta.2022.141529.

[6] H. Jung, N. V. Myung, Electrodeposition of antimony telluride thin films from acidic nitrate-tartrate baths, Electrochim. Acta 56 (2011) 5611–5615. https://doi.org/10.1016/j.electacta.2011.04.010.

[7] J. Schoenleber, N. Stein, C. Boulanger, Influence of tartaric acid on diffusion coefficients of BiIII, SbIII, TeIV in aqueous medium: Application of electrodeposition of thermoelectric films, J. Electroanal. Chem. 724 (2014) 111–117. https://doi.org/10.1016/j.jelechem.2014.04.004.

[8] V.A. Majidzade, P.H. Guliyev, A.S. Aliyev, M. Elrouby, D.B. Tagiyev, Electrochemical characterization and electrode kinetics for antimony electrodeposition from its oxychloride solution in the presence of tartaric acid, J. Mol. Struct. 1136 (2017) 7–13. https://doi.org/10.1016/j.molstruc.2017.01.082.

[9] Y. Lin, P. Ning, Y. Cui, C. Zhang, M. Xu, P. Dong, Z. Zhou, Y. Zhang, Electrodeposition behaviour of antimony in H2SO4-NH4F-SbF3 solutions, Int. J. Electrochem. Sci. 14 (2019) 4003–4019. https://doi.org/10.20964/2019.03.33.

[10] L. Hernández-Pérez, J. Carrillo-Abad, V. Pérez-Herranz, M.T. Montañés, M.C. Martí-Calatayud, Effluents from the copper electrorefining as a secondary source of antimony: Role of mass transfer on the recovery by electrodeposition, Desalination 549 (2023). https://doi.org/10.1016/j.desal.2022.116322.

[11] W. Liu, T.Z. Yang, Q.H. Zhou, D.C. Zhang, C.M. Lei, Electrodeposition of Sb(III) in alkaline solutions containing xylitol, Trans. Nonferrous Met. Soc. China (English Ed. 22 (2012) 949–957. https://doi.org/10.1016/S1003-6326(11)61269-7.

[12] Q. Wang, Y. Wang, Fundamental Electrochemical Behavior of Antimony in Alkaline Solution, J. Sustain. Metall. 5 (2019) 606–616. https://doi.org/10.1007/s40831-019-00253-7.

[13] L. Hernández-Pérez, J. Carrillo-Abad, E.M. Ortega, V. Pérez-Herranz, M.T. Montañés, M.C. Martí-Calatayud, Voltammetric and electrodeposition study for the recovery of antimony from effluents generated in the copper electrorefining process, J. Environ. Chem. Eng. 11 (2023). https://doi.org/10.1016/j.jece.2022.109139.

[14] M.H. Yang, I.W. Sun, Electrodeposition of antimony in a water-stable 1-ethyl-3-methylimidazolium chloride tetrafluoroborate room temperature ionic liquid, J. Appl. Electrochem. 33 (2003) 1077–1084. https://doi.org/10.1023/A:1026223314259.

[15] W. Yang, H. Cang, Y. Tang, J. Wang, Y. Shi, Electrodeposition of tin and antimony in 1-ethyl- 3-methylimidazolium tetrafluoroborate ionic liquid, J. Appl. Electrochem. 38 (2008) 537–542. https://doi.org/10.1007/s10800-007-9470-6.

[16] Y.-T. Hsieh, Y.-C. Chen, I.-W. Sun, 1-Butyl-1-Methylpyrrolidinium Dicyanamide Room Temperature Ionic Liquid for Electrodeposition of Antimony, J. Electrochem. Soc. 163 (2016) D188–D193. https://doi.org/10.1149/2.0051606jes.

[17] Y.T. Hsieh, Y.C. Liu, N.C. Lo, W.J. Lin, I.W. Sun, Electrochemical co-deposition of gallium and antimonide from the 1-butyl-1-methylpyrrolidinium dicyanamide room temperature ionic liquid, J. Electroanal. Chem. 832 (2019) 48–54. https://doi.org/10.1016/j.jelechem.2018.10.034.

[18] R. Bernasconi, G. Panzeri, A. Accogli, F. Liberale, L. Nobili, L. Magagnin, Electrodeposition from deep eutectic solvents, Intech. Prog. Dev. Lon. Liq (2017) 235–261.

[19] A.P. Abbott, Deep eutectic solvents and their application in electrochemistry, Curr. Opin. Green Sustain. Chem. 36 (2022) 100649. https://doi.org/10.1016/j.cogsc.2022.100649.

[20] M.L. Mares, F. Golgovici, T. Visan, RDE voltammetry and impedance spectroscopy studies of Sb, Te and SbTe electrodeposition from choline chloride - Urea ionic liquids, Chalcogenide Lett. 10 (2013) 259–272.

[21] A.C. Rastogi, N.R. Janardhana, Properties of CuSbS2 thin films electrodeposited from ionic liquids as p-type absorber for photovoltaic solar cells, Thin Solid Films 565 (2014) 285–292. https://doi.org/10.1016/j.tsf.2014.06.031.

[22] A.S. Catrangiu, I. Sin, P. Prioteasa, A. Cotarta, A. Cojocaru, L. Anicai, T. Visan, Studies of antimony telluride and copper telluride films electrodeposition from choline chloride containing ionic liquids, Thin Solid Films 611 (2016) 88–100.

https://doi.org/10.1016/j.tsf.2016.04.030.

[23] Z. Su, C. Xu, Y. Hua, J. Li, J. Ru, M. Wang, L. Xiong, Y. Zhang, Electrochemical preparation of sub-micrometer Sn-Sb alloy powder in ChCl-EG deep eutectic solvent, Int. J. Electrochem. Sci. 11 (2016) 3325–3338. https://doi.org/10.20964/110446.

[24] N. Su, S. Guo, F. Li, D. Liu, B. Li, Electrodeposition of p-Type Sb2Te3 films and micro-pillar arrays in a multi-channel glass template, Materials (Basel). 11 (2018). https://doi.org/10.3390/ma11071194.

[25] J. Bu, J. Ru, Z. Wang, Y. Hua, C. Xu, Y. Zhang, Y. Wang, Controllable preparation of antimony powders by electrodeposition in choline chloride-ethylene glycol, Adv. Powder Technol. 30 (2019) 2859–2867. https://doi.org/10.1016/j.apt.2019.06.027.

[26] Y. Sun, S. Cheng, Z. Mao, Z. Lin, X. Ren, Z. Yu, High electrochemical activity of a Ti/SnO2–Sb electrode electrodeposited using deep eutectic solvent, Chemosphere 239 (2020) 124715. https://doi.org/10.1016/j.chemosphere.2019.124715.

[27] J. Bu, J. Ru, Y. Hua, Z. Wang, Y. Zhang, X. Geng, W. Zhang, Electrochemical behavior of Sb(III)/Sb during the preparation of Sb particles in deep eutectic solvent, Ionics (Kiel). 27 (2021) 3119–3127. https://doi.org/10.1007/s11581-021-04048-3.

[28] Z. Zhang, Z. Wang, Y. Sun, S. Jiang, L. Shi, Q. Bi, J. Xue, Preparation of a novel Ni/Sb co-doped Ti/SnO2 electrode with carbon nanotubes as growth template by electrodeposition in a deep eutectic solvent, J. Electroanal. Chem. 911 (2022) 116225. https://doi.org/10.1016/j.jelechem.2022.116225.

[29] S. Liu, Z. Tan, J. Wu, B. Mao, J. Yan, Electrochemical interfaces in ionic liquids/deep eutectic solvents incorporated with water: A review, Electrochem. Sci. Adv. (2022) 1–9. https://doi.org/10.1002/elsa.202100199.

[30] A.Y.M. Al-Murshedi, J.M. Hartley, A.P. Abbott, K.S. Ryder, Effect of water on the electrodeposition of copper on nickel in deep eutectic solvents, Trans. Inst. Met. Finish. 97 (2019) 321–329. https://doi.org/10.1080/00202967.2019.1671062.

[31] P.E. Valverde, T.A. Green, S. Roy, Effect of water on the electrodeposition of copper from a deep eutectic solvent, J. Appl. Electrochem. 50 (2020) 699–712. https://doi.org/10.1007/s10800-020-01408-1.

[32] M. Lukaczynska, E.A. Mernissi Cherigui, A. Ceglia, K. Van Den Bergh, J. De Strycker, H. Terryn, J. Ustarroz, Influence of water content and applied potential on the electrodeposition of Ni coatings from deep eutectic solvents, Electrochim. Acta 319 (2019) 690–704. https://doi.org/10.1016/j.electacta.2019.06.161.

[33] J.R. Bezerra-Neto, L.L. Bezerra, N.G. Sousa, L.P.M. dos Santos, E.S. Marinho, N.K.V. Monteiro, A.N. Correia, P. de Lima-Neto, Molecular approach about the effect of water on the electrochemical behaviour of Ag+ ions in urea-choline chloride-water mixture, J. Mol. Model. 26 (2020). https://doi.org/10.1007/s00894-020-04587-y.

[34] Q. Xiang, C. Xu, X. Chen, S. Wang, J. Lu, J. Li, Y. Hua, Effect of water on electrodeposition behavior of zinc in a ChCl-urea-ZnO deep eutectic system, J. Solid State Electrochem. 26 (2022) 2353–2363. https://doi.org/10.1007/s10008-022-05250-7.

[35] J.R. Bezerra-Neto, N.G. Sousa, L.P.M. Dos Santos, A.N. Correia, P. De Lima-Neto, The effect of water on the physicochemical properties of an ethylene glycol and choline chloride mixture containing Cu^{2+} ions: Electrochemical results and dynamic molecular simulation approach, Phys. Chem. Chem. Phys. 20 (2018) 9321–9327. https://doi.org/10.1039/c7cp05911f.

[36] S. Rozas, M. Atilhan, S. Aparicio, A density functional theory based tight-binding study on the water effect on nanostructuring of choline chloride + ethylene glycol deep eutectic solvent, J. Chem. Phys. 156 (2022). https://doi.org/10.1063/5.0091665.

[37] D.M.L. Pinheiro, L.L. Bezerra, A.A.C. Alcanfor, F.X. Feitosa, N.K.V. Monteiro, A.N. Correia, P. de Lima Neto, H.B. de Sant'Ana, Ag^{+} ion in choline chloride and glycerol mixture: Evaluation of electrochemical properties and molecular modelling approaches, J. Mol. Liq. 371 (2023) 121053. https://doi.org/10.1016/j.molliq.2022.121053.

[38] A.P. Abbott, D. Boothby, G. Capper, D.L. Davies, R.K. Rasheed, Deep Eutectic Solvents Formed between Choline Chloride and Carboxylic Acids : Versatile Alternatives to Ionic Liquids, J. Am. Chem. Soc. 126 (2004) 9142–9147.

[39] C. Bannwarth, S. Ehlert, S. Grimme, GFN2-xTB - An Accurate and Broadly Parametrized Self-Consistent Tight-Binding Quantum Chemical Method with Multipole Electrostatics and Density-Dependent Dispersion Contributions, J. Chem. Theory Comput. 15 (2019) 1652–1671. https://doi.org/10.1021/acs.jctc.8b01176.

[40] T. Lu, Molclus program, Beijing Kein Res. Cent. Nat. Sci. China (2016).

[41] F. Weigend, R. Ahlrichs, Balanced basis sets of split valence, triple zeta valence and quadruple zeta valence quality for H to Rn: Design and assessment of accuracyElectronic supplementary information (ESI) available:[DETAILS]. See http://dx. doi. org/10.1039/b508541a, Phys. Chem. Chem. Phys. 7 (2005) 3297–3305.

[42] F. Weigend, Accurate Coulomb-fitting basis sets for H to Rn, Phys. Chem. Chem. Phys. 8 (2006) 1057–1065. https://doi.org/10.1039/b515623h.

[43] F. Neese, Software update: the ORCA program system, version 4.0, Wiley Interdiscip. Rev. Comput. Mol. Sci. 8 (2018) 1–6. https://doi.org/10.1002/wcms.1327.

[44] F. Neese, F. Wennmohs, U. Becker, C. Riplinger, The ORCA quantum chemistry program package, J. Chem. Phys. 152 (2020). https://doi.org/10.1063/5.0004608.

[45] A.P. Gaiduk, T.A. Pham, M. Govoni, F. Paesani, G. Galli, Electron affinity of liquid water, Nat. Commun. 9 (2018) 4–9. https://doi.org/10.1038/s41467-017-02673-z.

[46] Y. Takahata, D.P. Chong, Density-Functional Calculations of Molecular Electron

Affinities, J. Braz. Chem. Soc. 10 (1999) 354–358. https://doi.org/10.1590/S0103-50531999000500003.

[47] R.F.W. Bader, S.G. Anderson, A.J. Duke, Quantum Topology of Molecular Charge Distributions, J. Am. Chem. Soc. 101 (1979) 1389–1395. https://doi.org/10.1021/ja00500a006.

[48] C.F. Matta, R.J. Boyd, An Introduction to the Quantum Theory of Atoms in Molecules, 2007. https://doi.org/10.1002/9783527610709.ch1.

[49] T. Lu, F. Chen, Multiwfn: A multifunctional wavefunction analyzer, J. Comput. Chem. 33 (2012) 580–592. https://doi.org/10.1002/jcc.22885.

[50] W. Humphrey, A. Dalke, K. Schulten, Sartorius products, J. Mol. Graph. 14 (1996) 33–38.

[51] L. Vieira, R. Schennach, B. Gollas, The effect of the electrode material on the electrodeposition of zinc from deep eutectic solvents, Electrochim. Acta 197 (2016) 344–352. https://doi.org/10.1016/j.electacta.2015.11.030.

[52] J.M. Hartley, C.-M. Ip, G.C.H. Forrest, K. Singh, S.J. Gurman, K.S. Ryder, A.P. Abbott, G. Frisch, EXAFS Study into the Speciation of Metal Salts Dissolved in Ionic Liquids and Deep Eutectic Solvents, Inorg. Chem. 53 (2014) 6280–6288. https://doi.org/10.1021/ic500824r.

[53] E.H. Oelkers, D.M. Sherman, K.V. Ragnarsdottir, C. Collins, An EXAFS spectroscopic study of aqueous antimony(III)-chloride complexation at temperatures from 25 to 250°C, Chem. Geol. 151 (1998) 21–27. https://doi.org/10.1016/S0009-2541(98)00067-9.

[54] A.L. Pitman, M. Pourbaix, N. de Zoubov, Potential-pH Diagram of the Antimony-Water System, J. Electrochem. Soc. 104 (1957) 594. https://doi.org/10.1149/1.2428423.

[55] D. Rajska, A. Brzózka, K.E. Hnida-Gut, G.D. Sulka, Investigation of electrodeposition kinetics of In, Sb, and Zn for advanced designing of InSb and ZnSb thin films, J. Electroanal. Chem. 882 (2021). https://doi.org/10.1016/j.jelechem.2020.114967.

[56] S. Wei, M. Zhang, W. Han, Y. Yan, Y. Xue, M. Zhang, B. Zhang, Electrochemical behavior of antimony and electrodeposition of Mg-Li-Sb alloys from chloride melts, Electrochim. Acta 56 (2011) 4159–4166. https://doi.org/10.1016/j.electacta.2011.01.104.

[57] L. Amorim, R.V. de Oliveira, L.L. Bezerra, L.P. Coutinho, P.B.A. Fechine, A.N. Correia, Á.R.L. da Silva, P. de Lima-Neto, N.K. de V. Monteiro, Analysis of Fe2+ and Mn2+ ions in DES and water: A theoretical study using molecular dynamic simulations, QTAIM and NCI-RDG, Colloids Surfaces A Physicochem. Eng. Asp. 674 (2023) 131818. https://doi.org/10.1016/j.colsurfa.2023.131818.

[58] T. Müller, S. Sharma, E.K.U. Gross, J.K. Dewhurst, Extending Solid-State Calculations to Ultra-Long-Range Length Scales, Phys. Rev. Lett. 125 (2020) 256402. https://doi.org/10.1103/PhysRevLett.125.256402.

[59] C. Ma, A. Laaksonen, C. Liu, X. Lu, X. Ji, The peculiar effect of water on ionic liquids and deep eutectic solvents, Chem. Soc. Rev. 47 (2018) 8685–8720. https://doi.org/10.1039/c8cs00325d.

[60] J. Zhao, G. Gorbatovski, O. Oll, E. Anderson, E. Lust, Influence of water on the electrochemical characteristics and nanostructure of Bi(hkl) │Ionic liquid interface, Electrochim. Acta 415 (2022) 140263. https://doi.org/10.1016/j.electacta.2022.140263.

[61] R.F.W. Bader, J.R. Cheeseman, K.E. Laidig, K.B. Wiberg, C. Breneman, Origin of Rotation and Inversion Barriers, J. Am. Chem. Soc. 112 (1990) 6530–6536. https://doi.org/10.1021/ja00174a012.

[62] I. Rozas, I. Alkorta, J. Elguero, Behavior of ylides containing N, O, and C atoms as hydrogen bond acceptors, J. Am. Chem. Soc. 122 (2000) 11154–11161. https://doi.org/10.1021/ja0017864.

[63] G. LI, Y. XIN, X. LÜ, Q. TIAN, K. YAN, L. YE, Stability constants of Sb5+ with Cl− and thermodynamics of Sb−S−Cl−H2O system involving complex behavior of Sb with Cl, Trans. Nonferrous Met. Soc. China 30 (2020) 3379–3389. https://doi.org/10.1016/S1003-6326(20)65469-3.

[64] Z. Su, Electrochemical Preparation of Sub-micrometer Sn-Sb Alloy powder in ChCl-EG deep eutectic solvent, Int. J. Electrochem. Sci. (2016) 3325–3338. https://doi.org/10.20964/110446.

[65] E. Rudnik, M. Kostępski, Comparative Studies on the Codeposition of Antimony and Tin from Acidic Chloride and Sulfate-Chloride Solutions, Arch. Metall. Mater. (2018). https://doi.org/10.24425/122397.

Supplementary material

On the role of water in antimony electrodeposition from choline chloride/ethylene glycol/water mixture

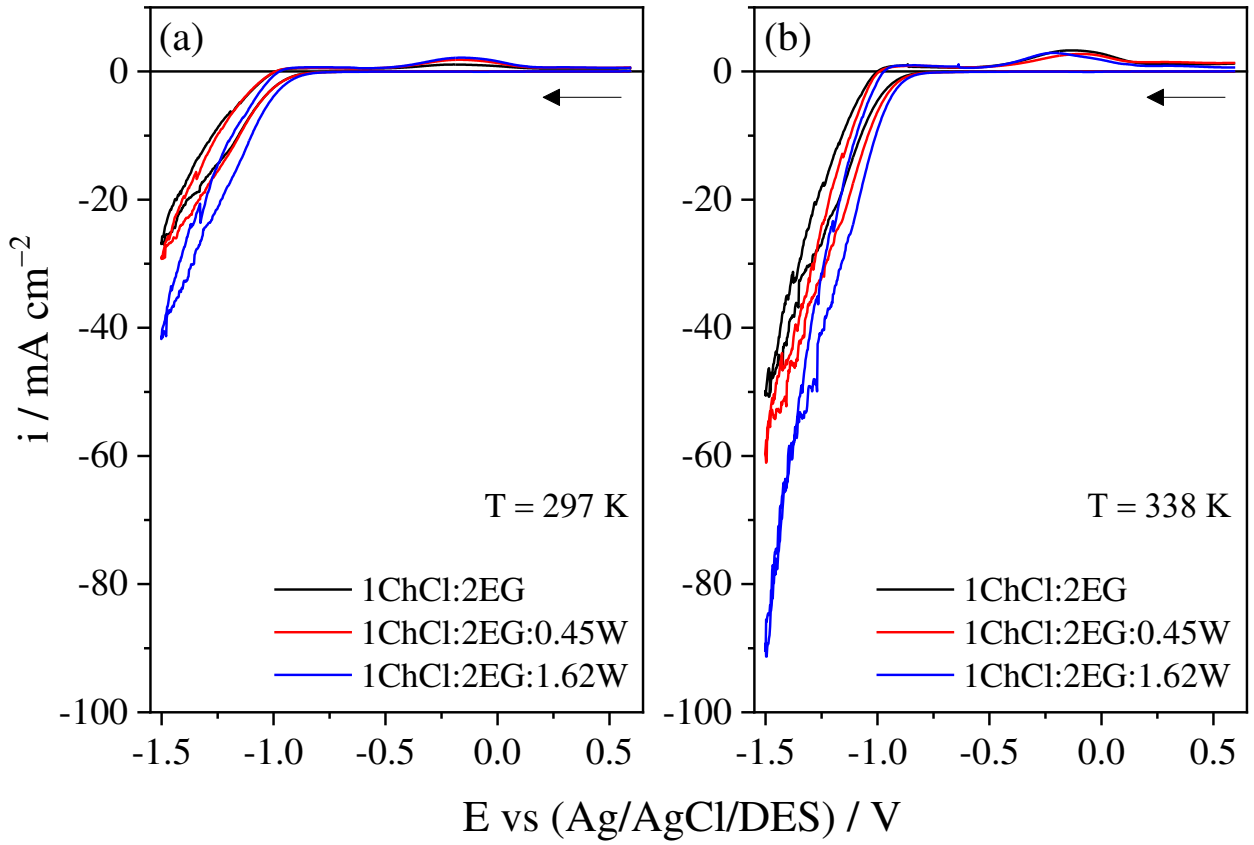

Fig. S1. Cyclic voltammograms obtained on Pt electrode immersed in 1ChCl:2EG, 1ChCl:2EG:0.45W and 1ChCl:2EG:1.62W at 297 K (a) and 338 K (b). All cyclic voltammograms were obtained at 25 mV s^{-1}.

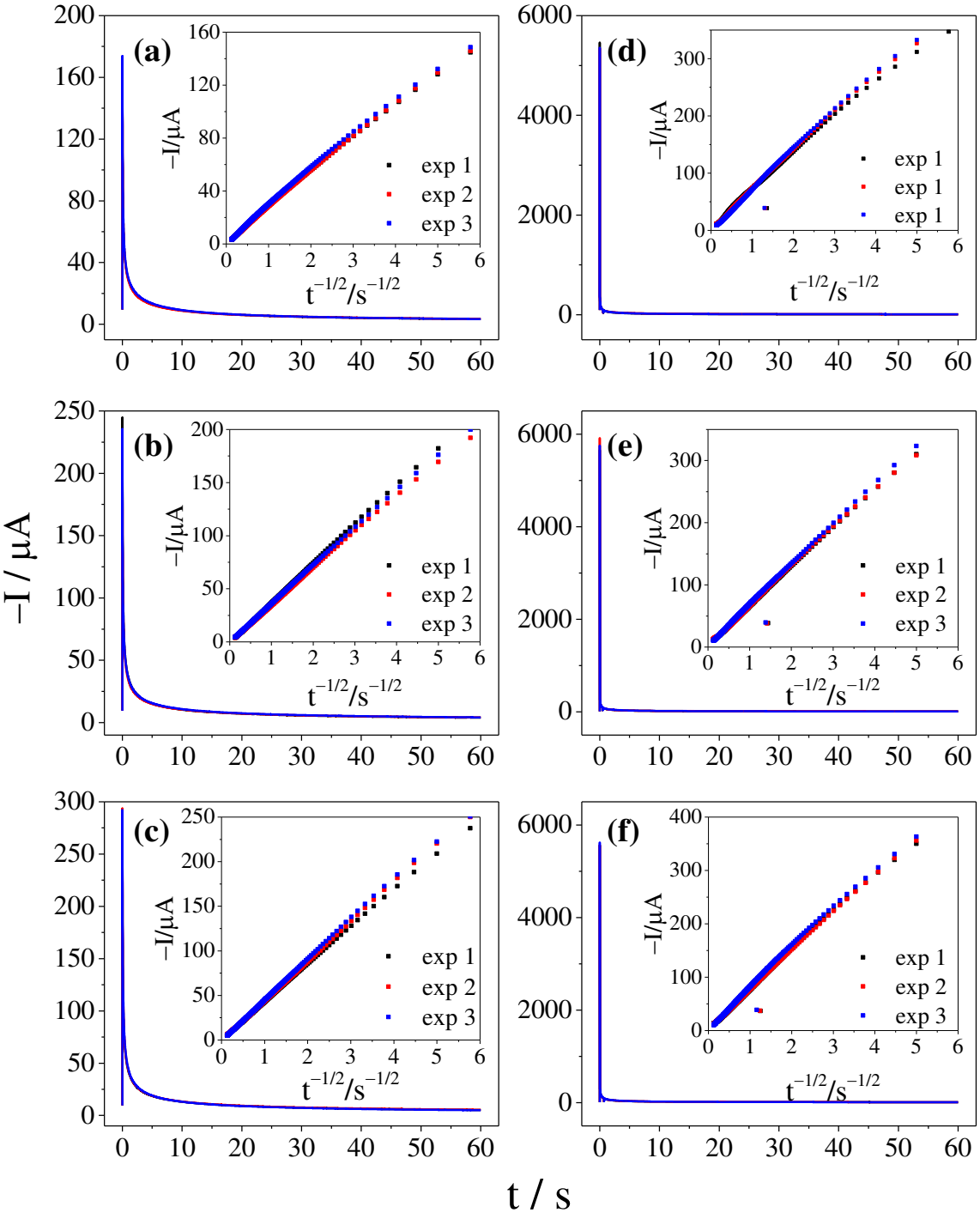

Fig. S2. Current *versus* time transients for the reduction of Sb^{3+}/Sb on Pt electrode in baths 1, 2 and 3 containing 0.05 mol L^{-1} $SbCl_3$ at 297 K (a-c) and 338 K (d-f) at an applied potential of –1.0 V for 60 s in triplicate. The inset graphs show Cottrell´s plots.

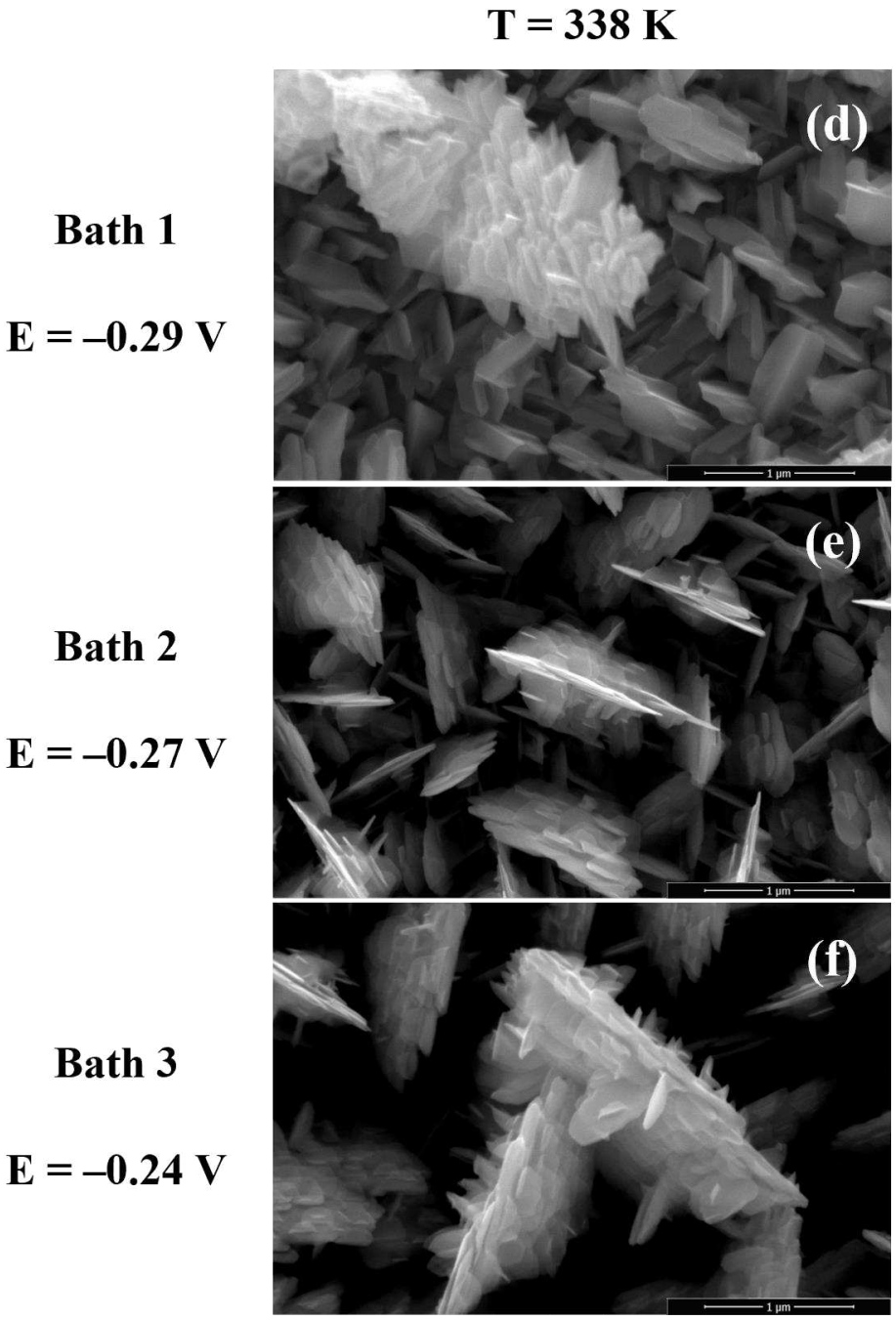

Fig. S3. SEM micrographs of Sb electrodeposits onto Pt electrode at 338 K obtained under potentiostatic control at (d) –0.29 V, (e) –0.27 V and (f) –0.24 V for 1800 s, in baths 1, 2 and 3 containing 0.05 mol L^{-1} $SbCl_3$. SEM scale bar 1 micron.

Table S1. The Electron density (ρ_b), Laplacian of the electron density ($\nabla^2\rho_b$) and Energy density (H_b) at Bond Critical Points (BCPs) of Sb^{3+} bonding from system A. All values are in a.u..

BCP	$\boldsymbol{\rho_b}$	$\boldsymbol{\nabla^2\rho_b}$	$\boldsymbol{H_b}$
1	7.78×10^{-2}	9.72×10^{-2}	-2.50×10^{-2}
2	6.51×10^{-2}	8.00×10^{-2}	-1.76×10^{-2}
3	6.79×10^{-2}	8.61×10^{-2}	-1.91×10^{-2}
4	2.03×10^{-2}	4.93×10^{-2}	1.46×10^{-4}
5	2.95×10^{-2}	6.41×10^{-2}	-1.76×10^{-3}
6	2.52×10^{-2}	5.85×10^{-2}	-7.43×10^{-4}
7	3.32×10^{-2}	7.04×10^{-2}	-3.01×10^{-3}
$\Sigma\rho_b$	0.319	0.506	–0.067

Table S2. The Electron density (ρ_b), Laplacian of the electron density ($\nabla^2\rho_b$) and Energy density (H_b) at Bond Critical Points (BCPs) of Sb^{3+} bonding from system B. All values are in a.u..

BCP	$\boldsymbol{\rho_b}$	$\boldsymbol{\nabla^2\rho_b}$	$\boldsymbol{H_b}$
1	7.36×10^{-2}	9.35×10^{-2}	-2.24×10^{-2}
2	6.33×10^{-2}	7.81×10^{-2}	-1.66×10^{-2}
3	7.28×10^{-2}	9.13×10^{-2}	-2.19×10^{-2}
4	3.55×10^{-2}	7.37×10^{-2}	-3.54×10^{-3}
5	1.62×10^{-2}	4.06×10^{-2}	6.94×10^{-4}
6	3.15×10^{-2}	7.23×10^{-2}	-2.16×10^{-3}
7	2.37×10^{-2}	5.35×10^{-2}	-6.71×10^{-4}
$\Sigma\rho_b$	0.317	0.503	–0.067

Table S3. The Electron density (ρ_b), Laplacian of the electron density ($\nabla^2\rho_b$) and Energy density (H_b) at Bond Critical Points (BCPs) of Sb^{3+} bonding/interaction from system C. All values are in a.u..

BCP	$\boldsymbol{\rho_b}$	$\boldsymbol{\nabla^2\rho_b}$	$\boldsymbol{H_b}$
1	7.45×10^{-2}	9.42×10^{-2}	-2.29×10^{-2}
2	5.96×10^{-2}	7.50×10^{-2}	-1.47×10^{-2}
3	7.33×10^{-2}	9.14×10^{-2}	-2.22×10^{-2}
4	3.95×10^{-2}	8.06×10^{-2}	-4.85×10^{-3}
5	2.04×10^{-2}	4.93×10^{-2}	1.48×10^{-4}
6	3.02×10^{-2}	7.04×10^{-2}	-1.78×10^{-3}
7	2.00×10^{-2}	4.66×10^{-2}	3.03×10^{-6}
$\Sigma\rho_b$	0.318	0.507	–0.066

Table S4. The Electron density (ρ_b), Laplacian of the electron density ($\nabla^2\rho_b$) and Energy density (H_b) at Bond Critical Points (BCPs) of Sb^{3+} bonding/interaction from system D. All values are in a.u..

BCP	$\boldsymbol{\rho_b}$	$\boldsymbol{\nabla^2\rho_b}$	$\boldsymbol{H_b}$
1	7.92×10^{-2}	9.77×10^{-2}	-2.58×10^{-2}
2	7.00×10^{-2}	8.87×10^{-2}	-2.02×10^{-2}
3	5.69×10^{-2}	7.68×10^{-2}	-1.32×10^{-2}
4	3.30×10^{-2}	6.75×10^{-2}	-2.96×10^{-3}
5	2.01×10^{-2}	5.42×10^{-2}	4.93×10^{-4}
6	5.36×10^{-2}	1.18×10^{-1}	-9.59×10^{-3}
$\Sigma\rho_b$	0.313	0.503	–0.071

Table S5. The Electron density (ρ_b), Laplacian of the electron density ($\nabla^2\rho_b$) and Energy density (H_b) at Bond Critical Points (BCPs) of Sb^{3+} bonding/interaction from system E. All values are in a.u..

BCP	$\boldsymbol{\rho_b}$	$\boldsymbol{\nabla^2\rho_b}$	$\boldsymbol{H_b}$
1	7.59×10^{-2}	9.77×10^{-2}	-2.37×10^{-2}
2	7.66×10^{-2}	9.46×10^{-2}	-2.41×10^{-2}
3	7.25×10^{-2}	9.39×10^{-2}	-2.16×10^{-2}
4	2.04×10^{-2}	5.07×10^{-2}	2.24×10^{-4}
5	2.90×10^{-2}	6.48×10^{-2}	-1.82×10^{-3}
6	3.71×10^{-2}	8.67×10^{-2}	-3.50×10^{-3}
$\Sigma\rho_b$	0.311	0.488	–0.075

3 MANUSCRITO 2: ELECTROCHEMICAL CORROSION EVALUATION OF SnSb ELECTRODEPOSITED COATINGS

Disponível em: https://doi.org/10.21577/0100-4042.20250086

Resumo

Os revestimentos de $Sn_xSb_{(1-x)}$ foram eletrodepositados a partir de 1ChCl:2EG em cobre. A resistência à corrosão dos eletrodepósitos foi avaliada em 0,1 mol dm^{-3} de NaCl. A caracterização foi realizada por microscopia eletrônica de varredura (MEV), espectroscopia de raios X por dispersão de energia (EDS) e difração de raios X (DRX). Os perfis voltamétricos mostraram que o potencial de eletrodeposição se deslocou para valores menos positivos com o aumento da concentração de Sb^{3+}. As imagens de MEV revelaram que os revestimentos exibiam grãos e cachos. As análises de EDS mostraram que o teor de Sb aumentou com a concentração de Sb^{3+}. Os resultados da DRX indicaram a formação das fases SbSn, como Cu_2Sb, Cu_6Sn_5 e $Cu_6(Sn,Sb)_5$. As curvas de polarização potenciodinâmica (PP) mostraram que Sn e $Sn_{77}Sb_{23}$ apresentaram uma região de potencial passivo, enquanto $Sn_{37}Sb_{63}$ apresentou uma dissolução ativa no eletrólito. Os testes de imersão foram realizados por 24 h e os resultados da DRX revelaram as fases, Sn, SnO, SbSn e Sb_2O_4. Considerando 48 h, foram identificadas as fases, CuSn, SnO_2 e SnSb. Os valores de resistência à polarização de 4.60, 14.69 e 1.81 kΩ cm^2 foram alcançados para Sn, $Sn_{77}Sb_{23}$ e $Sn_{37}Sb_{63}$, respectivamente. Os resultados do EIS sugeriram que a adição de Sb^{3+} melhora a resistência à corrosão para amostras de SnSb com maior teor de Sn. Para $Sn_{77}Sb_{23}$, a resistência à transferência de carga foi de 10.5 kΩ cm^2, para Sn e $Sn_{37}Sb_{63}$ 1.15 e 1.46 kΩ cm^2, respectivamente.

Palavras-chave: Revestimentos $Sn_xSb_{(1-x)}$; eletrodeposição; solvente eutético profundo; corrosão.

Abstract

$Sn_xSb_{(1-x)}$ coatings were electrodeposited from 1ChCl:2EG on copper. The corrosion resistance of the electrodeposits was evaluated in 0.1 mol dm^{-3} of NaCl. The characterization was performed by scanning electron microscopy (SEM), energy dispersive X-ray spectroscopy (EDS), and X-ray diffraction (XRD). Voltammetric profiles showed that the electrodeposition potential shifted towards less positive values with increasing Sb^{3+} concentration. SEM images revealed that the coatings exhibited grains and clusters. EDS analyses showed that the Sb content increased with the Sb^{3+} concentration. XRD results indicated the formation of the SbSn phases such as Cu_2Sb, Cu_6Sn_5, and $Cu_6(Sn,Sb)_5$. The potentiodynamic polarization (PP) curves showed that Sn and $Sn_{77}Sb_{23}$ presented a passive potential region, while $Sn_{37}Sb_{63}$ had an active dissolution in the electrolyte. Immersion tests were performed for 24 h and XRD results revealed Cu, Sn, SnO, SbSn and Sb_2O_4 phases. Considering 48 h, Cu, CuSn, SnO_2 and SnSb phases were identified. The polarization resistance values of 4.60, 14.69 and 1.81 kΩ cm^2 were achieved for Sn, $Sn_{77}Sb_{23}$, and $Sn_{37}Sb_{63}$, respectively. The EIS results suggested that adding Sb^{3+} improves corrosion resistance for SnSb samples with higher Sn content. For $Sn_{77}Sb_{23}$, the charge transfer resistance was 10.5 kΩ cm^2, for Sn and $Sn_{37}Sb_{63}$ 1.15 and 1.46 kΩ cm^2, respectively.

Keywords: $Sn_xSb_{(1-x)}$ coatings; electrodeposition; deep eutectic solvent; corrosion.

INTRODUCTION

Currently, tin (Sn), antimony (Sb) and $Sn_xSb_{(1-x)}$ alloys are promising materials for a variety of applications. These include their use as alloys for welding,[1,2] semiconductors,[3] thermoelectrics,[4] anode materials for metal-ion batteries,[3] anticorrosive coatings[5] and as electrocatalysts for electrochemical reduction of CO_2.[6] The electrodeposition technique, one of the several methods for preparing these coatings, is particularly attractive for industrial practice. It offers a low cost, easy handling, the ability to control the thickness of the electrodeposited coating, and the capacity to obtain electrodeposited layers on metallic substrates of different geometries and shapes. Most importantly, the electrodeposits have excellent adherence to the substrate.[6-11]

However, Sn and Sb have several problems with using water as a solvent or electrolyte for electroplating baths since there is a known hydrolysis in a neutral solution that Sn^{2+} undergoes:[12-14]

$$Sn^{2+}_{(aq)} + H_2O_{(l)} \rightarrow SnO_{(s)} + 2H^+_{(aq)} \qquad (1)$$

This reaction leads to a formation of SnO, which is unstable in an aqueous solution and brings other hydrolysis reactions:

$$SnO_{(s)} + H_2O_{(l)} \rightarrow SnO_{2(s)} + 2H^+_{(aq)} + 2e^- \qquad (2)$$

Also, Sb^{3+}cations can present problems with solvating in water once their solubility can be improved only by using strong acidic solutions:

$$Sb^{3+}_{(aq)} + H_2O_{(l)} \rightarrow SbO^+_{(aq)} + 2H^+_{(aq)} \qquad (3)$$

In this context, deep eutectic solvents (DES) offer a promising alternative for using as supporting electrolytes. Unlike traditional aqueous solutions, many chemical reactions that typically occur in water do not take place in DES. Since DES often contains only a small percentage of water, the hydrolysis reactions involving Sn and Sb mentioned earlier are less likely to occur. Also, the solubility of those compounds is very high in those solvents as the DES polarity can be tuned by choosing the appropriate components to achieve a polar or apolar behavior. In this context, known insoluble salts, such as $SnCl_2$ or $SbCl_3$, are highly soluble and

can be used as a solvent and supporting electrolyte without adding any chemical in the solvent solution. At the same time, the viscosity of the DES can be a problem for this property.

There is increasing interest in developing ambiently more sustainable processes, which means searching for new processes and technologies that mitigate the environmental impacts of the traditional industrial processes. Since the beginning of the first decade of the current century, DES have been investigated as an environmentally friendly alternative to water plating solutions for the electrodeposition of transition metals and their metallic alloys because they are stable, widely available, relatively inexpensive, biodegradable, non-toxic, the metallic salts are soluble, chemically stable in DES[15] and, therefore, electrodeposited metallic layers can be obtained from these solvents without the addition of complexing agents.

Therefore, the interest in the electrodeposition of metals and alloys from DES is rising, as demonstrated in the literature review papers related to this subject, which have already been published in the literature.[16-18] Abbott et al.[18] have used pilot projects for electroplating Ni, Fe and Zn to show that plating solutions based on DES have real potential for application in industrial practice.

Considering the deposition of Sn coatings, Brandão et al.[19] used oxidized multi-walled carbon nanotubes (ox-MWCNT), pristine multi-walled carbon nanotubes (P-MWCNT) and reduced graphene oxide (rGO) over a metallic matrix using a glassy carbon electrode (GC) for comparison. The linear voltammograms showed a reduction peak around 0.6 V vs Ag. The chronoamperometric analysis showed a 3D instantaneous process with diffusion-controlled growth. The Sn coating presented a topography by AFM showing round particles with different roughness in the function of the carbon electrode: the GC along ox-MWCNT presented higher values of roughness in comparison to P-MWCNT and rGO electrodes.

Considering the electrodeposition of Sn alloys, Gao et al.[20] studied the electrodeposition of SnBi alloy coatings using ethaline with boric acid at 90 ºC over a Cu electrode. The morphology of the alloy varies with the applied potential from a compact layer with small grain sizes to an unevenly distributed large grain, which shows the effect of the potential on the Sn-Bi alloy morphology.

Anicai et al.[21] presented SnIn electrodeposition using reline, whose coating had 10-65 % wt. of In. The authors present that the In content in the electrodeposited layer is inversely proportional to the applied current density. The morphology showed irregular particles covering the substrate under direct electrodeposition conditions at 3 mA cm^{-2}. Also, the SnIn electrodeposits can be used as an anti-corrosion barrier by the potentiodynamic polarization and impedance spectroscopy results in 0.5 mol L^{-1} NaCl. Also, the authors performed a

thermogravimetric analysis that showed that the electrodeposited coating had a melting point of 400.7 K and 391.8 K, which justifies the SnIn use as a lead-free welding solder.

A few reports in the literature related to SnSb alloys were obtained from DES. Su et al.[22] successfully electrochemically prepared submicrometric SnSb alloy powders on a titanium substrate in DES medium formed by choline chloride-ethylene glycol (ChCl-EG, 1:2 molar ratio) containing 0.2 mol dm^{-3} $SbCl_3$ and 0.2 mol dm^{-3} $SnCl_2$ at 343 K, showing that the applied electrodeposition potential had a significant effect on the alloy composition, but little influence on the morphology. Ma and Prieto[23] reported that the electrodeposition of pure phase SnSb as alloy-type anode material exhibits high stability for sodium-ion batteries. These authors electrodeposited SnSb thins films from ethylene (1:2 by weight ChCl:EG), and the electrochemical rests demonstrated that independent of SnSb composition, the electrode retained 95% of its initial capacity after 300 cycles at 0.5 $A \cdot g^{-1}$.

This concern arose from the inadequate disposal of Pb waste arising from the manufacturing process and manufactured products.[24,25] The interest in the welding process of SnSb alloys is due to their good thermal fatigue resistance and high fracture strength properties, as pointed out by Wang et al.[1] Furthermore, these authors investigated the welding reliability of SnSb with different Sb contents on the Cu substrate. Therefore, due to the outstanding properties of SnSb alloys and the concern with the creation of a sustainable electroplating process for these alloys, this work aimed to electrodeposited $Sn_xSb_{(1-x)}$ alloys from a plating solution based on 1ChCl:2EG, without the addition of complexing agents, and to evaluate the effect of Sb content on the corrosion behavior of the $Sn_xSb_{(1-x)}$ electrodeposited coatings.

EXPERIMENTAL

Chemicals and electrolyte preparation

All chemicals in this study were used as received without any further purification. The eutectic mixture was prepared by mixing choline chloride (ChCl, Sigma-Aldrich®, ≥99%) and ethylene glycol (EG, Sigma-Aldrich®, ≥99.8%) in a molar ratio 1:2 (1ChCl:2EG) at 353 K until the formation of a colorless liquid. Next, salts anhydrous salts of tin (II) chloride and antimony (III) chloride ($SnCl_2$ and $SbCl_3$, Sigma-Aldrich®, ≥99%) were added to 1ChCl:2EG to form the plating solutions. The compositions of all plating solutions are listed in Table 1.

Table 2. Chemical compositions of the plating solutions prepared by the addition of $SnCl_2$ and $SbCl_3$ to 1ChCl:2EG solvent.

Bath	Electrolyte composition	
	$[Sn^{2+}]$ / 10^{-3} mol dm^{-3}	$[Sb^{3+}]$ / 10^{-3} mol dm^{-3}
I	50	-
II	50	10
III	50	50

Electrochemical measurements

The electrochemical experiments were conducted on a potentiostat/galvanostat model PGSTAT30 (Autolab, Metrohm-Eco Chemie) connected to a computer, using NOVA® software version 2.1.4. To investigate the electrochemical behavior of the Sn^{2+} and Sb^{3+} species in solution and to electrodeposit the $Sn_xSb_{(1-x)}$ coatings, a glass electrochemical cell with a Teflon® lid was used, which was coupled to a thermostatic bath for temperature control under atmospheric conditions. Before each electrochemical measurement, the working electrode was sanded on SiC silicon carbide 600 grit sandpaper, washed with Milli-Q water (18.2 MΩ cm), and dried with airflow. Initially, to characterize the surface of the working electrode in the1ChCl:2EG mixture, cyclic voltammetry was obtained between –0.4 and –1.5 V. Next, to evaluate the electrochemical reduction of Sn^{2+} and Sb^{3+} species (baths I-III), linear sweep voltammetry was performed in the electrochemical range of –0.4 to –1.0 V. All voltammograms were recorded at 10 mV s^{-1} and 353 K. Cu disc (geometric surface area of 0.023 cm^2), a Pt plate (with 1.5 cm^2) and an $Ag_{(s)}/AgCl_{(s)}$ wire immersed in 1ChCl:2EG mixture, were used as the working, auxiliary and reference electrodes, respectively.

Electrodeposition and characterization

All $Sn_xSb_{(1-x)}$ coatings were electrodeposited on Cu discs (geometric area 0.18 cm^2) to characterize the surface morphologies, chemical compositions, and crystalline structures. The electrodeposits were obtained under potentiostatic control at −0.55 V and 353 K, with electric charge control to obtain coatings with a nominal thickness of 2 μm, estimated from Faraday's Equation. The morphologies and chemical compositions of the obtained coatings were analyzed by a scanning electron microscope (FEG-SEM, FEI-Quanta 450) coupled to an

energy-dispersive X-ray spectrometer (EDS, Oxford Instruments INCA X-MAX). The size analysis of the coatings was determined using the ImageJ-Fiji software. Finally, X-ray diffraction (XRD) analyses were carried out using a Bruker Diffractometer, model D8 Advance, equipped with a LynxEye detector. The measurements were made with a Cu tube, operating at 40 kV and 40 mA, a range of 20 to 100 degrees, with a step size of 0.02 degrees and a counting time of 0.2 s/step. The experimental data was treated using PANalytical® X'Pert HighScore Plus® software, and the crystalline phases were indexed using the crystallography PDF-22004 card files from the Inorganic Crystal Structure Database (ICSD).

Electrochemical Corrosion Tests

An electrochemical cell composed of three electrodes was used for corrosion tests. Ag(s)/AgCl(s)/Cl^- (saturated KCl) was used as the reference electrode, a platinum foil of 1 cm^2 was the counter electrode, and the Cu recovered with the $Sn_xSb_{(1-x)}$ coatings was the working electrode. Before each experiment, the open circuit potential (E_{ocp}) was recorded as a function of time for 1 h. The potentiodynamic polarization curves were obtained in 0.1 mol dm^{-3} NaCl at 298 K and 0.5 mV s^{-1} and between −0.25 V and +1.00 V around the E_{ocp}. All the experiments were performed in duplicate. After sample preparation, their morphology was evaluated after 24 h and 48 h immersion in a 0.1 mol dm^{-3} NaCl solution. The effect of the potential applied in a 0.1 mol dm^{-3} NaCl medium, −0.1 V and 0.2 V for 1 h was also evaluated. A copper disc with a geometric area of 0.28 cm^2 was used for these experiments. The electrochemical impedance spectroscopy results were obtained in 0.1 mol dm^{-3} NaCl at 298 K, applying 0 V to the E_{ocp} in the frequency range of 20 kHz to 6 mHz with a sinusoidal amplitude of 12 mV. Twelve points were collected by frequency decade. The validation of results considered Lissajous method.

RESULTS AND DISCUSSION

Electrochemical analyses

The insert in Figure 1 shows the cyclic voltammetry, at 353 K, obtained from 1ChCl:2EG on a copper surface in the potential range of –0.4 V to –1.5 V. In this potential range, there is an increase in the cathodic current density at potential values from –1.2 V. This process is associated with the reduction of ethylene glycol hydroxyl groups, choline chloride cationic ions and traces of water.[26]

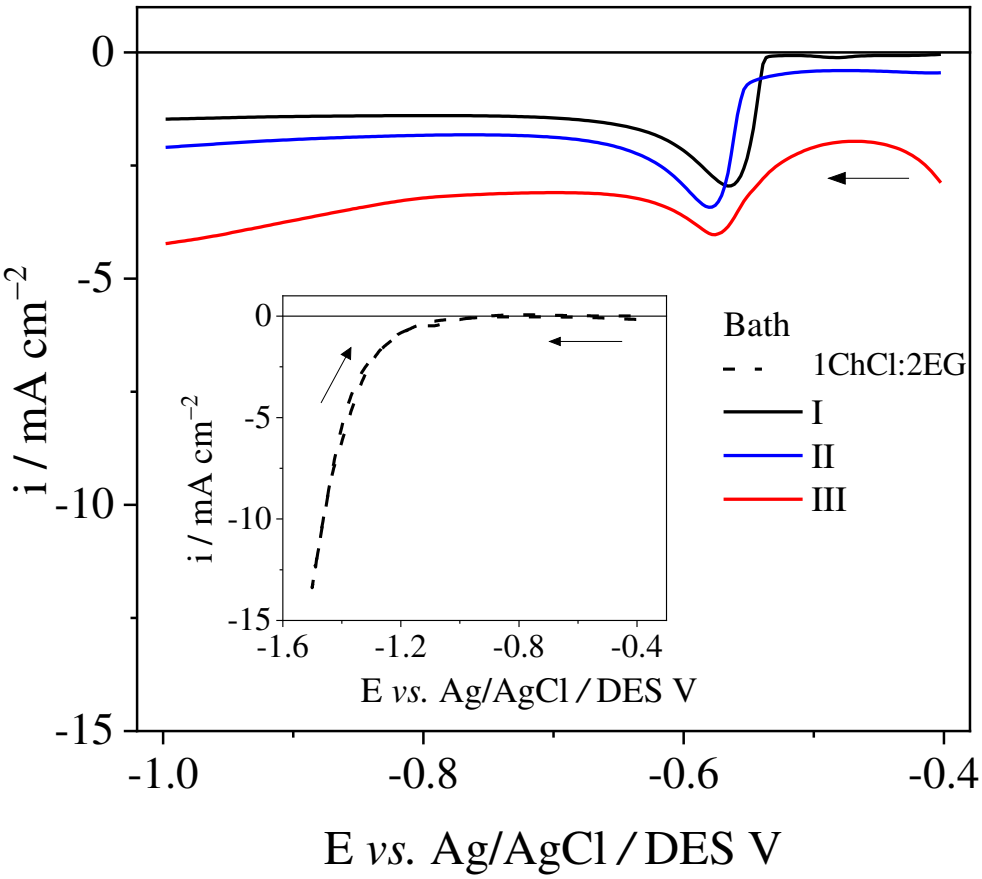

Figure 4. Linear sweep voltammetry of the copper electrode in baths I, II and III at 353 K and 10 mV s^{-1}. The inset shows a linear sweep voltammetry obtained for a copper electrode in 1ChCl:2EG mixture at 353 K and 10 mV s^{-1}.

The electrochemical behavior of Sn^{2+} and Sb^{3+} species was investigated by linear sweep voltammetry using a Cu electrode immersed in baths I-III, applying a potential range between –0.4 and –1.0 V at 10 mV s^{-1} and 353 K. The recorded voltammograms are shown in Figure 1. For bath I (black line), a single well-defined cathodic peak can be observed at –0.56 V, which is attributed to the electrochemical reduction of Sn^{2+} to metallic Sn. A similar voltammetric profile was reported in a previous investigation for the electrodeposition of Sn.[27-29]

Since the Sb content increases in baths II and III (blue and red lines), the voltammograms change regarding cathodic peak potential and total electrochemical charge. A similar system was used for Sb electrodeposition in the literature, but a Pt disc was used as the working electrode. In this context, the peak potential of Sb^{3+} reduction at 298 K was located before –0.4 V since this electrode presents more electrochemical stability than the Cu substrate.

Once undesired electrochemical reactions occur before –0.4 V in DES, the voltammogram for bath III (red line) presents a so-called "semi-peak" between –0.4 and –0.5 V due to the diffusion process of Sb^{3+} reduction. The subsequent peak around –0.58 V is related to the Sn^{2+} reduction, which was slightly shifted towards more negative potentials than pure Sn^{2+} bath I (black line). In bath II (blue line), having less Sb^{3+} than bath III, the cathodic peak seen in bath III does not appear, having the Sn^{2+} reduction process at –0.58 V. Although the hypothesis of co-deposition of the Sn^{2+} and Sb^{3+} was reported in the literature. But, as shown in Figure 1, the increase of Sb^{3+} concentration does not change the cathodic peak potential of Sb^{3+} process.

Morphology, composition, and structural results

The SEM images shown in Figure 2 presented an evolution of the structure from a cuboid-like in pure Sn to a pentagonal-like structure in $Sn_{37}Sb_{63}$. In Figure 2I, it is possible to see the body-centered tetragonal, once the cuboid structure is elongated in metallic islets. When Sb is added, there is a transition in the structure, as shown in Figure 2II, in which those islets do not appear due to the rhombohedral structure of Sb, which modulates the alloy grain size. Still, in this image, they are tiny alloy grains with pentagonal and hexagonal shapes, which could be related to the atomic position of the elements in the alloy that mixes both cuboid (from Sn) and rhombohedral (from Sb) structures. This observation is clearer in Figure 2III, which shows many pentagonal-like structures in the SnSb and other regular shapes, such as trigonal and cuboid. With increased Sb content in the coatings, the rhombohedra structure is predominant, which causes those variations in the alloy grains. Compared with the pure Sn image (Figure 2I), Figures 2II and 2III exhibit a regular and compact layer, which is not seen in the pure Sn image. The Sn islets are deposited over an Sn layer; the electrodeposited Sn layer can be attributed to the voltammetric results in Figure 1, which shows a small peak at circa −0.47 V. Although the system is similar having Sn^{2+} in ethaline using a copper electrode, the $Sn_{(ads)} \rightarrow Sn_{(abs)}$ step was not observed within the potential window of the copper electrode. $SnSO_4$ rather than $SnCl_2$ probably creates an extra step with the so-called "absorption" of the deposited Sn layer. Therefore, this Sn layer before the bulk Sn deposition was observed in both voltametric and SEM experiments.

Figure 2I shows that grain clusters are present in pure Sn deposits. When Sb^{3+} is added to the electrolytic solution (Figure 2II), a reduction in the average size to 1.05 μm was observed, in addition to a non-uniform overlayer.[30] In Figure 2III, obtained from an equimolar

solution of Sn^{2+} and Sb^{3+}, grains with distinct shapes (circular, pentagonal, and hexagonal) were observed, covering the entire surface. This organization of the morphology was related to the reduction in the average particle size (0.49 μm), approximately 10 times smaller than the coating containing only Sn (Figure 2I).

Azpeitia et al.[31] found a similar morphology for Sn electrodeposition in 1ChCl:2U on a copper substrate at 343 K, applying a potential of −0.75 V. The atom percentages of Sn and Sb in each electrodeposited coating are displayed in Table 2. From this table, it can be observed that increasing the concentration of Sb^{3+} species in the plating solution composition led to an increase in the Sb content in the coating and that the ratio between the Sb and Sn content in the coatings is higher than this ratio in the plating solution, indicating that under the used operational conditions, the electrodeposition of $Sn_xSb_{(1-x)}$ is classified as normal, based on the comparative analysis of the ration Sn/Sb in the bath and Sn/Sb in the electrodeposited layer.

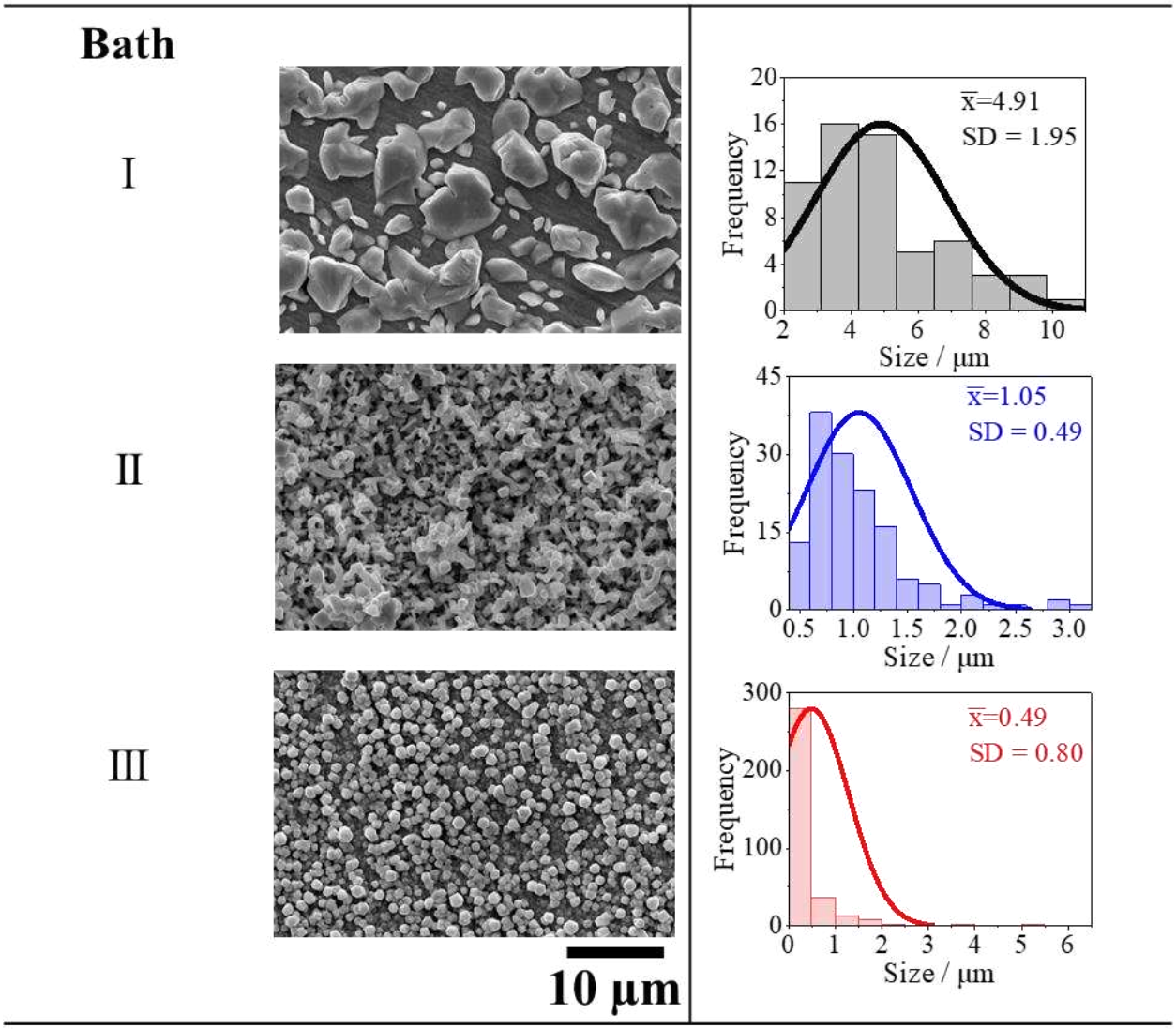

Figure 5. SEM micrographs electrodeposit of Sn (I), $Sn_{77}Sb_{23}$ (II) and $Sn_{37}Sb_{63}$ (III) onto Cu electrode –0.55 V at 353 K. Histograms of the particle size of coatings.

Table 3. Chemical composition of electrodeposited coatings from EDS results and samples labelling.

Bath	Film composition by EDS		Film
	Sn / at. %	Sb / at. %	
I	100	-	Sn
II	77	23	$Sn_{77}Sb_{23}$
III	37	63	$Sn_{37}Sb_{63}$

X-ray diffraction analyses were performed to investigate the effect of electrolytic bath composition on the crystal structure of $Sn_xSb_{(1-x)}$ coatings. Figure 3 shows the XRD patterns for the electrodeposits of Sn, $Sn_{77}Sb_{23}$ and $Sn_{37}Sb_{63}$ obtained on the Cu surface from baths I, II and III, applying a potential of –0.55 V at 353 K. In all diffractograms in Figure 3, peaks corresponding to the Cu substrate were indexed at $2\theta = 43.2°$, 50.4°, 74.0° and 89.9° with a crystal structure cubic (space group Fm-3m, #225, ICDD #00-003-1005). For the diffractograms in Figure 3a-b, a pure Sn phase was indexed at $2\theta = 30.6°$, 31.9°, 43.8°, 44.8°, 55.3°, 62.5°, 63.7°, 64.5°, 73.1° and 79.4°, referring to planes (200), (101), (220), (211), (301), (112), (400), (321), (411) and (312), respectively, with a tetragonal crystal system (space group I41/amd, #141, ICDD #03-065-0296). In addition, a diffraction peak of the intermetallic phase Cu_6Sn_5 with a monoclinic crystal structure (space group C2/c, #15, ICDD #00-045-1488) was indexed for the diffractograms of Figure 3a-b. The pure Sn and intermetallic Cu_6Sn_5 phases were observed, as Zhao et al. [32] reported.

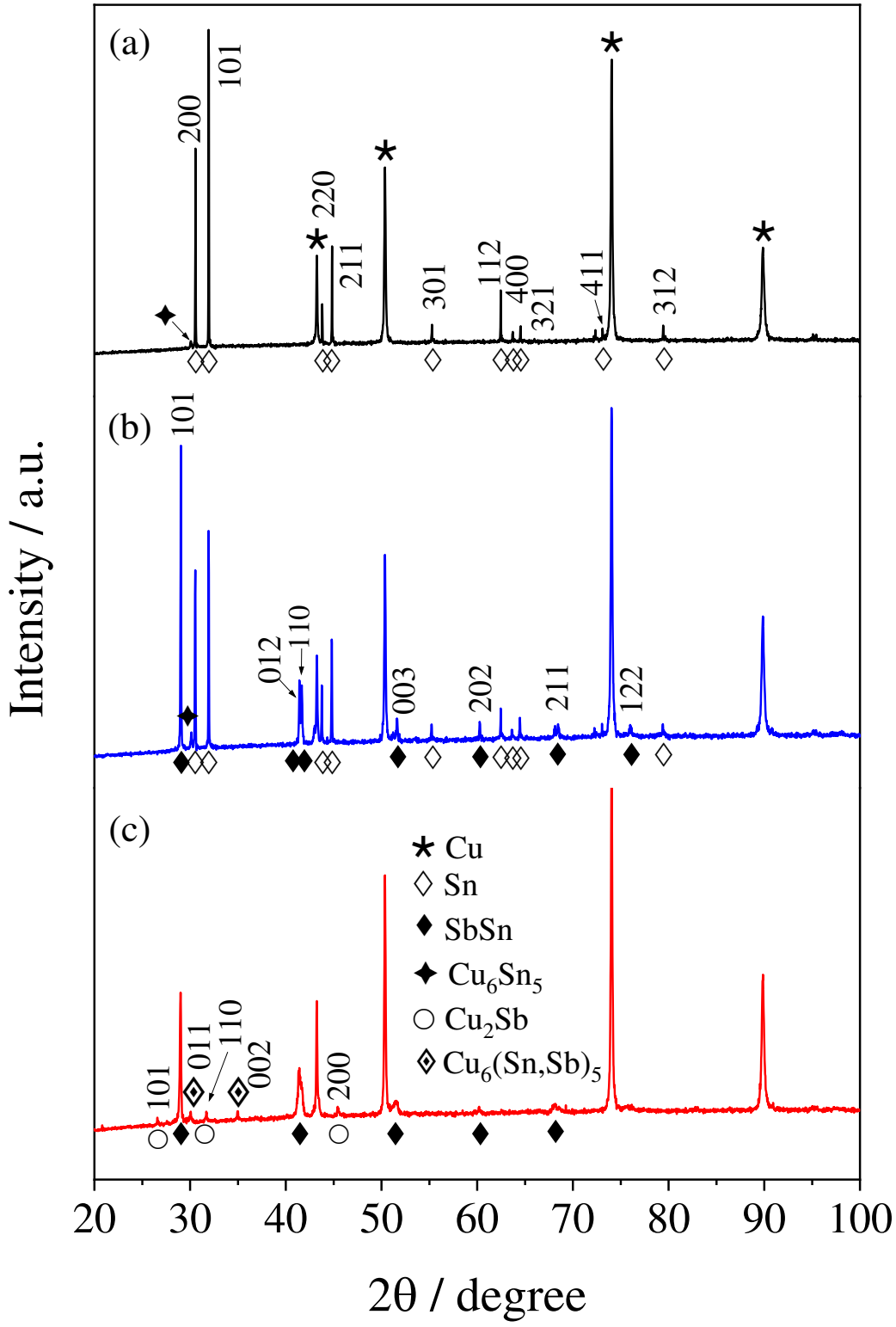

Figure 6. Diffraction patterns electrodeposit of Sn (a), $Sn_{77}Sb_{23}$ (b) and $Sn_{37}Sb_{63}$ (c) onto Cu electrode –0.55 V at 353 K.

Additionally, for diffractograms of Figure 3b-c, it was observed that the presence of Sb^{3+} in the electrolytic baths II and III favored the formation of the SnSb alloy, evidenced by the pure phase SbSn, with a rhombohedral crystal system (space group R-3m, #166, ICDD #00-033-0118).[33] Finally, for the diffractogram of Figure 3c, phases referring to the intermetallic Cu_2Sb and $Cu_6(Sn, Sb)_5$ were indexed, with tetragonal crystal structure (space group P4/nmm, #129, ICDD #01-087-1176) and hexagonal crystal system (space group P63/mmc E, #194, ICDD #00-49-1055), for Cu_2Sb and $Cu_6(Sn, Sb)_5$, respectively. The formation of these CuSn and CuSb intermetallic phases is attributed to the metallic bonding between the Cu atom on the surface of the Cu electrode and the first SnSb electrodeposited layer on the Cu surface. Considering the different phases and morphologies obtained in the coatings, a test was carried out to evaluate the applicability of the coatings for corrosion.

Electrochemical corrosion tests

Potentiodynamic Polarization (PP)

The potentiodynamic polarization curves obtained for the $Sn_xSb_{(1-x)}$ coatings in 0.1 mol dm^{-3} NaCl are shown in Figure 4. The results suggest an anodic behaviour of the $Sn_xSb_{(1-x)}$ alloys, meaning that deposits are less noble than pure Sn deposits. Those differences can be explained by the coating morphology: the pure Sn has a layer combined with a bulk layer of the metal, whereas the SnSb alloy presented no apparent layer. When the Sb content increases, the alloy grain decreases, and the electroactive area increases. The corrosion resistance of the investigated samples was evaluated by the polarization resistance (R_p) derived from the PP curves since the corrosion rate of a sample decreases with the increase of the R_p values. The Rp values were calculated from the fitted slope of the PP curves in the region of corrosion potential (E_{corr}) ±10 mV, as shown in Figure S1. The obtained Rp values and E_{corr} are presented in Table 3. The E_{corr} values for Sn and Sn77Sb23 were statistically similar, considering the standard deviation at a 95% confidence level. When adding Sb to the coating, a three-fold increase in the obtained R_p value was observed compared to the coating containing only Sn. Initially, it can be noted that the sample with higher Sb content presents a less negative corrosion potential than those with higher Sn content. The cathodic branches of the PP curves are related to the oxygen reduction reaction (ORR), which is the cathodic reaction of the corrosion process in a neutral medium. For the anodic branches, it can be noted that the PP anodic curves obtained for the Sn and $Sn_{77}Sb_{23}$ are similar and characterized by three potential regions. The first region is related

to the current increase with applied potential until it reaches a maximum current, attributed to the active dissolution of both electrodeposited coatings. The second region is evidenced by the current plateaus, which are associated with the deposition of SnO or SnO_2 on the coating surfaces,[34-36] acting as a physical barrier against the corrosion of both coatings. The third region presents an increase of the current with the applied potential due to the breakdown of oxide film, which allows the active dissolution corrosion of Sn and $Sn_{77}Sb_{23}$ coatings. These results are in close agreement with those reported by Dias et al.[34] which investigated the corrosion behavior of SnSb solder alloys varying the Sb content between 2 and 10 wt%. Finally, the anodic curve achieved for the sample richer in Sb ($Sn_{23}Sb_{67}$) shows the corrosion in the working electrolyte without the formation of oxides on its surface. Figure 5 shows the SEM images and diffractograms for the Sn, $Sn_{23}Sb_{77}$, and $Sn_{37}Sb_{63}$ coatings after 24 and 48 h of immersion.

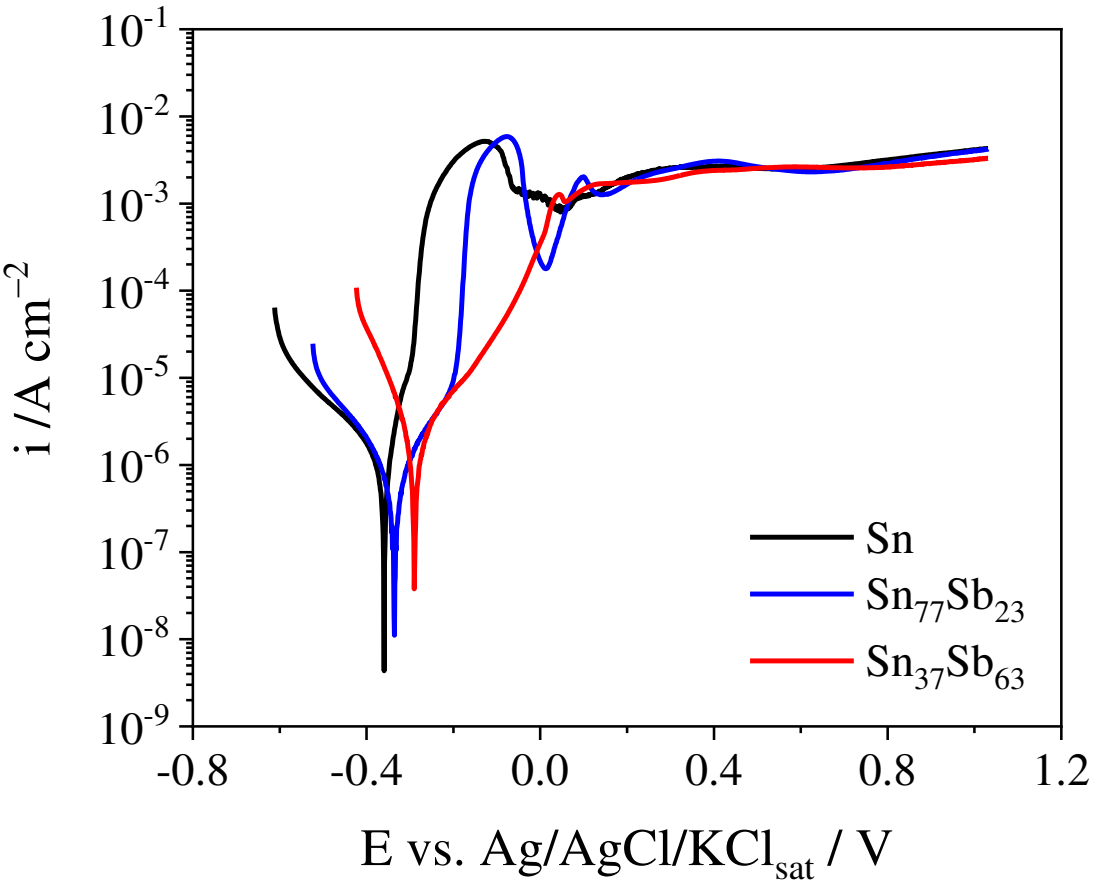

Figure 4. The potentiodynamic polarization curves of different coatings in 0.1 mol dm^{-3} NaCl at 298 K and 0.5 mV s^{-1}.

Table 3. Electrochemical parameters for coatings Sn, $Sn_{77}Sb_{23}$ and $Sn_{37}Sb_{63}$ in 0.1 mol dm^{-3} NaCl obtained for Figure 4.

Samples	$-E_{corr}$ / mV	R_p / kΩ cm^2
Sn	347 ± 55	4597 ± 235
$Sn_{77}Sb_{23}$	348 ± 41	14692 ± 817
$Sn_{37}Sb_{63}$	299 ± 70	1806 ± 306

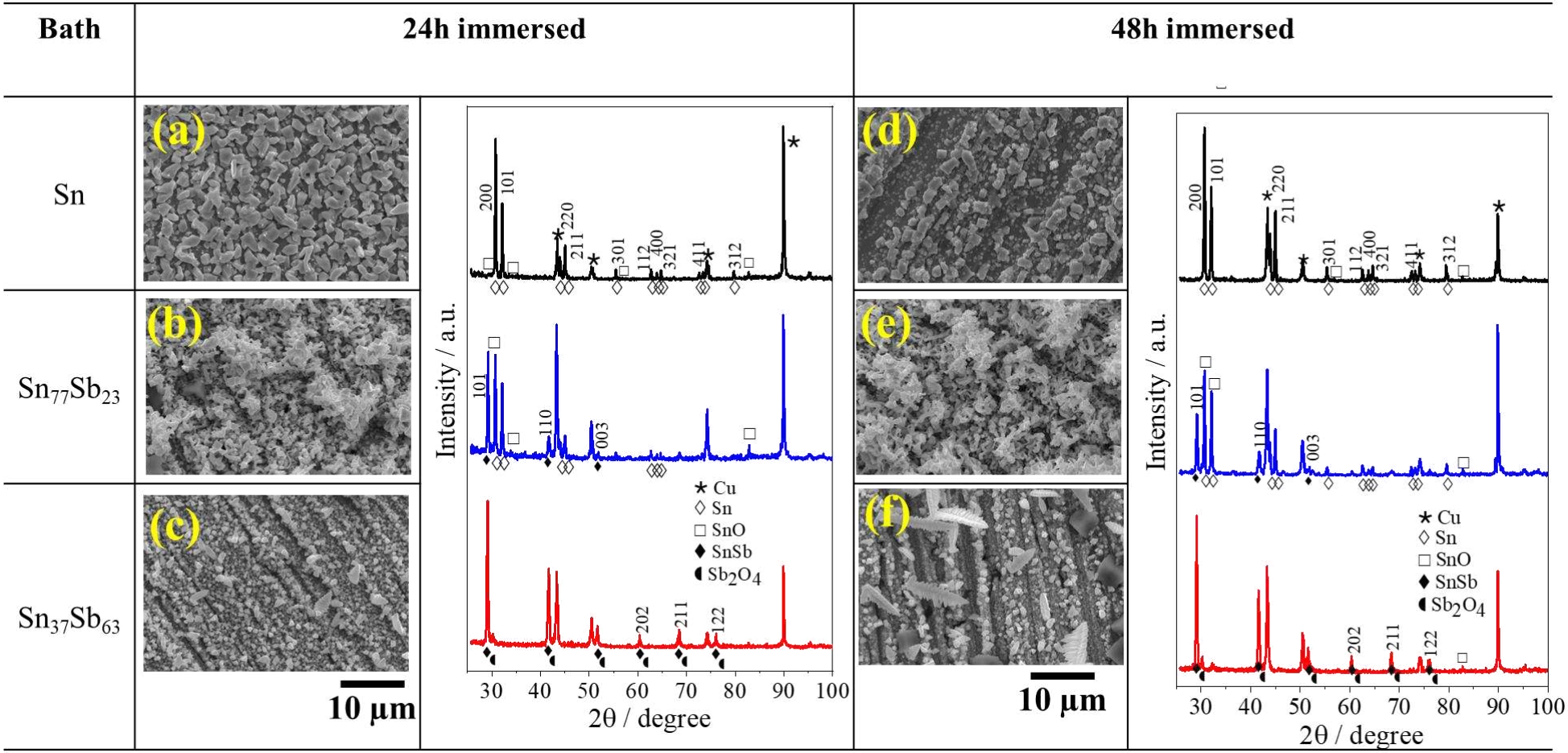

Figure 5. SEM images and DRX results for Sn (a-d), $Sn_{77}Sb_{23}$ (b-e) and $Sn_{37}Sb_{63}$ (c-f) at different immersion times (24 h and 48 h) in NaCl in 0.1 mol dm^{-3} at 298 K.

Analyzing the coatings obtained for Sn (a and d), it was observed that when immersed in the NaCl solution, there was a reduction in the number of grains observed at 48 h, compared to 24 h, where it was possible to observe vacancies in the coating due to exposure. For the $Sn_{77}Sb_{23}$ coatings (b and e), it was observed that the immersion time did not alter the morphology. The $Sn_{37}Sb_{63}$ coatings (c and f) presented a dendritic morphology resembling pine trees[30,37,38] with size of approximately 0.022 μm for 24 h and 0.19 μm for 48 h, demonstrated in Figure S2. The analysis of XRD data from the samples immersed in 0.1 mol dm^{-3} NaCl solution for 24 h allowed for the identification of five distinct crystalline phases: Cu, Sn, SnO, SbSn and Sb_2O_4. Characteristic peaks of the SnSb phase were observed in both the $Sn_{23}Sb_{77}$ and $Sn_{37}Sb_{63}$ materials for 24 h of immersion. Identifiable peaks related to the SnO phase were observed in $Sn_{23}Sb_{77}$, and identifiable peaks related to Sb_2O_4 phases were found in the $Sn_{37}Sb_{63}$ material. Considering 48 h of immersion, the analysis of XRD data allowed for the identification of four distinct crystalline phases: Cu, CuSn, SnO_2 and SnSb. Characteristic peaks of the SnSb phase were observed in both $Sn_{23}Sb_{77}$ and $Sn_{37}Sb_{63}$ materials for 48 h of immersion. Identifiable peaks related to the SnO phase were observed in both samples mentioned, and identifiable peaks related to the Sb_2O_4 phases were found only in the $Sn_{37}Sb_{63}$ material. Analyzing the SnSb polarization curves and the XRD analysis of the samples after immersion (Figures 4 and 5) showed that the formation of Sn and Sb oxides occurred in all coatings. For Sn and $Sn_{77}Sb_{23}$, the first level appeared due to the high Sn content. For the $Sn_{27}Sb_{63}$ coating, the first level referring to Sn did not appear because all the Sn present in the coating was used to combine with Sb. In this last league, Sb is in excess (63%).

For the coatings, Figure 4 shows at potential with values close to −0.1 V, a maximum current density, and stability in the current density values at 0.2 V. Polarization tests were conducted by applying the mentioned potential for 1 h to evaluate the influence of the potential applied to the Sn and SnSb coatings. Figure 6 shows the SEM images and diffractograms for the Sn, $Sn_{23}Sb_{77}$, and $Sn_{37}Sb_{63}$ coatings, obtained by polarizing the electrode for 1 h, at −0.1 and 0.2 V.

At −0.1 V, Figure 6 (a-c), the analysis of XRD data allowed for identifying five distinct crystalline phases: Cu, CuSn, SnO, SnO_2 and SnSb. Characteristic peaks of the SnSb phase were observed in the $Sn_{23}Sb_{77}$ and $Sn_{37}Sb_{63}$ coatings at −0.1 V, confirming the formation of the SnSb alloy. Identifiable peaks referring to the SnO phases were observed in the two samples mentioned. Figure 6 (d-f) shows the SEM images and diffractograms for the Sn, $Sn_{23}Sb_{77}$, and $Sn_{37}Sb_{63}$ coatings obtained by polarizing the coating at 0.2 V for 1 h.

The analysis of XRD data allowed for identifying eight distinct crystalline phases: Cu, Cu_2O, Cu_3Sn, SnO, SbSn, SnSb, Sb_2O_3 and SbO_2. Characteristic peaks of the SnSb phase were observed in the $Sn_{23}Sb_{77}$ and $Sn_{37}Sb_{63}$ coatings. Identifiable peaks related to the SbO_2 and Sb_2O_3

phases were also detected. For the coatings containing only Sn Figure 6 (a and d), it was observed that the negative potential ended up removing the grains observed in Figure 5. In contrast, at 0.2 V, a morphology like that obtained in Figure 5 was observed.

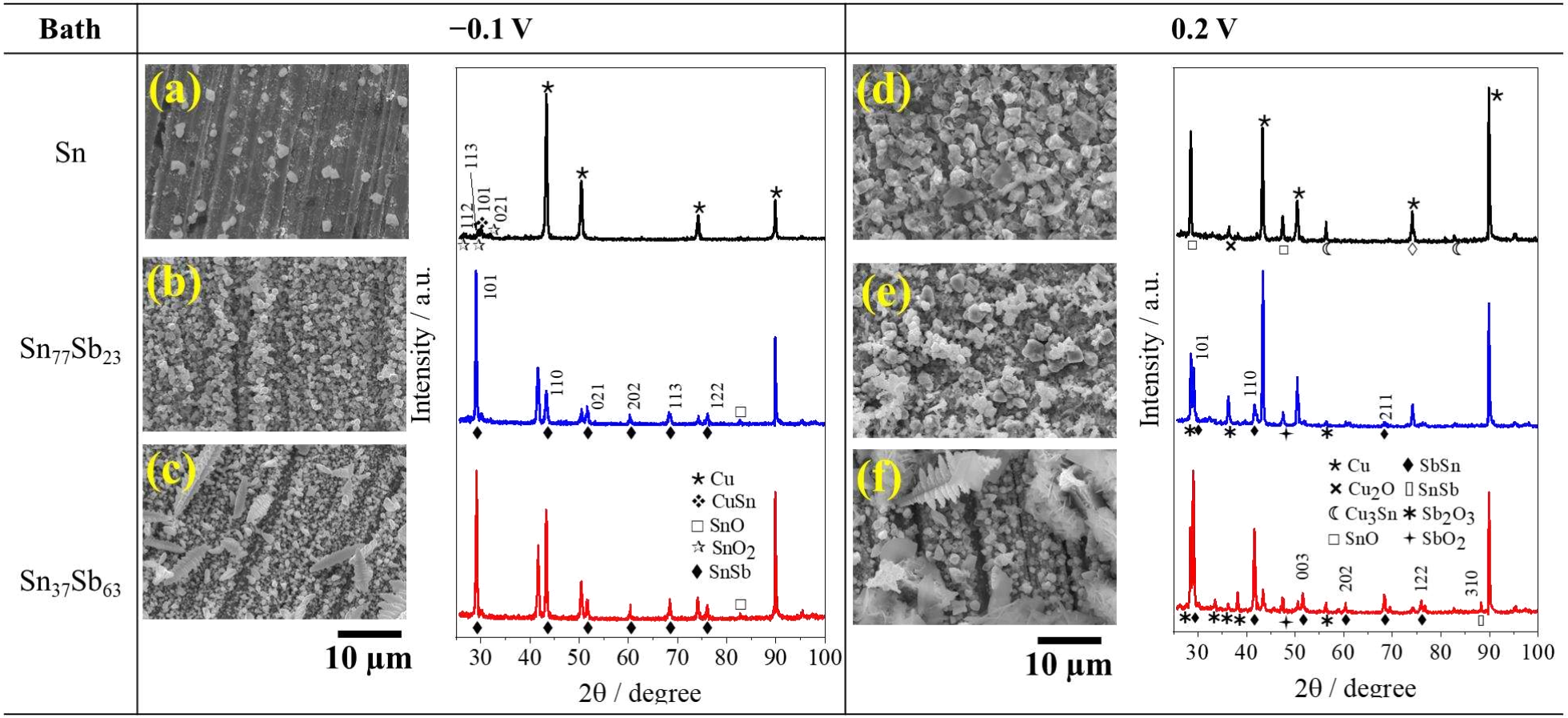

Figure 6. SEM images and DRX results for Sn (a-d), $Sn_{77}Sb_{23}$ (b-e) and $Sn_{37}Sb_{63}$ (c-f) after 1 h at polarization on –0,1 V (a-c) and 0,2 V (d-f) on 0.1 mol dm^{-3} NaCl at 298 K.

Electrochemical Impedance Spectroscopy (EIS)

EIS experimental data were collected for Sn, $Sn_{37}Sb_{63}$, and $Sn_{77}Sb_{23}$ coatings at 298 K in open circuit potential after 1 h of immersion in 0.1 mol dm^{-3} NaCl. Figure 7 presents the Nyquist diagrams obtained.

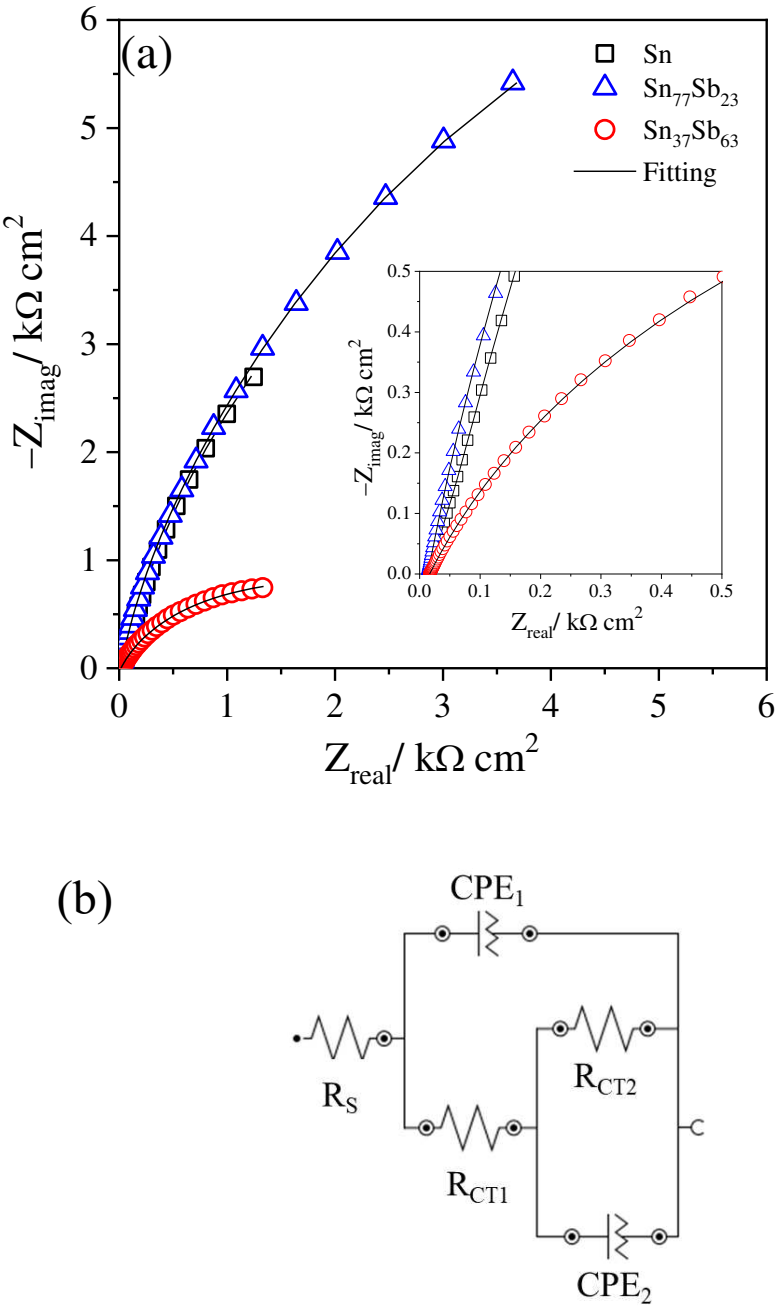

Figure 7. (a)Nyquist diagrams of coatings in the 0.1 mol dm^{-3} NaCl at 298 K. Empty symbols indicate experimental results and filled symbols indicate the fitting values using the EEC model. (b) shows an example of better visualization at high frequencies. EEC model used to explain and fit the experimental EIS results.

The EIS diagrams were obtained at open circuit potential after 1 h of immersion of the samples in 1 mol L^{-1} NaCl. The potentials of −0.37 V, −0.30 V, and −0.24 V, determined by OCP after 1 h, were applied to Sn, $Sn_{77}Sb_{23}$, and $Sn_{37}Sb_{63}$, respectively, during the EIS experiment. The evolution of open circuit potential values with immersion time is shown in Figure S3.

Since the highest corrosion resistance is associated with the largest capacitive arc, the results indicate a greater susceptibility to corrosion for the coating with a higher Sb content ($Sn_{37}Sb_{63}$) and a greater tendency towards corrosion resistance for the binary coating with a higher Sn content ($Sn_{77}Sb_{23}$). A similar trend was observed in the study of potentiodynamic polarization curves.

$Sn_{77}Sb_{23}$ coating was analyzed during 24 h of immersion in 0.1 mol dm^{-3} NaCl. The data corresponding to immersion times of 1, 2, 4, and 24 h are presented in Figure 8. Nyquist diagram profile showed no change from 4 h to 24 h. These results indicate an increase in susceptibility to corrosion of the coating with an increase in immersion time.

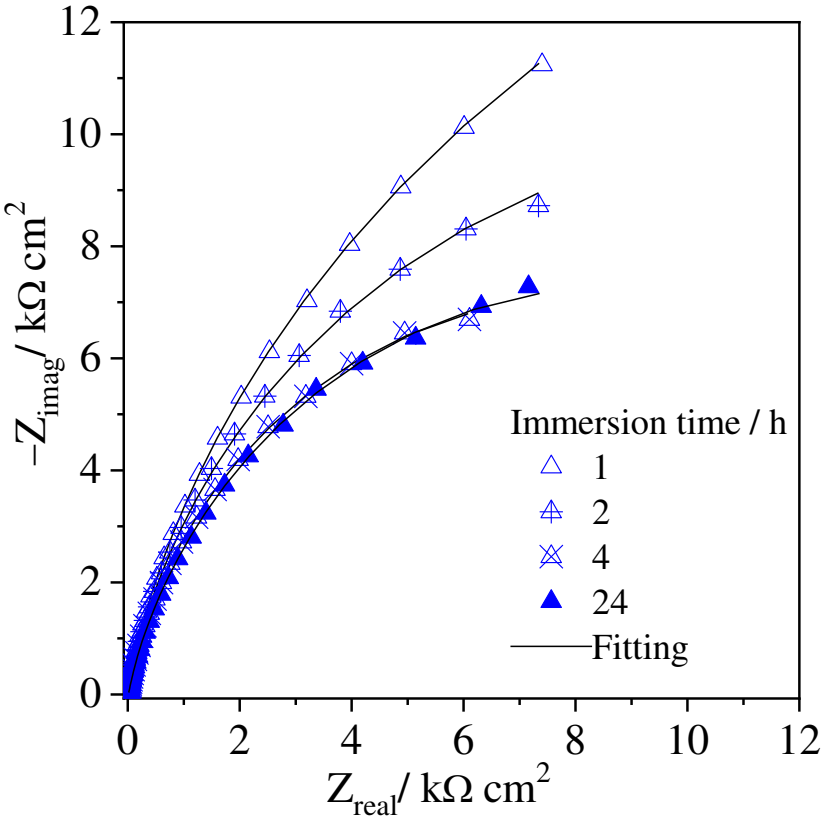

Figure 8. Nyquist diagrams of $Sn_{77}Sb_{23}$ in the 0.1 mol dm^{-3} NaCl at 298 K in different immersion times. Empty symbols indicate experimental results and filled symbols indicate the fitting values using the EEC model.

EIS data (Figure S4) reveal the presence of two-time constants regardless of the analyzed coating. Analysis of the Nyquist diagrams shows capacitive time constants with elongated characteristics, indicating the overlap of two-time constants. A first-time constant is observed in the high to medium-frequency region, and the second-time constant is characterized in the low-frequency region (below 0.1 Hz). A similar result was reported by Dias et al.[34]

The X-ray diffraction (XRD) obtained after experiments in 0.1 mol dm–3 NaCl reveal the formation of oxides as corrosion products. This result allows for the association of the two-time constants with the oxides/electrolyte interface and the coating/oxides interface. The corrosion product layer's resistance and capacitance are linked to the time constants at a high frequency region. The capacitance and resistance of the electrical double layer between the interface of corrosion products and coating are linked to the time constants at a low frequency region.

Taking into consideration the coating surface characteristics and the formation of oxides, the proposed model (Insert of Figure. 7b) comprises the solution resistance, R_S, in series with two parallel elements: charge-transfer resistance (R_{CT}) and constant phase element (CPE). The first-time constant (R_{CT1}-CPE_1) couple corresponds to the oxides/electrolyte interface, while the second-time constant (R_{CT2}-CPE_2) couple, characterized in the low-frequency region, is associated with the coating/oxides interface. This configuration aligns with observations from other studies of Sn-based coatings in the literature.[39-41] The CPE is essential as it accounts for the distribution of relaxation times arising from physical, chemical, or geometrical inhomogeneity.[42,43]

Equation (4) describes the CPE impedance (Z_{CPE}), which is characterized by a non-ideal double-layer capacitance.

$$Z_{CPE} = \frac{1}{Y_o(j\omega)^{\alpha}} \qquad (4)$$

Where j is an imaginary number, ω is the angular frequency of sinusoidal perturbation, and Y_o is the capacity parameter that considers the combination of properties related to the surface and electrochemical species and proportional to the electroactive area.[40] The parameter α is the dimensionless non-linearity coefficient that ranges between 0 and 1. A value of 1 corresponds to an ideal capacitor, 0 corresponds to a resistor, and 0.5 can be associated with diffusion phenomena. Additionally, a value of −1, indicating inductive behavior.[44,45]

The quality of the fit was assessed using chi-squared values, which ranged of 10^{-4} to 10^{-5}.Considering fitting criteria such as the "number of model parameters" and "Chi-square values",[39], the NOVA software version 2.1.5 was utilized to develop the electric equivalent circuit (EEC) model and determine the values of its components, resulting in a very good approximation to the experimental data. EEC parameter values obtained by modeling the experimental data of Sn, $Sn_{37}Sb_{63}$, and $Sn_{77}Sb_{23}$ coatings after 1 h of immersion are presented in Table 4. EEC parameter values for the $Sn_{77}Sb_{23}$ coating, analyzed for 24 h of immersion, are presented in Figure 8.

Table 4. Parameters obtained by fitting the experimental result of the EIS on the different coatings using the EEC model.

Coating	R_s	R_{CT1}	Yo_1	α_1	R_{CT2}	Yo_2	α_2
	Ω cm^2	kΩ cm^2	μF s$^{(\alpha-1)}$ cm^2		kΩ cm^2	μF s$^{(\alpha-1)}$ cm^2	
Sn	89	1.15	55.2	0.85	12.5	1.32	0.95
$Sn_{77}Sb_{23}$	76	10.5	538.9	0.88	7.43	422.2	0.85
$Sn_{37}Sb_{63}$	93	1.46	2744.4	0.71	2.7	515.0	0.45

Figure 9 illustrates a decrease in R_{CT2} with increasing immersion time. This trend may be attributed to the release of Sn^{2+} ions into the solution, which reduces the corrosion resistance of the coating. A slight increase in R_{CT1} value accompanies this decline in resistance. The action of the chloride ion results in the dissolution of the coating's passivation film to some extent. Concurrently the passivation film is repaired due to the coating's corrosive processes. This behavior corroborates the values of the first-time constant (R_{CT1}-CPE_1) couple, as they exhibited little variation with immersion time. For SnSb electrodeposited alloys (Figures 2II and 2III), the SEM images reveal that the electrodeposited coating is granular, and it is possible to observe the occurrence of smaller hexagonal and circular grains in the presence of Sb, making the coatings more homogeneous and with a larger surface area.

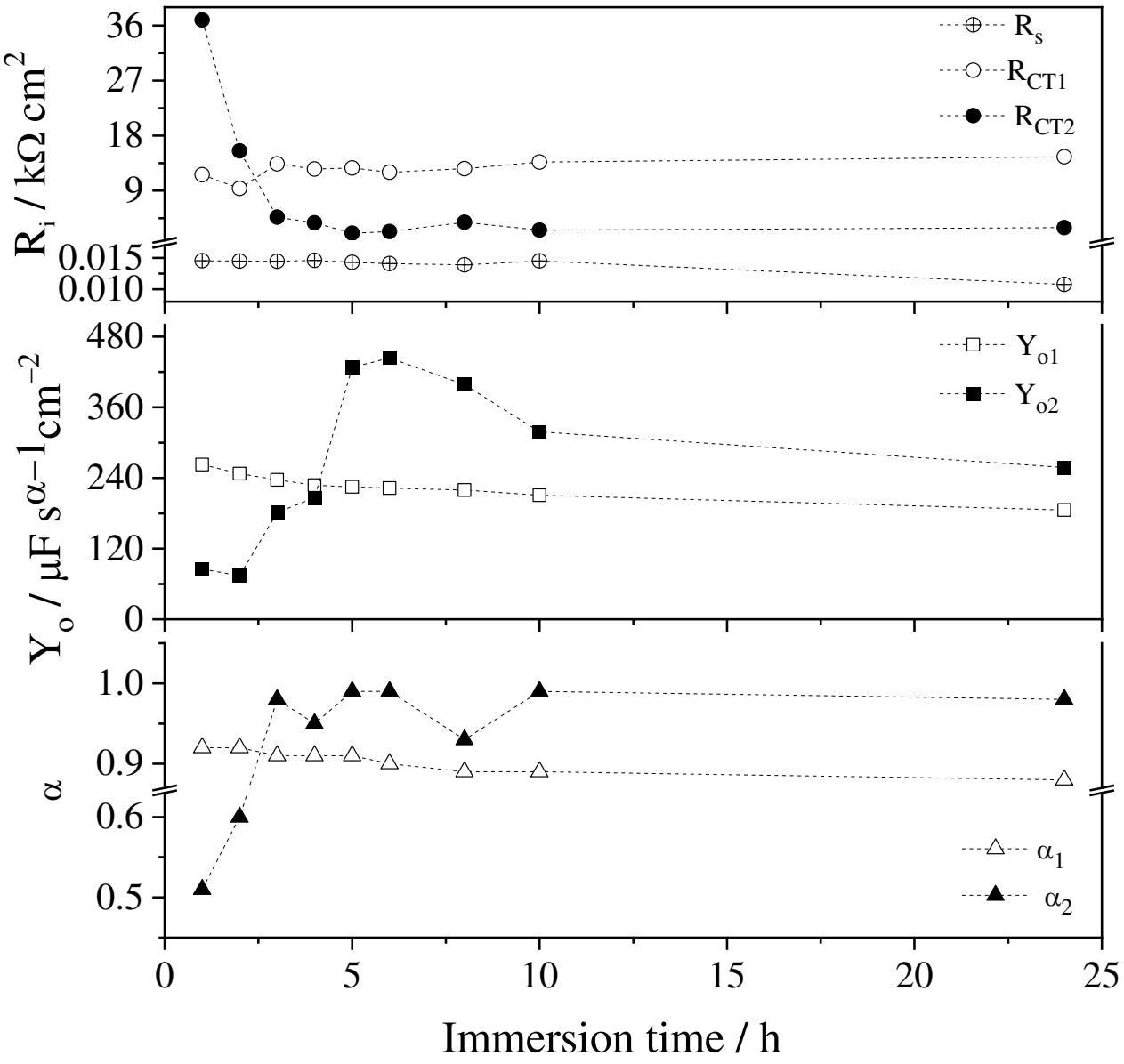

Figure 9. Relationship between parameters obtained from the EIS result of $Sn_{77}Sb_{23}$ in the 0.1 mol dm^{-3} NaCl at 298 K across different immersion times.

This result aligns with the capacity parameter (Y_o) observed in the $Sn_{37}Sb_{63}$ and $Sn_{77}Sb_{23}$ coatings, as they exhibited higher values. The α values obtained for the $Sn_{37}Sb_{63}$ and $Sn_{77}Sb_{23}$ coatings after 1 h of immersion in 0.1 mol dm^{-3} NaCl support diffusion phenomena, with values close to 0.5. The diffusion phenomena observed at low frequencies suggest rapid coating corrosion, likely due to the inadequate formation of an efficient protective film. R_{CT2} values for the Sn and $Sn_{77}Sb_{23}$ coatings were 12.6 kΩ cm^2 and 10.4 kΩ cm^2, respectively, while

the $Sn_{37}Sb_{63}$ coating exhibited the lowest value at 2.7 kΩ cm^2. Consistent with the polarization curves, the results obtained from EIS suggest a correlation between corrosion resistance and the percentage of Sn, indicating an increase in corrosion resistance increases with higher Sn content.

The XRD data reveals a single Sn matrix, with Sb appearing in intermetallic forms such as SnSb dispersed within the Sn matrix. The proportion of intermetallics increases with Sb content, potentially forming multiple galvanic couples that can affect the resulting corrosion resistance.[34,46,47]

The formation of Sn-based oxides and hydroxides has been extensively reviewed in the literature. Kapusta and Hackerman[48] elucidate the pathways leading to the formation of $Sn(OH)_2$ and SnO, corresponding to reactions 5 and 6, respectively. The redox potentials of these half-reactions exhibit proximate values and are contingent upon pH variations.[49]

$$Sn_{(s)} + 2OH^-_{(aq)} \rightleftharpoons Sn(OH)_{2(s)} + 2e^- \qquad (5)$$

$$Sn_{(s)} + 2OH^-_{(aq)} \rightleftharpoons SnO_{(s)} + H_2O_{(l)} + 2e^- \qquad (6)$$

Since $Sn(OH)_2$ can be considered as an H_2O-containing SnO. Dehydration of $Sn(OH)_2$ can indeed produce result in the production of SnO, as indicated by equation 7.[34,39] This transformation occurs specifically when the Sn-based surface is exposed to a dry atmosphere.[50] However, the experimental conditions in the present study do not involve a dry atmosphere. The formation of SnO, validated by the XRD spectrum presented in Figure 5, is attributed to reaction 7.

$$Sn(OH)_{2(s)} \rightarrow SnO_{(s)} + H_2O_{(l)} \qquad (7)$$

The literature suggests the formation of $Sn(OH)_4$ and SnO_2 according to equations 8 and 9, respectively.[34,39-42] However, these compounds were not observed in the XRD spectrum provided in Figure 5. Kapusta and Hackerman[48] indicate that these reactions exhibit slow kinetics, and an increase in the anodic potential may promote the formation of these compounds.

$$SnO_{(s)} + 2OH^-_{(aq)} \rightleftharpoons Sn(OH)_{4(s)} + 2e^- \qquad (8)$$

$$Sn(OH)_{4(s)} + 2OH^-_{(aq)} \rightarrow SnO_{2(s)} + 2H_2O_{(l)} \quad (9)$$

The experimental investigation conducted in 0.1 mol dm^{-3} NaCl was performed under open circuit potential conditions. The absence of $Sn(OH)_4$ and SnO_2 as corrosion products on the $Sn_{77}Sb_{23}$ coatings can be attributed to this specific experimental setup.

CONCLUSIONS

SEM and EDS analyses demonstrated that the electrodeposits' morphology exhibited a uniform distribution of dendritic clusters, and the occurrence of grains with different sizes was evident with increasing Sb content (63%). Characterization by XRD revealed the presence of crystalline phases of Sn, Sb, SbSn and intermetallic phases Cu_2Sb, Cu_6Sn_5 and $Cu_6(Sn,Sb)_5$. Polarization tests in 0.1 mol L^{-1} NaCl medium determined R_p values equal to 4597, 14692 and 1805 kΩ cm^{-2}. Immersion tests were carried out for 24 h and 48 h, and it was observed that the morphology of $Sn_{77}Sb_{23}$ did not change with the immersion time. XRD analyses for the coatings showed the presence of SnO, SnSb and Sb_2O_4 for both immersion times. When polarizing the coatings in NaCl for 1 h, SnO_2, SnSb and SnO phases were observed for –0.1 V and SnO, Cu_2O, Sb_2O_3, SnSb, Sb_2O_3 for 0.2 V. By EIS, the R_{CT1} values for the Sn, $Sn_{77}Sb_{23}$ and $Sn_{37}Sb_{63}$ coatings were 1.15; 10.5 and 1.46 kΩ cm^2, respectively. R_{CT2} values were 12.5; 7.43 and 2.7 kΩ cm^2. Consistent with the R_p values, the results suggested a correlation between corrosion resistance and the percentage of Sb, indicating increased corrosion resistance for $Sn_{77}Sb_{23}$.

ACKNOWLEDGMENTS

This study was financed in part by the Coordenação de Aperfeiçoamento de Pessoal de Nível Superior - Brasil (CAPES), Conselho Nacional de Desenvolvimento Científico e Tecnológico (CNPq) and Fundação Cearense de Apoio ao Desenvolvimento Científico e Tecnológica (FUNCAP). A. N. Correia gratefully acknowledges the funding provided by CNPq (proc. 305103/2022-9). P. de Lima-Neto thanks the financial support received from CNPq (proc. 302825/2022-3). N. G. Sousa by CNPq (proc. 141171/2021-9). Ana. A. C. Alcanfor thanks CAPES for her grants. The authors thank the Central Analítica-UFC/CT-INFRA/MCTI-SISANO/Pró-Equipamentos CAPES and Laboratório de Raios-X (UFC) for their support.

REFERENCES

[1]. Wang, R. Y.; Yuan, Z. F.; Zhao, H. X.; Yang, X.; Hao, Y. H.; Trans. Nonferrous Met. Soc. China **2023**, 33, 1839-1850. https://doi.org/10.1016/S1003-6326(23)66226-0

[2]. Wang, X.; Zhang, L.; Li, M. L.; J. Mater. Sci.: Mater. Electron. **2022**, 33, 2259–2292. https://doi.org/10.1007/s10854-021-07437-6

[3]. Lakshmi, D.; Jayapandi, S.; Nalini, B.; Selvin, P. C.; Semicond Sci Technol. **2020**, 35, 045008. 10.1088/1361-6641/ab708d

[4]. Huang, H. H.; Fan, X.; Singh, D. J.; Zheng, W. T.; J. Mater. Chem. C. **2019**, 7, 10652-10662. https://doi.org/10.1039/C9TC02876E

[5]. Schneider, M.; Langklotz, U.; Körsten, O.; Gierth, U.; Mater. Corros. **2023**, 74, 920–928. https://doi.org/10.1002/maco.202213718

[6]. Lucas, F. W. S.; Lima, F. H. B.; ChemElectroChem **2020**, 7, 3733–3742. https://doi.org/10.1002/celc.202000769

[7]. Gamburg, Y. D.; Zangari, G. Springer Science & Business Media. https://doi.org/10.1007/978-1-4419-9669-5 2011.

[8]. Li, A.; Bai, X.; Xie, Y.; Xia, P.; Bao, H.; He, M.; Zeng, X.; Yang, W.; Li, X.; Chemosphere 2023, 336, 139097. https://doi.org/10.1016/j.chemosphere.**2023**.139097

[9]. He, Z.; Yu, C.; Liu, J.; Miao, Z.; Wang, Y.; Coatings **2023**, 13,866. https://doi.org/10.3390/coatings13050866

[10]. Liu, S.; Ma, L.; Zhen, C.; Li, D.; Wang, Y.; Jia, Q.; Guo, F.; Appl. Energy **2023**, 352, 121997. https://doi.org/10.1016/j.apenergy.2023.121997

[11]. Schulze, M. C.; Belson, R. M.; Kraynak, L. A.; Prieto, A. L.; Energy Storage Materials **2020**, 25, 572–584. https://doi.org/10.1016/j.ensm.2019.09.025

[12]. Han, C.; Liu, Q.; Ivey, D. G. Electrochim. Acta **2008**, 53, 28, 8332-8340. https://doi.org/10.1016/j.electacta.2008.06.037

[13]. Huang, F. F.; Huang, M. L. J. Electrochem. Soc. **2018**, 165, D152. 10.1149/2.0721803jes

[14]. Hashimoto, H.; Nishimura, T.; Umetsu, Y. Mater. Trans. **2003**, 44, 1624-1629. https://doi.org/10.2320/matertrans.44.1624

[15]. Smith, E. L.; Abbott, A. P.; Ryder, K. S.; Chem. Rev. **2014**, 114, 11060−11082. https://doi.org/10.1021/cr300162p

[16]. Endres, F.; Abbott, A.; Macfarlane, D. R. John Wiley & Sons. **2017**

[17]. Chu, Q.; Wu, A.; Tan, T.; Guo, H.; Xiong, P.; Huang, S.; He, Y.; Appl. Surf. Sci. 2021, 550, 149322. https://doi.org/10.1016/j.apsusc.2021.149322

[18]. Abbott, A. P.; Curr. Opin. Green Sustainable Chem. 2022, 36, 100649. https://doi.org/10.1016/j.cogsc.2022.100649

[19]. Brandão, A. T. S. C.; Anicai, L.; Lazar O. A.; Rosoiu, S.; Pantazi, A.; Costa, R.; Enachescu, M.; Pereira, C. M.; Silva, A. F. Coatings, **2019**, 9, 798. https://doi.org/10.3390/coatings9120798

[20]. Gao, X.; Duan, B. Surf. Eng. **2014**, 30, 59-63. https://doi.org/10.1179/1743294413Y.0000000198

[21]. Anicai, L.; Petica, A.; Costovici, S.; Moise, C.; Brincoveanu, O.; Visan, T.; Coatings **2019**, 9, 800. https://doi.org/10.3390/coatings9120800

[22]. Su, Z.; CunyingXu, Hua, Y.; Li, J.; Ru, J.; Wang, M.; Xiong, L.; Zhang, Y.; Int. J. Electrochem. Sci. **2016**, 5, 3325-3338. https://doi.org/10.1016/S1452-3981(23)17402-5

[23]. Ma, J.; Prieto, A. L.; Chem. Commun. **2019**, 55, 6938-6941. https://doi.org/10.1039/C9CC00001A

[24]. Abtew, M.; Selvaduray, G. Reports **2000**, 27, 95-141. https://doi.org/10.1016/S0927-796X(00)00010-3

[25]. Cheng, S.; Huang, C. M.; Pecht, M.; Microelectron. Reliab. **2017**, 75, 77-95. https://doi.org/10.1016/j.microrel.2017.06.016

[26]. Vieira, L.; Schennach, R.; Gollas, B.; Electrochim. Acta **2016**, 197, 344–352. https://doi.org/10.1016/j.electacta.2015.11.030

[27]. Rosoiu, P. S.; Costovici, S. Moise, C.; Petica, A.; Anicai, L.; Visan, T.; Enachescu, M. Electrochim. Acta **2021**, 398, 139339. https://doi.org/10.1016/j.electacta.2021.139339

[28]. Sousa, N. G.; Oliveira R. V.; Alcanfor, A. A. C.; Feitosa, F. X.; Sant'Ana, H. B.; Schwarzacher, W.; De Lima Neto, P.; Monteiro, N. K. V.; Correia, A. N.; J. Mol. Liq. **2024**, 390, 122973. https://doi.org/10.1016/j.molliq.2023.122973

[29]. Anicai, L.; Petica, A.; Costovici, S.; Prioteasa, P.; Visan, T. Electrochim. Acta **2013**,114, 868-877. https://doi.org/10.1016/j.electacta.2013.08.043

[30]. Alcanfor, A. A. C.; da Silva, L. P.; de Oliveira, R. C.; Paulo, G. A.; Sousa, C. P.; Campos, O. S.; Dias, D. F.; Feitosa F. X.; de Sant'Ana, H. B.; Monteiro, N. K.V.; Correia, A. N.; de Lima-Neto. P. On the role of water in antimony electrodeposition from choline chloride/ethylene glycol/water mixture. J. Mol. Liq. **2024**, 399, 124416. https://doi.org/10.1016/j.molliq.2024.124416

[31]. Azpeitia, L. A.; Gervasi, C. A.; Bolzán, A. E.; J. Electroanal. Chem. **2023**, 944, 117637. https://doi.org/10.1016/j.jelechem.2023.117637

[32]. Zhao, J.; Sun, K.; Liang, G.; Xu, C.; Zhao, J.; Xue, F.; Zhou, J.; J. Mater. Res. Technol. **2021**, 15, 6726-6735. https://doi.org/10.1016/j.jmrt.2021.11.097

[33]. Park, M. S.; Needham, S. A.; Wang, G. X.; Kang, Y. M.; Park, J. S.; Dou, S. X.; Liu, H. K.; Chem. Mater. **2007**, 19, 2406–2410. https://doi.org/10.1021/cm0701761

[34]. Dias, M.; Verissimo, N. C.; Regone, N. N.; Freitas, E. S.; Cheung, N.; Garcia, A.; Corros. Eng., Sci. Technol. **2021**, 56, 11-21. https://doi.org/10.1080/1478422X.2020.1791446

[35]. Liu, G.; Khorsand, S.; JI, S.; J. Mater. Sci. Technol. **2019**, 35, 1618-1628. https://doi.org/10.1016/j.jmst.2019.03.026

[36]. Jaffery, H. A.; Sabri, M. F. M.; Said, S. M.; Hasan, S. W.; Sajid, I. H.; Nordin, N. I. M.; Hasnan, M. M. I. M.; Shnawah, D. A.; Moorthy, C. VKNSN.; J. Alloys Compd. **2019**, 810, 151925. https://doi.org/10.1016/j.jallcom.2019.151925

[37]. Shen, H.M; Han, X.Y; Zheng, X.M; Muniyandi, B.; Wang, J.K; Kang, Q.L.; Chen, M.G; Wu, Q.; Zhang, P.Y. Electrochim. Acta **2023**, 438, 141529. https://doi.org/10.1016/j.electacta.2022.141529

[38]. Bu, J.; Ru, J.; Wang, Z.; Hua, Y.; Xu, C.; Zhang, Y.; Wang, Y. Adv Powder Technol **2019**, 30, 2859-2867. https://doi.org/10.1016/j.apt.2019.06.027

[39]. Liu, J.; Park, S.; Nagao, S.; Nogi, M.; Koga, H.; Ma, J.; Zhang, G.; Suganuma, K.; Corros. Sci. **2015**, 92, 263-271. https://doi.org/10.1016/j.corsci.2014.12.014

[40]. Liao, B.; Cen, H.; Chen, Z.; Guo, X.; Corros. Sci. **2018**, 143, 347-361. https://doi.org/10.1016/j.corsci.2018.08.041

[41]. Jaiswal, D.; Kumar, S.; Behera, C. K.; Mater. Today Commun. **2022**, 33, 104627. https://doi.org/10.1016/j.mtcomm.2022.104627

[42]. Łosiewicz, B.; Budniok, A.; Rówiński, E.; Łągiewka, E.; Lasia, A.; Int. J. Hydrogen Energy **2004**, 29, 145-157. https://doi.org/10.1016/S0360-3199(03)00096-X

[43]. Kramer, M.; Tomkiewicz, M.; J. Electrochem. Soc. **1984**, 131, 1283, https://doi.org/10.1149/1.2115807

[44]. Metikoš-huković, M.; Babić, R.; Corros. Sci. **2007**, 49, 3570-3579. https://doi.org/10.1016/j.corsci.2007.03.023

[45]. Burashnikova, M. M.; Kazarinov, I. A.; Zotova, I. V.; J. Power Sources, **2012**, 207, 19-29. https://doi.org/10.1016/j.jpowsour.2011.12.042

[46]. Yan, Q.; Zhang, H.; Man, C.; Pang, K.; Wang, X.; Cui, Z.; Cui, H.; J. Mater. Eng. Perform. **2023**, 1-16. https://doi.org/10.1007/s11665-023-08771-y

[47]. Zhang, Q.; Li, Q.; Chen, X.; RSC Adv. 2021, 11, 1332-1342. https://doi.org/10.1039/D0RA08986A

[48]. Kapusta, S. D.; Hackerman, N.; Electrochim. Acta, **1980**, 25, 1625-1639. https://doi.org/10.1016/0013-4686(80)80016-8

[49]. Pourbaix, M. 1ª, Pergamon Press, **1966**.

[50]. Yan, Z.; Xian, A. Ping.; Metall. Mater. Trans. A, **2013**, 44, 1462-1474. https://doi.org/10.1007/s11661-012-1480-2

Supplementary Material

Electrochemical corrosion evaluation of SnSb electrodeposited coatings

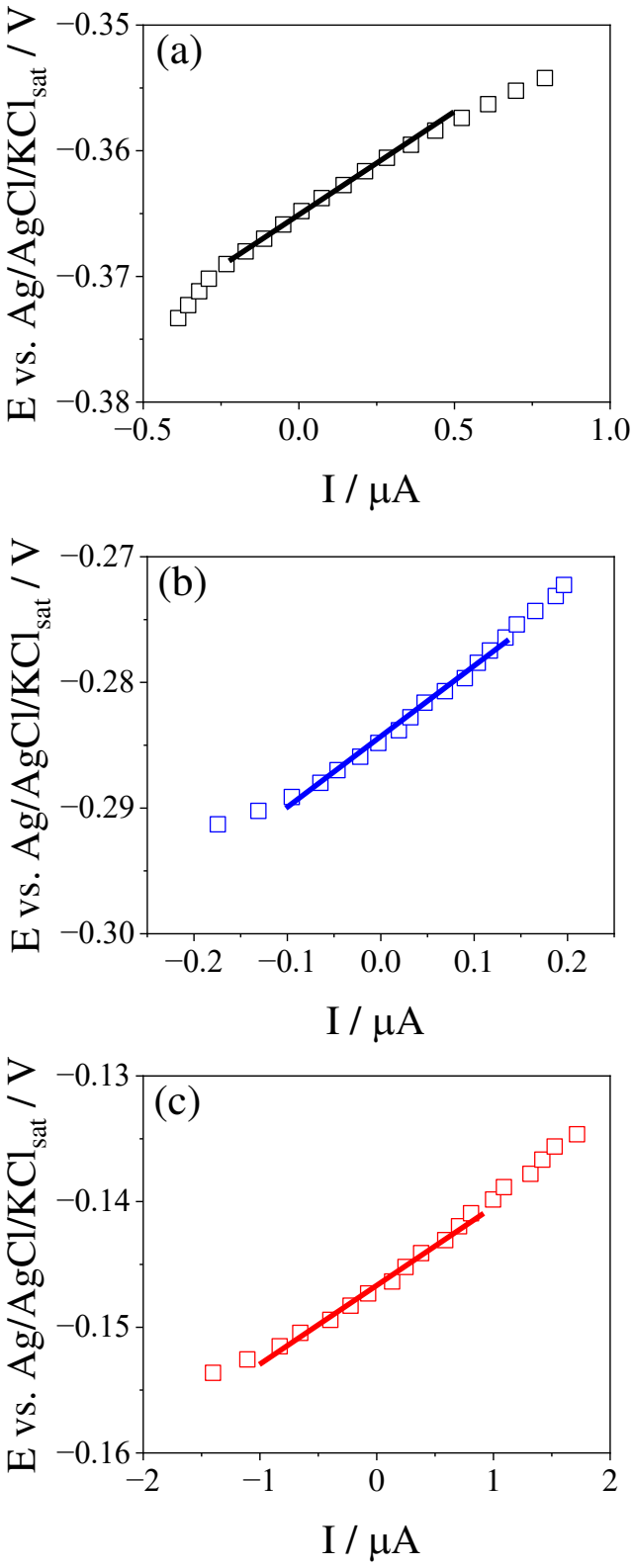

Figure S1. Linear fittings for (a) Sn, (b) $Sn_{77}Sb_{23}$ and (c) $Sn_{37}Sb_{63}$ coatings to calculate the values of R_p, considering ±10 mV in relation to E_{ocp}. Scan rate 0.5 mV s^{-1}.

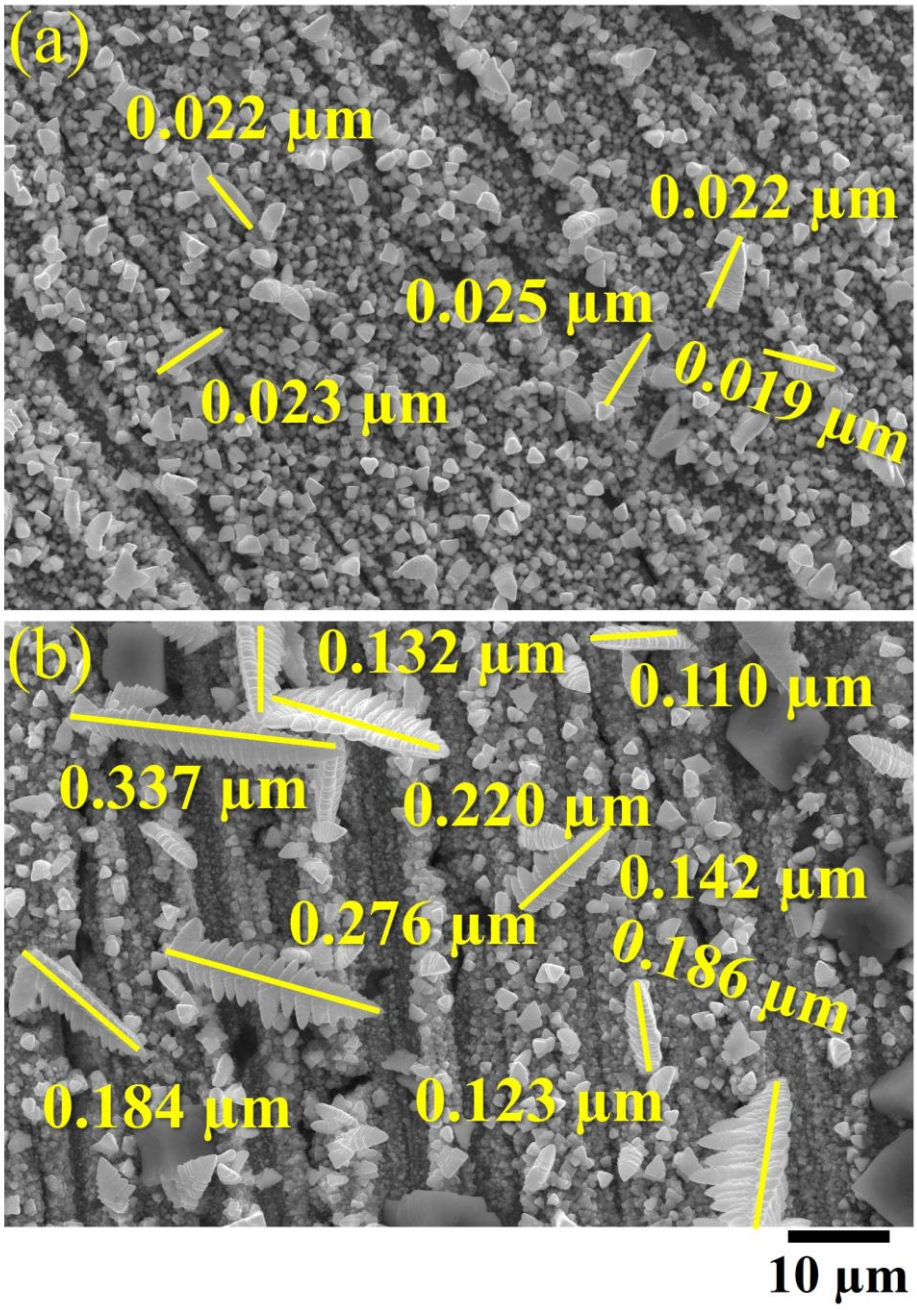

Figure S2. SEM images for $Sn_{37}Sb_{63}$ coating for (a) 24 h and (b) 48 h of immersion tests, both treated with ImageJ.

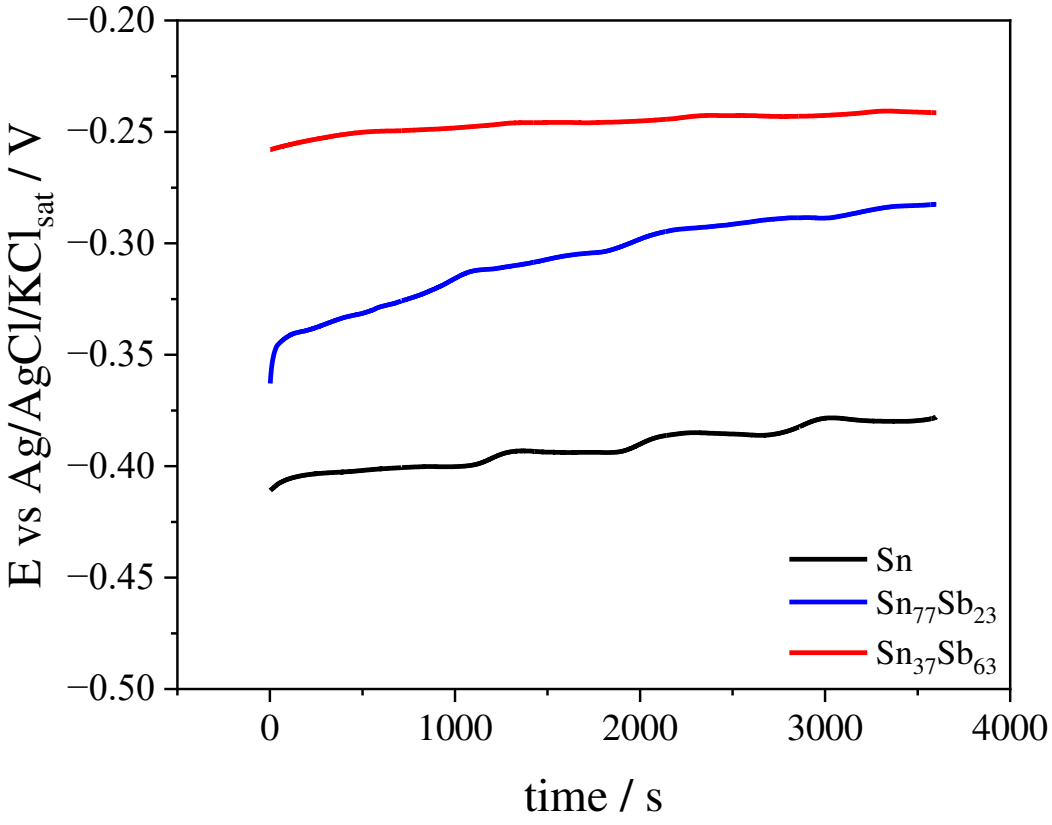

Figure S3. Open circuit potential measurements for SnSb coatings.

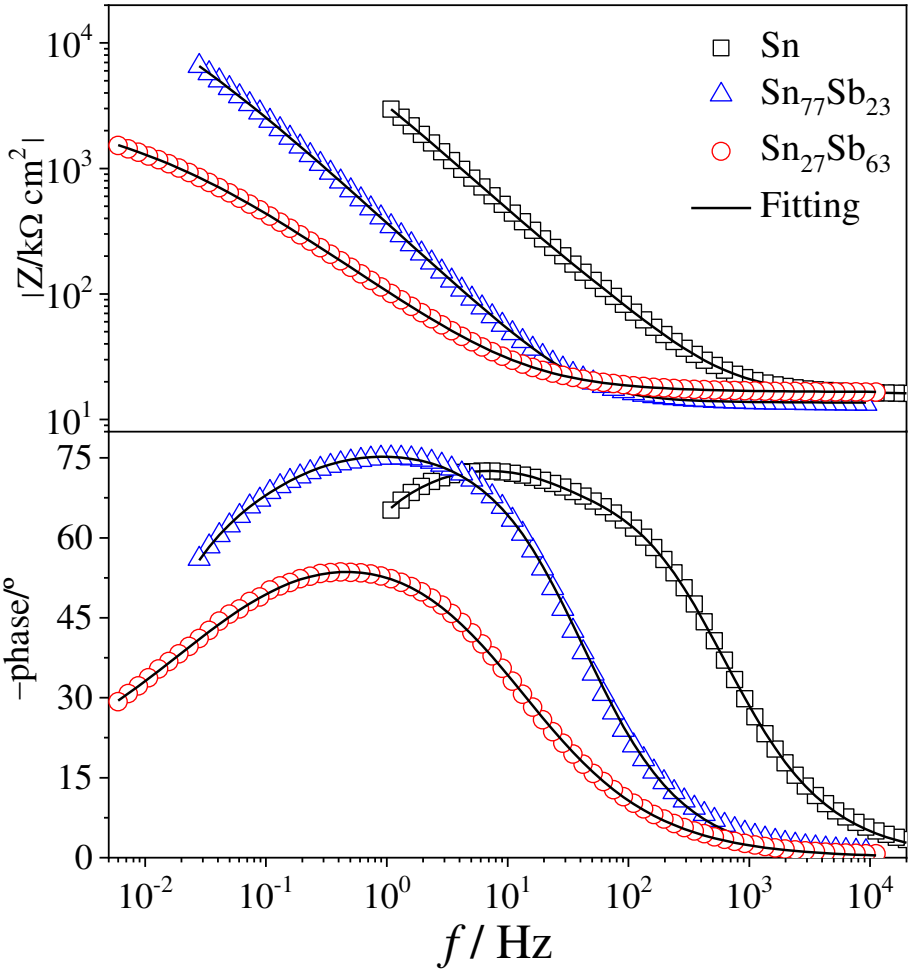

Figure S4. Bode diagrams for SnSb coatings.

4 CONCLUSÕES

Portanto, neste trabalho o solvente eutético formado pela mistura de cloreto de colina e etilenoglicol foi empregada com sucesso para os dois manuscritos desenvolvidos.

No primeiro manuscrito, o solvente eutético na ausência e presença de água foi utilizada com sucesso para eletrodeposição de Sb na superfície de Pt a 297 K e 338 K sem a necessidade de adição de aditivos complexos. O voltamograma cíclico realizado no eletrodo de Pt da solução eletrolítica contendo o Sb^{3+} mostrou, na varredura direta, um pico catódico bem definido correspondente à redução de Sb^{3+}/Sb. A análise SEM mostrou morfologias dendríticas semelhantes para filmes de Sb obtidos com adição de água a 297 K. Enquanto isso, foram obtidas estruturas de folha para todos os filmes de Sb a 338 K. Finalmente, a caracterização por DRX revelou que os eletrodepósitos de Sb apresentavam uma estrutura cristalina romboédrica com fases puras para todas as amostras.

As simulações DFT para sistemas DES e $SbCl_3$ sem H_2O e com quantidades variadas de moléculas de H_2O favoreceram o sistema no aumento da afinidade eletrônica. Além disso, houve forte tendência de adição de H_2O, causando diminuição da densidade eletrônica dos íons Sb^{3+} com os átomos em todos os sistemas estudados. Esses resultados indicaram uma possível explicação para a eletrodeposição ser favorecida neste tipo de sistema na presença de moléculas de H_2O. Por fim, as simulações computacionais quânticas indicaram que a interação Sb-Cl é mais forte, o que sugere a formação de complexos Sb-Cl e que a adição de moléculas de água favorece a afinidade eletrônica dos sistemas, e os resultados do QTAIM sugeriram que este aditivo diminuiu a densidade eletrônica de íons Sb^{3+}.

No segundo manuscrito, conclui-se que os revestimentos de $Sn_xSb_{(1-x)}$ eletrodepositados a partir de 1ChCl:2EG em cobre apresentam diferentes comportamentos de corrosão dependendo da composição e do teor de Sb. A adição de Sb^{3+} aos revestimentos de Sn resulta em uma modificação nas propriedades eletroquímicas, melhorando a resistência à corrosão, especialmente para as amostras com maior teor de Sn. O $Sn_{77}Sb_{23}$, por exemplo, mostrou boa resistência à corrosão, com uma região passiva observada nas curvas de polarização e valores elevados de resistência à polarização (R_p). Em contraste, o $Sn_{37}Sb_{63}$ exibiu uma dissolução ativa no eletrólito, indicando menor resistência à corrosão. As análises de DRX confirmaram a formação de fases SbSn, como Cu_2Sb e Cu_6Sn_5, com a evolução das fases durante os testes de imersão, sugerindo que a composição do revestimento afeta diretamente a estabilidade das fases e sua resistência à corrosão. Os testes de EIS corroboram a tendência de que a presença de Sb^{3+} melhora a resistência à corrosão, particularmente nas amostras com

maior conteúdo de Sn, como o $Sn_{77}Sb_{23}$. Esses resultados indicam que o controle da concentração de Sb no revestimento pode ser uma estratégia eficaz para otimizar as propriedades de resistência à corrosão de revestimentos eletrodepositados de SnSb.

REFERÊNCIAS

ABBOTT, Andrew P. *et al*. Preparation of novel, moisture-stable, Lewis-acidic ionic liquids containing quaternary ammonium salts with functional side chains. **Chemical Communications**, [*S.l.*], n. 19, p. 2010-2011, 2001.

ABBOTT, Andrew P. *et al*. Novel solvent properties of choline chloride/urea mixtures. **Chemical Communications**, [*S.l.*], n. 1, p. 70-71, 2003.

ABBOTT, Andrew P. *et al*. Deep Eutectic Solvents Formed between Choline Chloride and Carboxylic Acids: versatile alternatives to ionic liquids. **Journal of the American Chemical Society**, [*S.l.*], v. 126, n. 29, p. 9142-9147, 2004.

ABBOTT, Andrew P. *et al*. Speciation, physical and electrolytic properties of eutectic mixtures based on $CrCl_3 \cdot 6H_2O$ and urea. **Physical Chemistry Chemical Physics**, [*S.l.*], v. 16, n. 19, p. 9047-9055, 2014.

ABBOTT, Andrew P. *et al*. A comparative study of nickel electrodeposition using deep eutectic solvents and aqueous solutions. **Electrochimica Acta**, [*S.l.*], v. 176, p. 718-726, 2015.

ABBOTT, Andrew P. *et al*. Bright metal coatings from sustainable electrolytes: the effect of molecular additives on electrodeposition of nickel from a deep eutectic solvent. **Physical Chemistry Chemical Physics**, [*S.l.*], v. 19, n. 4, p. 3219-3231, 2017.

ABBOTT, Andrew P. Deep eutectic solvents and their application in electrochemistry. **Current Opinion in Green and Sustainable Chemistry**, [*S.l.*], v. 36, p. 100649, 2022.

ABO-HAMAD, Ali *et al*. Potential applications of deep eutectic solvents in nanotechnology. **Chemical Engineering Journal**, [*S.l.*], v. 273, p. 551-567, 2015.

ALCANFOR, Ana A.C. *et al*. Electrodeposition of indium on copper from deep eutectic solvents based on choline chloride and ethylene glycol. **Electrochimica Acta**, [*S.l.*], v. 235, p. 553-560, 2017.

AMORIM, Laudenor *et al*. Analysis of Fe^{2+} and Mn^{2+} ions in DES and water: A theoretical study using molecular dynamic simulations, QTAIM and NCI-RDG. **Colloids and Surfaces A**: Physicochemical and Engineering Aspects, [*S.l.*], v. 674, p. 131818, 2023.

ANICAI, Liana *et al*. Electrodeposition of Sn and NiSn alloys coatings using choline chloride based ionic liquids: Evaluation of corrosion behavior. **Electrochimica Acta**, [*S.l.*], v. 114, p. 868-877, 2013.

AZZOUZ, Amirah; HAYYAN, Maan. Potential applications of deep eutectic solvents in nanotechnology: part II. **Chemical Engineering Journal**, [*S.l.*], v. 468, p. 143563, 2023.

BERNASCONI, R. *et al*. Electrodeposition from deep eutectic solvents. **Progress and developments in Ionic Liquids**, [*S.l.*], p. 235-261, 2017.

BEZERRA-NETO, João R. *et al*. The effect of water on the physicochemical properties of an ethylene glycol and choline chloride mixture containing Cu^{2+} ions: electrochemical results and dynamic molecular simulation approach. **Physical Chemistry Chemical Physics**, [*S.l.*], v. 20, n. 14, p. 9321-9327, 2018.

BEZERRA-NETO, João R. *et al*. Molecular approach about the effect of water on the electrochemical behaviour of Ag^{+} ions in urea-choline chloride-water mixture. **Journal of Molecular Modeling**, [*S.l.*], v. 26, p. 1-9, 2020.

BEZERRA, Lucas Lima *et al*. Electrochemical and theoretical investigation on the behavior of the Co^{2+} ion in three eutectic solvents. **Journal of Molecular Graphics and Modelling**, [*S.l.*], v. 112, p. 108137, 2022.

BEZERRA, Lucas Lima *et al*. Analysis of temperature effect in the CO_2 absorption using a deep eutectic solvent: An in silico approach. **Journal of Molecular Graphics and Modelling**, [*S.l.*], v. 126, p. 108649, 2024.

CASCIANO, Paulo N.S. *et al*. Factorial design in the electrodeposition of Co-Mo coatings and their evaluations for hydrogen evolution reaction. **Journal of Alloys and Compounds**, [*S.l.*], v. 723, p. 164-171, 2017.

FASHU, S. *et al*. Influence of electrodeposition conditions on the microstructure and corrosion resistance of Zn-Ni alloy coatings from a deep eutectic solvent. **Surface and Coatings Technology**, [*S.l.*], v. 242, p. 34-41, 2014.

GAMBURG, Yuliy D.; ZANGARI, Giovanni. **Theory and practice of metal electrodeposition**. London: Springer Science & Business Media, 2011.

GARCÍA-ÁLVAREZ, Joaquín. Deep eutectic mixtures: Promising sustainable solvents for metal-catalysed and metal-mediated organic reactions. **European Journal of Inorganic Chemistry**, [*S.l.*], v. 2015, n. 31, p. 5147-5157, 2015.

GRAY, J.E.; LUAN, B. Protective coatings on magnesium and its alloys: a critical review. **Journal of Alloys and Compounds**, [*S.l.*], v. 336, n. 1-2, p. 88-113, 2002.

HANSEN, Benworth B. *et al*. Deep Eutectic Solvents: A review of fundamentals and applications. **Chemical Reviews**, [*S.l.*], v. 121, n. 3, p. 1232-1285, 2020.

KOVÁCS, Attila. *et al*. Modeling the physicochemical properties of natural deep eutectic solvents. **ChemSusChem**, [*S.l.*], v. 13, n. 15, p. 3789–3804, 2020.

KUDŁAK, Błażej; OWCZAREK, Katarzyna; NAMIEŚNIK, Jacek. Selected issues related to the toxicity of ionic liquids and deep eutectic solvents: a review. **Environmental Science and Pollution Research**, [*S.l.*], v. 22, n. 16, p. 11975–11992, 2015.

LI, Xiaoxia; ROW, Kyung H. Development of deep eutectic solvents applied in extraction and separation. **Journal of separation science**, [*S.l.*], v. 39, n. 18, p. 3505–3520, 2016.

LIU, Fan *et al*. Electrodeposition of metals and alloys from ionic liquids. **Journal of Alloys**

and Compounds, [*S.l.*], v. 654, p. 163–170, 2016.

MARTINS, Mónia A.R.; PINHO, Simão P.; COUTINHO, João A.P. Insights into the nature of eutectic and deep eutectic mixtures. **Journal of Solution Chemistry**, [*S.l.*], v. 48, p. 962–982, 2019.

MBOUS, Yves Paul *et al*. Applications of deep eutectic solvents in biotechnology and bioengineering: Promises and challenges. **Biotechnology advances**, [*S.l.*], v. 35, n. 2, p. 105–134, 2017.

MESSIER, Russell. Electrodeposition: the materials science of coatings and substrates. **Advanced Materials**, [*S.l.*], v. 6, n. 1, p. 88–89, 1993.

OLIVEIRA, Francisco. G.S. *et al*. Fe-Co coatings electrodeposited from eutectic mixture of choline chloride-urea: physical characterizations and evaluation as electrocatalysts for the hydrogen evolution reaction. **Journal of Alloys and Compounds**, [*S.l.*], v. 851, p. 156330, jan. 2021.

OLIVEIRA, Francisco G.S. *et al*. $Fe_xNi_{(1-x)}$ coatings electrodeposited from choline chloride-urea mixture: magnetic and electrocatalytic properties for water electrolysis. **Materials Chemistry and Physics**, [*S.l.*], v. 279, p. 125738, 2022.

OLIVEIRA, Renato Veríssimo de *et al*. Analysis of the behavior of Sn^{2+} and In^{3+} ions in DES and in water: A theoretical approach. **Journal of Molecular Liquids**, [*S.l.*], v. 353, p. 118774, 2022.

PEREIRA, Juliermes C. *et al*. Effects of electrodeposition parameters on corrosion resistance of ZnSn coatings on carbon steel obtained from eutectic mixture based on choline chloride and ethylene glycol. **Journal of Alloys and Compounds**, [*S.l.*], v. 886, p. 161159, 2021.

PEREIRA, Juliermes C. *et al*. Electrochemical corrosion evaluation of new Zn-Sn-In coatings electrodeposited in a eutectic mixture containing choline chloride and ethylene glycol. **Electrochimica Acta**, [*S.l.*], v. 407, p. 139647, 2022.

PEREIRA, Nuno M. *et al*. Zn–Sn electrodeposition from deep eutectic solvents containing EDTA, HEDTA, and Idranal VII. **Journal of Applied Electrochemistry**, [*S.l.*], v. 42, p. 561-571, 2012.

PERKINS, Sasha L.; PAINTER, Paul; COLINA, Coray M. Experimental and computational studies of choline chloride-based deep eutectic solvents. **Journal of Chemical & Engineering Data**, [*S.l.*], v. 59, n. 11, p. 3652-3662, 2014.

PERNA, Filippo Maria; VITALE, Paola; CAPRIATI, Vito. Deep eutectic solvents and their applications as green solvents. **Current Opinion in Green and Sustainable Chemistry**, [*S.l.*], v. 21, p. 27-33, 2020.

PINHEIRO, Daniela Mirema Lima *et al*. Ag^+ ion in choline chloride and glycerol mixture: Evaluation of electrochemical properties and molecular modelling approaches. **Journal of Molecular Liquids**, [*S.l.*], v. 371, p. 121053, 2023.

VANDA, Henni. Natural deep eutectic solvents: from their discovery to their applications. *In:* RAMÓN, Diego J. (Org.). **Deep eutectic solvents:** synthesis, properties, and applications. New Jersey: Wiley-VCH, 2019. p. 61–81.

VIGIER, Karine De Oliveira. Synthesis and properties. *In:* RAMÓN, Diego J. (Org.). **Deep eutectic solvents:** synthesis, properties, and applications. New Jersey: Wiley-VCH, 2019. p. 1–23.

RODRIGUES-JÚNIOR, Deomar N. *et al*. $Zn_xCo_{(1-x)}$ coatings from choline chloride-ethylene glycol deep eutectic solvent as electrocatalysts for hydrogen evolution reaction. **Journal of Electroanalytical Chemistry**, [*S.l.*], v. 947, p. 117785, 2023.

RU, Juanjian *et al*. Preparation of sub-micrometer lead wires from PbO by electrodeposition in choline chloride-urea deep eutectic solvent. **Advanced Powder Technology**, [*S.l.*], v. 26, n. 1, p. 91-97, 2015.

SANTOS, Luis P.M. dos *et al*. Electrodeposition of 1-D tellurium nanostructure on gold surface from choline chloride-urea and choline chloride-ethylene glycol mixtures. **Journal of Molecular Liquids**, [*S.l.*], v. 288, p. 111038, 2019.

SEMEDO, Ronnie A.R. *et al*. Evaluation of corrosion resistance of Zn_x-Mn_{1-x} coatings electrodeposited on 1020 carbon steel rotating electrode from choline chloride and urea at eutectic composition. **Materials Chemistry and Physics**, [*S.l.*], v. 307, p. 128074, 2023.

SIMKA, Wojciech; PUSZCZYK, Dagmara; NAWRAT, Ginter. Electrodeposition of metals from non-aqueous solutions. **Electrochimica Acta**, [*S.l.*], v. 54, n. 23, p. 5307-5319, 2009.

SMITH, Emma L.; ABBOTT, Andrew P.; RYDER, Karl S. Deep eutectic solvents (DESs) and their applications. **Chemical reviews**, [*S.l.*], v. 114, n. 21, p. 11060-11082, 2014.

SONG, Yuexian *et al*. Interfacial assistant role of amine additives on zinc electrodeposition from deep eutectic solvents: an in situ X-ray imaging investigation. **Electrochimica Acta**, [*S.l.*], v. 240, p. 90-97, 2017.

SOUSA, Natalia G. *et al*. One-step preparation of silver electrodeposits from non-aqueous solvents. **Journal of Molecular Liquids**, [*S.l.*], v. 288, p. 111091, 2019.

SOUSA, Natalia G. *et al*. Modelling approach applied to SnIn coatings from choline chloride/ethylene glycol deep eutectic solvent. **Journal of Molecular Liquids**, [*S.l.*], v. 390, p. 122973, 2023.

STEFANOVIC, Ryan *et al*. Nanostructure, hydrogen bonding and rheology in choline chloride deep eutectic solvents as a function of the hydrogen bond donor. **Physical Chemistry Chemical Physics**, [*S.l.*], v. 19, n. 4, p. 3297-3306, 2017.

SUDAGAR, Jothi; LIAN, Jianshe; SHA, Wei. Electroless nickel, alloy, composite and nano coatings–A critical review. **Journal of alloys and compounds**, [*S.l.*], v. 571, p. 183-204, 2013.

TANG, Baokun; ZHANG, Heng; ROW, Kyung Ho. Application of deep eutectic solvents in

the extraction and separation of target compounds from various samples. **Journal of separation science**, [*S.l.*], v. 38, n. 6, p. 1053-1064, 2015.

TOLMACHEV, Dmitry *et al*. Computer simulations of deep eutectic solvents: Challenges, solutions, and perspectives. **International journal of molecular sciences**, [*S.l.*], v. 23, n. 2, p. 645, 2022.

TOMÉ, Luciana I.N. *et al*. Deep eutectic solvents for the production and application of new materials. **Applied Materials Today**, [*S.l.*], v. 10, p. 30-50, 2018.

TROTER, Dragan Z. *et al*. Application of ionic liquids and deep eutectic solvents in biodiesel production: A review. **Renewable and Sustainable Energy Reviews**, [*S.l.*], v. 61, p. 473-500, 2016.

URCEZINO, Amanda S.C. *et al*. Electrodeposition study of Ni coatings on copper from choline chloride-based deep eutectic solvents. **Journal of the Brazilian Chemical Society**, [*S.l.*], v. 28, n. 07, p. 1193-1203, 2017.

VELEZ, Caroline; ACEVEDO, Orlando. Simulation of deep eutectic solvents: Progress to promises. **Wiley Interdisciplinary Reviews:** Computational Molecular Science, [*S.l.*], v. 12, n. 4, p. e1598, 2022.

VIJAYAKUMAR, Jeyasankar *et al*. Electrodeposition of Ni–Co–Sn alloy from choline chloride-based deep eutectic solvent and characterization as cathode for hydrogen evolution in alkaline solution. **International journal of hydrogen energy**, [*S.l.*], v. 38, n. 25, p. 10208-10214, 2013.

WAGLE, Durgesh V.; ZHAO, Hua; BAKER, Gary A. Deep eutectic solvents: sustainable media for nanoscale and functional materials. **Accounts of chemical research**, [*S.l.*], v. 47, n. 8, p. 2299-2308, 2014.

XIE, Xueliang *et al*. Electrodeposition of Zn and Cu-Zn alloy from ZnO/CuO precursors in deep eutectic solvent. **Applied Surface Science**, [*S.l.*], v. 385, p. 481-489, 2016.

XUE, Zhimin. Electrochemistry. *In:* RAMÓN, Diego J. (Org.). Deep eutectic solvents: synthesis, properties, and applications. New Jersey: Wiley-VCH, 2019. p. 335–362.

ZHANG, Qinghua *et al*. Deep eutectic solvents: syntheses, properties and applications. **Chemical Society Reviews**, [*S.l.*], v. 41, n. 21, p. 7108-7146, 2012.

ZHEKENOV, Temirlan *et al*. Formation of type III Deep Eutectic Solvents and effect of water on their intermolecular interactions. **Fluid Phase Equilibria**, [*S.l.*], v. 441, p. 43-48, 2017.

ANEXO A – MANUSCRITO 1

Article

ELECTROCHEMICAL CORROSION EVALUATION OF SnSb ELECTRODEPOSITED COATINGS

Ana Aline C. Alcanfor[a], Natalia G. Sousa[a], Othon S. Campos[b,*], Alan S. de Menezes[c], Edipo S. de Oliveira[d], Hamilton F. G. de Abreu[d], Paulo N. S. Casciano[a], Pedro de Lima Neto[a,*] and Adriana N. Correia[a,*,*]

[a]Departamento de Química Analítica e Físico-Química, Universidade Federal do Ceará, Campus do Pici, 60440-900 Fortaleza – CE, Brasil

[b]Departamento de Química e Física, Universidade Federal do Espírito Santo, Campus de Alegre, 29500-000 Alegre – ES, Brasil

[c]Departamento de Física, Universidade Federal do Maranhão, Campus Universitário do Bacanga, 65080-805 São Luís – MA, Brasil

[d]Departamento de Engenharia Metalúrgica e de Materiais, Universidade Federal do Ceará, Campus do Pici, 60020-181 Fortaleza – CE, Brasil

Received: 06/13/2024; accepted: 10/30/2024; published online: 12/10/2024

$Sn_xSb_{(1-x)}$ coatings were electrodeposited from 1ChCl:2EG on copper. The corrosion resistance of the electrodeposits was evaluated in 0.1 mol dm^{-3} of NaCl. The characterization was performed by scanning electron microscopy (SEM), energy dispersive X-ray spectroscopy (EDS), and X-ray diffraction (XRD). Voltammetric profiles showed that the electrodeposition potential shifted towards less positive values with increasing Sb^{3+} concentration. SEM images revealed that the coatings exhibited grains and clusters. EDS analyses showed that the Sb content increased with the Sb^{3+} concentration. XRD results indicated the formation of the SbSn phases such as Cu_2Sb, Cu_6Sn_5, and $Cu_6(Sn,Sb)_5$. The potentiodynamic polarization (PP) curves showed that Sn and $Sn_{77}Sb_{23}$ presented a passive potential region, while $Sn_{37}Sb_{63}$ had an active dissolution in the electrolyte. Immersion tests were performed for 24 h and XRD results revealed Cu, Sn, SnO, SbSn and Sb_2O_4 phases. Considering 48 h, Cu, CuSn, SnO_2 and SnSb phases were identified. The polarization resistance values of 4.60, 14.69 and 1.81 kΩ cm^2 were achieved for Sn, $Sn_{77}Sb_{23}$, and $Sn_{37}Sb_{63}$, respectively. The EIS results suggested that adding Sb^{3+} improves corrosion resistance for SnSb samples with higher Sn content. For $Sn_{77}Sb_{23}$, the charge transfer resistance was 10.5 kΩ cm^2, for Sn and $Sn_{37}Sb_{63}$ 1.15 and 1.46 kΩ cm^2, respectively.

Keywords: $Sn_xSb_{(1-x)}$ coatings; electrodeposition; deep eutectic solvent; corrosion.

INTRODUCTION

Currently, tin (Sn), antimony (Sb) and $Sn_xSb_{(1-x)}$ alloys are promising materials for a variety of applications. These include their use as alloys for welding,[1,2] semiconductors,[3] thermoelectrics,[4] anode materials for metal-ion batteries,[3] anticorrosive coatings[5] and as electrocatalysts for electrochemical reduction of CO_2.[6] The electrodeposition technique, one of the several methods for preparing these coatings, is particularly attractive for industrial practice. It offers a low cost, easy handling, the ability to control the thickness of the electrodeposited coating, and the capacity to obtain electrodeposited layers on metallic substrates of different geometries and shapes. Most importantly, the electrodeposits have excellent adherence to the substrate.[6-11]

However, the electrodepositions of Sn and Sb present several problems when carried out in an aqueous-based plating solution since there is a known hydrolysis in a neutral solution that Sn^{2+} undergoes (Equation 1).[12-14] This reaction leads to a formation of SnO, which is unstable in an aqueous solution and brings other hydrolysis reactions to form the SnO_2 (Equation 2). Finally, the Sb^{3+} cations can present problems with solvating in water once their solubility can be improved only by using strong acidic solutions (Equation 3).

$$Sn^{2+}_{(aq)} + H_2O_{(l)} \rightarrow SnO_{(s)} + 2H^+_{(aq)} \quad (1)$$

$$SnO_{(s)} + H_2O_{(l)} \rightarrow SnO_{2(s)} + 2H^+_{(aq)} + 2e^- \quad (2)$$

$$Sb^{3+}_{(aq)} + H_2O_{(l)} \rightarrow SbO^+_{(aq)} + 2H^+_{(aq)} \quad (3)$$

In this context, deep eutectic solvents (DES) offer a promising alternative for preparing electroplating solutions containing Sn^{2+} and Sb^{3+} ions since, unlike the traditional aqueous electroplating solutions, many chemical reactions that typically occur in water do not take place in DES. These organic solvents often contain only a small percentage of water, and consequently, the hydrolysis reactions involving Sn^{2+} and Sb^{3+} ions, as mentioned earlier, are less likely to occur. Also, the solubility of these metal salts is very high in these solvents as the DES polarity can be tuned by choosing the appropriate components to achieve polar or apolar behavior. In this context, $SnCl_2$ and $SbCl_3$ are highly soluble in DES-based formulation, and, therefore, electroplating solutions using these solvents can be prepared without adding any complexing addictive to maintain the Sn^{2+} and Sb^{3+} ions stable in the solution.

Nowadays, there is an increasing interest in developing ambiently more sustainable processes, which means searching for new processes and technologies that mitigate the environmental impacts of traditional industrial processes. Since the beginning of the first decade of the current century, DES have been investigated as an environmentally friendly alternative to water plating solutions for the electrodeposition of transition metals and their metallic alloys because their ions are stable in these solvents. In addition, DES are widely available, relatively inexpensive, biodegradable, and non-toxic[15] and, therefore, electrodeposited metallic layers can be achieved from these solvents without the addition of complexing agents, which gives to the electrodeposition of individual metal or metallic alloys in DES a potential to become, in the future, an industrial electroplating process associated to the sustainable development. Therefore, the interest in the electrodeposition of metals and alloys from DES is rising, as demonstrated in the literature review papers related to this subject, which have already been published.[16-18] Furthermore, Abbott[18] has

*e-mail: adriana@ufc.br

Associate Editor handled this article: Lucia Mascaro

used pilot projects for electroplating Ni, Fe and Zn to show that plating solutions based on DES have real potential for application in industrial practice.

Considering the deposition of Sn coatings in ethaline, Brandão *et al.*[19] used oxidized multi-walled carbon nanotubes (ox-MWCNT), pristine multi-walled carbon nanotubes (P-MWCNT) and reduced graphene oxide (rGO) over a metallic matrix using a glassy carbon electrode (GC) for comparison. The cyclic voltammograms showed a reduction peak around 0.6 V *vs.* Ag. The chronoamperometric analysis showed a 3D instantaneous process with diffusion-controlled growth. The Sn coating presented a topography by atomic force microscopy (AFM) showing round particles with different roughness in the function of the carbon electrode: the GC along ox-MWCNT presented higher values of roughness in comparison to P-MWCNT and rGO electrodes. Concerning the electrodeposition of Sn alloys, Gao *et al.*[20] studied the electrodeposition of Sn-Bi alloy coatings using ethaline with boric acid at 90 °C over a Cu electrode. The morphology of the alloy varied with the applied potential from a compact layer with small grain sizes to an unevenly distributed large grain, which shows the effect of the potential on the Sn-Bi alloy morphologies. Anicai *et al.*[21] presented SnIn electrodeposition using reline on copper, whose coating had 10-65 wt.% of In. The authors present that the In content in the electrodeposited layer is inversely proportional to the applied current density. The morphology showed irregular particles covering the substrate under direct electrodeposition conditions at 3 mA cm^{-2}. Moreover, corrosion electrochemical tests in 0.5 mol L^{-1} NaCl demonstrated that the electrodeposited SnIn coatings acted as an anticorrosion barrier. Lastly, the authors performed a thermogravimetric analysis, which showed that the electrodeposited coatings had a melting point of 400.7 K (Sn:In 50:50%) and 391.8 K (Sn:In 48:52%), which justifies the SnIn use as a lead-free welding solder.

Presently, there are few reports in the literature related to the electrodeposition of SnSb alloys from DES. For instance, Su *et al.*[22] successfully electrochemically prepared submicrometric SnSb alloy powders on a titanium substrate in DES medium formed by choline chloride-ethylene glycol (ChCl-EG, 1:2 molar ratio) containing 0.2 mol dm^{-3} $SbCl_3$ and 0.2 mol dm^{-3} $SnCl_2$ at 343 K. These authors showed that the applied electrodeposition potential had a significant effect on the alloy composition, but little influence on the morphology. Ma and Prieto[23] reported that the electrodeposition of pure phase SnSb as alloy-type anode material exhibits high stability for sodium-ion batteries. These authors electrodeposited SnSb thins films from ethylene (1:2 by weight ChCl:EG), and the electrochemical tests demonstrated that independent of SnSb composition, the electrode retained 95% of its initial capacity after 300 cycles at 0.5 A g^{-1}. This concern arose from the inadequate disposal of Pb waste arising from the manufacturing process and manufactured products.[24,25] The interest in the welding process of SnSb alloys is due to their good thermal fatigue resistance and high fracture strength properties, as pointed out by Wang *et al.*[1] Furthermore, these authors investigated the welding reliability of SnSb with different Sb contents on the Cu substrate. Therefore, due to the outstanding properties of SnSb alloys and the concern with the creation of a sustainable electroplating process for these alloys, this work aimed to electrodeposited $Sn_xSb_{(1-x)}$ alloys from a plating solution based on 1ChCl:2EG, without the addition of complexing agents, and to evaluate the effect of Sb content on the corrosion behavior of the $Sn_xSb_{(1-x)}$ electrodeposited coatings.

EXPERIMENTAL

Chemicals and electrolyte preparation

All chemicals in this study were used as received without any further purification. The eutectic mixture was prepared by mixing choline chloride (ChCl, Sigma-Aldrich®, ≥ 99%) and ethylene glycol (EG, Sigma-Aldrich®, ≥ 99.8%) in a molar ratio 1:2 (1ChCl:2EG) at 353 K until the formation of a colorless liquid. Next, anhydrous salts of tin(II) chloride and antimony(III) chloride ($SnCl_2$ and $SbCl_3$, Sigma-Aldrich®, ≥ 99%) were added to 1ChCl:2EG to form the plating solutions. The compositions of all plating solutions are listed in Table 1.

Table 1. Chemical composition of the plating solutions prepared by adding $SnCl_2$ and $SbCl_3$ to 1ChCl:2EG solvent

Bath	Electrolyte composition	
	$[Sn^{2+}]$ / (10^{-3} mol dm^{-3})	$[Sb^{3+}]$ / (10^{-3} mol dm^{-3})
I	50	-
II	50	10
III	50	50

Voltammetric measurements

The voltammetric experiments were conducted on a potentiostat/galvanostat model PGSTAT30 (Autolab, Metrohm-Eco Chemie) connected to a computer, using NOVA® software version 2.1.4. To investigate the electrochemical behavior of the Sn^{2+} and Sb^{3+} species in solution and to electrodeposit the $Sn_xSb_{(1-x)}$ coatings, a glass electrochemical cell with a Teflon® lid was used, which was coupled to a thermostatic bath for temperature control under atmospheric conditions. Before the obtention of the cyclic voltammograms, the working electrode was sanded on SiC silicon carbide 600 grit sandpaper, washed with Milli-Q water (18.2 MΩ cm), and dried with airflow. Initially, to characterize the surface of the working electrode in the 1ChCl:2EG mixture, cyclic voltammetry was obtained between –0.4 and –1.5 V. Next, to evaluate the electrochemical reduction of Sn^{2+} and Sb^{3+} species (baths I-III), linear sweep voltammetries were performed in the electrochemical potential range between –0.4 and –1.0 V. All voltammograms were recorded at 10 mV s^{-1} and 353 K. Cu disc (geometric surface area of 0.023 cm^2), a Pt plate (with 1.5 cm^2) and an $Ag_{(s)}/AgCl_{(s)}$ wire immersed in 1ChCl:2EG mixture, were used as the working, auxiliary and reference electrodes, respectively.

Electrodeposition and characterization

All $Sn_xSb_{(1-x)}$ coatings were electrodeposited on Cu discs (geometric area 0.18 cm^2) to characterize the surface morphologies, chemical compositions, and crystalline structures. The electrodeposits were obtained under potentiostatic control at –0.55 V and 353 K, with electric charge control to obtain coatings with a nominal thickness of 2 μm, estimated from Faraday's equation. The morphologies and chemical compositions of the obtained coatings were analyzed by a field emission gun-scanning electron microscopy (FEG-SEM, FEI-Quanta 450) coupled to an energy-dispersive X-ray spectrometer (EDS, Oxford Instruments INCA X-MAX). The particle size of electrodeposited coatings was determined using the ImageJ-Fiji software.[26] Finally, X-ray diffraction (XRD) analyses were carried out using a Bruker diffractometer, model D8 Advance, equipped with a LynxEye detector. The measurements were made with a Cu tube, operating at 40 kV and 40 mA, a range of 20 to 100 degrees, with a step size of 0.02 degrees and a counting time of 0.2 s $step^{-1}$. The experimental data was treated using PANalytical® X'Pert HighScore Plus® software,[27] and the crystalline phases were indexed using the crystallography PDF-22004 card files from the Inorganic Crystal Structure Database (ICSD).

Electrochemical corrosion tests

An electrochemical cell composed of three electrodes was used for corrosion tests. $Ag_{(s)}/AgCl_{(s)}/Cl^-$ (saturated KCl) was used as the reference electrode, a platinum foil of 1 cm^2 was the counter electrode, and the Cu recovered with the $Sn_xSb_{(1-x)}$ coatings was the working electrode. Before each experiment, the open circuit potential (E_{ocp}) was recorded as a function of time for 1 h. The potentiodynamic polarization curves were obtained in 0.1 mol dm^{-3} NaCl at 298 K and 0.5 mV s^{-1} and between –0.25 and +1.00 V around the E_{ocp}. All experiments were performed in duplicate. After sample preparation, the morphologies of the tested samples were evaluated after 24 and 48 h immersion in a 0.1 mol dm^{-3} NaCl solution. The effect of the potential applied in a 0.1 mol dm^{-3} NaCl medium, –0.1 and 0.2 V for 1 h was also evaluated. A copper disc with a geometric area of 0.28 cm^2 was used for these experiments. The electrochemical impedance spectroscopy results were obtained in 0.1 mol dm^{-3} NaCl at 298 K, applying 0 V to the E_{ocp} in the frequency range of 20 kHz to 6 mHz with a sinusoidal amplitude of 12 mV. Twelve points were collected by frequency decade. The validation of results considered Lissajous method.

RESULTS AND DISCUSSION

Electrochemical analyses

The insert in Figure 1 shows the cyclic voltammetry, at 353 K, obtained from 1ChCl:2EG on a copper surface in the potential range between –0.4 and –1.5 V. In this potential range, there is an increase in the cathodic current density at potential values from –1.2 V. This process is associated with the reduction of ethylene glycol hydroxyl groups, choline chloride cationic ions and traces of water.[28]

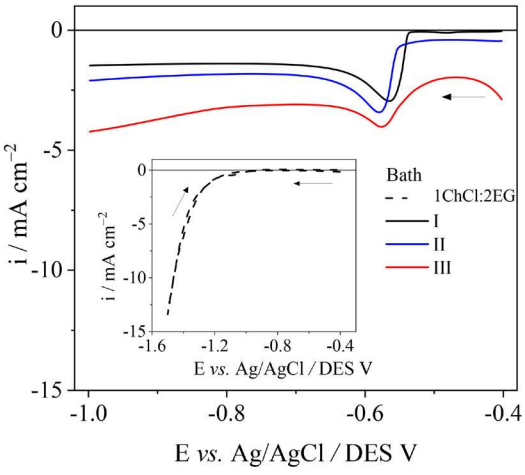

Figure 1. *Linear sweep voltammetry of the copper electrode in baths I, II and III at 353 K and 10 mV s^{-1}. The inset shows a cyclic profile obtained for a copper electrode in 1ChCl:2EG mixture at 353 K and 10 mV s^{-1}*

The electrochemical behaviors of Sn^{2+} and Sb^{3+} species were investigated by linear sweep voltammetry using a Cu electrode immersed in baths I-III, applying a potential range between –0.4 and –1.0 V at 10 mV s^{-1} and 353 K. The recorded voltammograms are shown in Figure 1. For bath I (black line), a single well-defined cathodic peak can be observed at –0.56 V, which is attributed to the electrochemical reduction of Sn^{2+} to metallic Sn. A similar voltammetric profile was reported[29-31] in a previous investigation for the electrodeposition of Sn.

Since the Sb content increases in baths II and III (blue and red lines), the voltammograms change regarding cathodic peak potential and total electrochemical charge. A similar system was used for Sb electrodeposition in the literature,[32] but a Pt disc was used as the working electrode. In this context, the peak potential of Sb^{3+} reduction at 298 K was located before –0.4 V since this electrode presents more electrochemical stability than the Cu substrate. Once undesired electrochemical reactions occur before –0.4 V in DES, the voltammogram for bath III (red line) presents a so-called "semi-peak" between –0.4 and –0.5 V due to the diffusion process of Sb^{3+} reduction. The subsequent peak around –0.58 V is related to the Sn^{2+} reduction, which was slightly shifted towards more negative potentials than pure Sn^{2+} bath I (black line). In bath II (blue line), having less Sb^{3+} than bath III, the cathodic peak seen in bath III does not appear, having the Sn^{2+} reduction process at –0.58 V. Although the hypothesis of co-deposition of the Sn^{2+} and Sb^{3+} was reported in the literature.[6]

Morphology, composition, and structural results

The SEM images shown in Figure 2 present an evolution of the grain structure from a cuboid-like in pure Sn to a pentagonal-like structure in $Sn_{37}Sb_{63}$. In Figure 2a, it is possible to see the body-centered tetragonal, once the cuboid structure is elongated in metallic islets. When Sb is added, there is a transition in the structure, as shown in Figure 2b, in which those islets do not appear due to the rhombohedral structure of Sb, which modulates the alloy grain size. Still, in this image, they are tiny alloy grains with pentagonal and hexagonal shapes, which could be related to the atomic position of the elements in the alloy that mixes both cuboid (from Sn) and rhombohedral (from Sb) structures. This observation is clearer in Figure 2c, which shows many pentagonal-like structures in the SnSb and other regular shapes, such as trigonal and cuboid. With the increase in the Sb content in the coatings, the rhombohedral structure is predominant, which causes those variations in the alloy grains. Compared with the pure Sn image (Figure 2a), Figures 2b and 2c exhibit a regular and compact layer, which is not seen in the pure Sn image. The Sn islets are deposited over an Sn layer; the electrodeposited Sn layer can be related to the voltammetric results shown in Figure 1, which shows a small peak at circa –0.47 V. Although the system is similar, having Sn^{2+} in ethaline using a copper electrode, the $Sn_{(ads)} \rightarrow Sn_{(abs)}$ step was not observed within the potential window of the copper electrode. Therefore, this Sn layer before the bulk Sn deposition was observed in both voltammetric and SEM experiments.

Furthermore, Figure 2a shows the grain clusters in pure Sn deposits. When Sb^{3+} is added to the electrolytic solution (Figure 2b), a reduction in the average size to 1.05 µm was observed, in addition to a non-uniform overlayer.[32] In Figure 2c, obtained from an equimolar solution of Sn^{2+} and Sb^{3+}, grains with distinct shapes (circular, pentagonal, and hexagonal) were observed, covering the entire surface. This organization of the morphology was related to the reduction in the average particle size (0.49 µm), approximately 10 times smaller than the coating containing only Sn (Figure 2a).

Azpeitia *et al.*[33] found a similar morphology for Sn electrodeposition in 1ChCl:2U on a copper substrate at 343 K, applying a potential of –0.75 V. The atom percentages of Sn and Sb in each electrodeposited coating are displayed in Table 2. From this table, it can be observed that increasing the concentration of Sb^{3+} species in the plating solution composition led to an increase in the Sb content in the coating and that the ratio between the Sb and Sn content in the coatings is higher than this ratio in the plating solution, indicating that under the used operational conditions, the electrodeposition of $Sn_xSb_{(1-x)}$ is classified as normal, based on the comparative analysis of the ratio Sn^{2+}/Sb^{3+} in the bath and Sn/Sb in the electrodeposited layer.

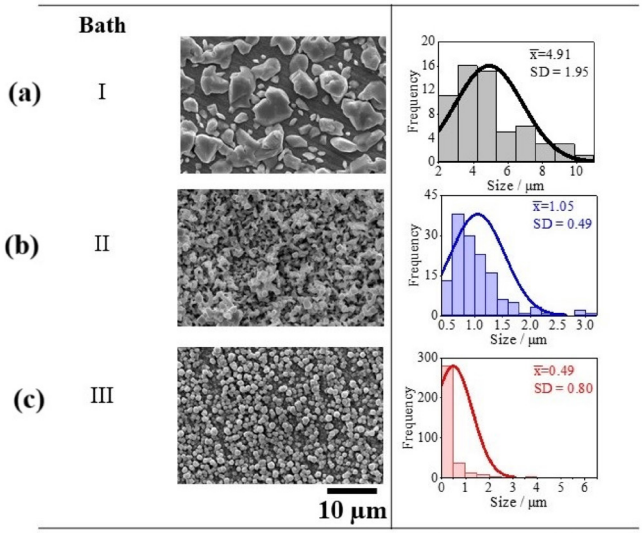

Figure 2. *SEM micrographs electrodeposit of Sn (a), $Sn_{77}Sb_{23}$ (b) and $Sn_{37}Sb_{63}$ (c) onto Cu electrode –0.55 V at 353 K. Histograms of the particle size of coatings*

Table 2. Chemical composition of electrodeposited coatings from EDS results and samples labelling

Bath	Film composition by EDS		Film
	Sn / at.%	Sb / at.%	
I	100	-	Sn
II	77	23	$Sn_{77}Sb_{23}$
III	37	63	$Sn_{37}Sb_{63}$

X-ray diffraction analyses were performed to investigate the effect of electrolytic bath composition on the crystal structure of $Sn_xSb_{(1-x)}$ coatings. Figure 3 shows the XRD patterns for the electrodeposits of Sn, $Sn_{77}Sb_{23}$ and $Sn_{37}Sb_{63}$ obtained on the Cu surface from baths I, II and III, applying a potential of –0.55 V at 353 K. In all diffractograms in Figure 3, the peaks corresponding to the Cu substrate are indexed at 2θ = 43.2, 50.4, 74.0 and 89.9° with a crystal structure cubic (space group Fm-3m, 225, ICDD 00-003-1005). For the diffractograms in Figures 3a-3b, a pure Sn phase is indexed at 2θ = 30.6, 31.9, 43.8, 44.8, 55.3, 62.5, 63.7, 64.5, 73.1 and 79.4°, referring to planes (200), (101), (220), (211), (301), (112), (400), (321), (411) and (312), respectively, with a tetragonal crystal system (space group I41/and, 141, ICDD 03-065-0296). In addition, a diffraction peak of the intermetallic phase Cu_6Sn_5 with a monoclinic crystal structure (space group C2/c, 15, ICDD 00-045-1488) is indexed for the diffractograms of Figures 3a-3b. The pure Sn and intermetallic Cu_6Sn_5 phases were also reported by Zhao *et al.*[34]

Additionally, for diffractograms of Figures 3b-3c, it was observed that the presence of Sb^{3+} in the electrolytic baths II and III favored the formation of the SnSb alloy, evidenced by the pure phase SbSn, with a rhombohedral crystal system (space group R-3m, 166, ICDD 00-033-0118).[35] Finally, for the diffractogram of Figure 3c, phases referring to the intermetallic Cu_2Sb and $Cu_6(Sn, Sb)_5$ were indexed, with tetragonal crystal structure (space group P4/nmm, 129, ICDD 01-087-1176) and hexagonal crystal system (space group P63/mmc E, 194, ICDD 00-49-1055), for Cu_2Sb and $Cu_6(Sn, Sb)_5$, respectively. The formation of these CuSn and CuSb intermetallic phases is attributed to the metallic bonding between the Cu atom on the surface of the Cu electrode and the first SnSb electrodeposited layer on the Cu surface. Considering the different

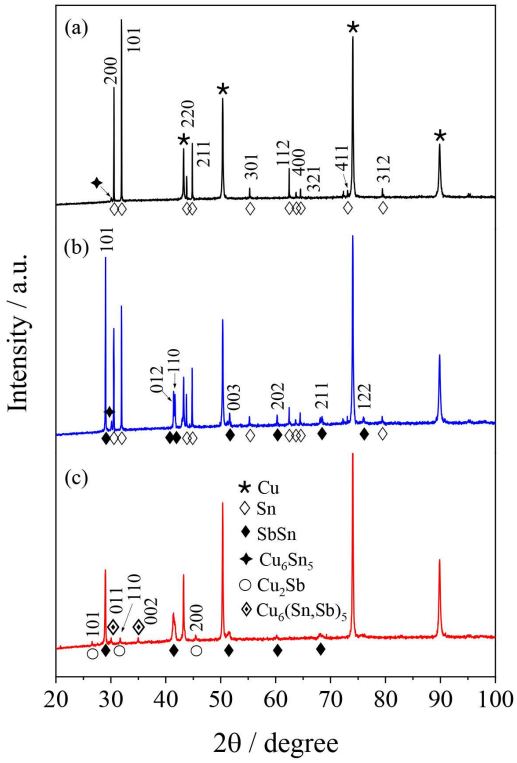

Figure 3. *Diffraction patterns electrodeposit of Sn (a), $Sn_{77}Sb_{23}$ (b) and $Sn_{37}Sb_{63}$ (c) onto Cu electrode –0.55 V at 353 K*

phases and morphologies obtained in the coatings, a test was carried out to evaluate the applicability of the coatings for corrosion.

Electrochemical corrosion tests

Potentiodynamic polarization (PP)

The potentiodynamic polarization curves obtained for the $Sn_xSb_{(1-x)}$ coatings in 0.1 mol dm^{-3} NaCl are shown in Figure 4. Initially, it can be noted that the corrosion potential (E_{corr}) of the $Sn_xSb_{(1-x)}$ alloys slightly shift towards more positive values compared to the Sn coating and with the Sb content in the electrodeposit. This behavior is attributed to Sb being a nobler metal than Sn. However, the E_{corr} values for Sn and $Sn_{77}Sb_{23}$, shown in Table 3, were statistically similar, considering the standard deviation at a 95% confidence level. For the cathodic branches, the achieved current densities are

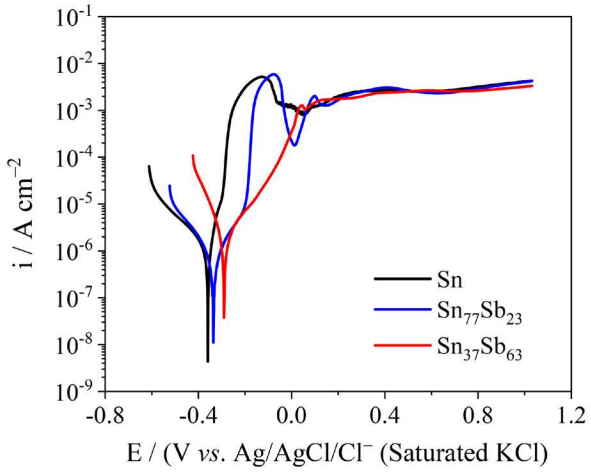

Figure 4. *The potentiodynamic polarization curves of different coatings in 0.1 mol dm^{-3} NaCl at 298 K and 0.5 mV s^{-1}*

Table 3. Electrochemical parameters for coatings Sn, $Sn_{77}Sb_{23}$ and $Sn_{37}Sb_{63}$ in 0.1 mol dm^{-3} NaCl obtained for Figure 4

Sample	$-E_{corr}$ / mV	R_p / (kΩ cm^2)
Sn	347 ± 55	4.60 ± 0.24
$Sn_{77}Sb_{23}$	348 ± 41	14.69 ± 0.82
$Sn_{37}Sb_{63}$	299 ± 70	1.81 ± 0.31

R_p: polarization resistance; E_{corr}: corrosion potential.

related to the oxygen reduction reaction (ORR), which is the cathodic reaction of the corrosion process in a neutral medium. For the anodic branches, it can be noted that the PP anodic curves obtained for the Sn and $Sn_xSb_{(1-x)}$ alloys are similar and characterized by two potential regions. The first region is related to the current increase with applied potential until it reaches a maximum current, attributed to the active dissolution of both electrodeposited coatings. In contrast, the second region is evidenced by the current plateaus, which are associated with the formation of tin oxides (SnO or SnO_2)[36-38] and antimony oxides (Sb_2O_3 or Sb_2O_4) on the electrodeposited $Sn_xSb_{(1-x)}$ coatings. These oxides can act as a physical barrier against the corrosion of both coatings. These results are in close agreement with those reported by Dias *et al.*,[36] who investigated the corrosion behavior of SnSb solder alloys, varying the Sb content between 2 and 10 wt.%.

The corrosion resistance of the investigated samples was evaluated by the polarization resistance (R_p) derived from the PP curves since the corrosion rate of a sample decreases with the increase of the R_p values. The R_p values were calculated from the fitted slope of the PP curves in the region of the E_{corr} (± 10 mV), as shown in Figure 1S (Supplementary Material). The obtained R_p values are also displayed in Table 3. For $Sn_xSb_{(1-x)}$ samples, a three-fold increase and a two-and-a-half-fold decrease in the obtained R_p values were observed for $Sn_{77}Sb_{23}$ and $Sn_{37}Sb_{63}$, respectively, compared to the Sn coating. Therefore, the R_p values indicate that the $Sn_{77}Sb_{23}$ sample is the most corrosion-resistant among the tested samples.

Figure 5 shows the SEM images and diffractograms for the Sn, $Sn_{23}Sb_{77}$, and $Sn_{37}Sb_{63}$ coatings after 24 and 48 h of immersion.

Analyzing these SEM images obtained for Sn after 24 and 48 h in 0.1 mol dm^{-3} NaCl solution (Figures 5a and 5d, respectively), it is observed that there is a reduction in the number of grains observed at 48 h, compared to 24 h, where it was possible to observe vacancies in the coating for the longest exposure time. For the SEM images of $Sn_{77}Sb_{23}$ coatings (Figures 5b and 5e), no significant modification was observed on the surface of this sample. The $Sn_{37}Sb_{63}$ coatings (Figures 5c and 5f) presented a dendritic morphology resembling pine trees[32,37,38] with size of approximately 0.022 µm for 24 h and 0.19 µm for 48 h, demonstrated in Figure 2S (Supplementary Material).

The analysis of XRD data achieved for the $Sn_xSb_{(1-x)}$ samples immersed in 0.1 mol dm^{-3} NaCl solution for 24 h, allowed the identification of five distinct crystalline phases: Cu, Sn, SnO, SbSn and Sb_2O_4. Characteristic peaks of the SnSb phase are also observed in the corresponding X-ray diffractograms of both $Sn_{23}Sb_{77}$ and $Sn_{37}Sb_{63}$ samples after 24 h of immersion. Considering 48 h of immersion, the analysis of XRD data allowed for the identification of four distinct crystalline phases: Cu, CuSn, SnO_2 and SnSb. Characteristic peaks of the SnSb phase were observed in both $Sn_{23}Sb_{77}$ and $Sn_{37}Sb_{63}$ materials for 48 h of immersion. Identifiable peaks related to the SnO phase were observed in both samples mentioned, and identifiable peaks related to the Sb_2O_4 phases were found only in the $Sn_{37}Sb_{63}$ material. Analyzing the SnSb polarization curves and the XRD analysis of the samples after immersion (Figures 4 and 5) showed that the formation of Sn and Sb oxides occurred in all coatings. For Sn and $Sn_{77}Sb_{23}$, the first level appeared due to the high Sn content. For the $Sn_{27}Sb_{63}$ coating, the first level referring to Sn did not appear because all the Sn present in the coating was used to combine with Sb. In this last league, Sb is in excess (63%).

For the coatings, Figure 4 shows at potential with values close to –0.1 V, a maximum current density, and stability in the current density values at 0.2 V. Polarization tests were conducted by applying the mentioned potential for 1 h to evaluate the influence of the potential applied to the Sn and SnSb coatings. Figure 6 shows the SEM images and diffractograms for the Sn, $Sn_{23}Sb_{77}$, and $Sn_{37}Sb_{63}$ coatings, obtained by polarizing the electrode for 1 h, at –0.1 and 0.2 V. At –0.1 V, Figures 6a-6c, the analysis of XRD data allowed for identifying five distinct crystalline phases: Cu, CuSn, SnO, SnO_2 and SnSb. Characteristic peaks of the SnSb phase were observed in the $Sn_{23}Sb_{77}$ and $Sn_{37}Sb_{63}$ coatings at –0.1 V, confirming the formation of the SnSb alloy. Identifiable peaks referring to the SnO phases were observed in the two samples mentioned. Figures 6d-6f shows the SEM images and diffractograms for the Sn, $Sn_{23}Sb_{77}$, and $Sn_{37}Sb_{63}$ coatings obtained by polarizing the coating at 0.2 V for 1 h. Therefore, the analysis of XRD data allowed for identifying eight distinct crystalline phases: Cu, Cu_2O, Cu_3Sn, SnO, SbSn, SnSb, Sb_2O_3 and SbO_2. Characteristic peaks of the SnSb phase were observed in the

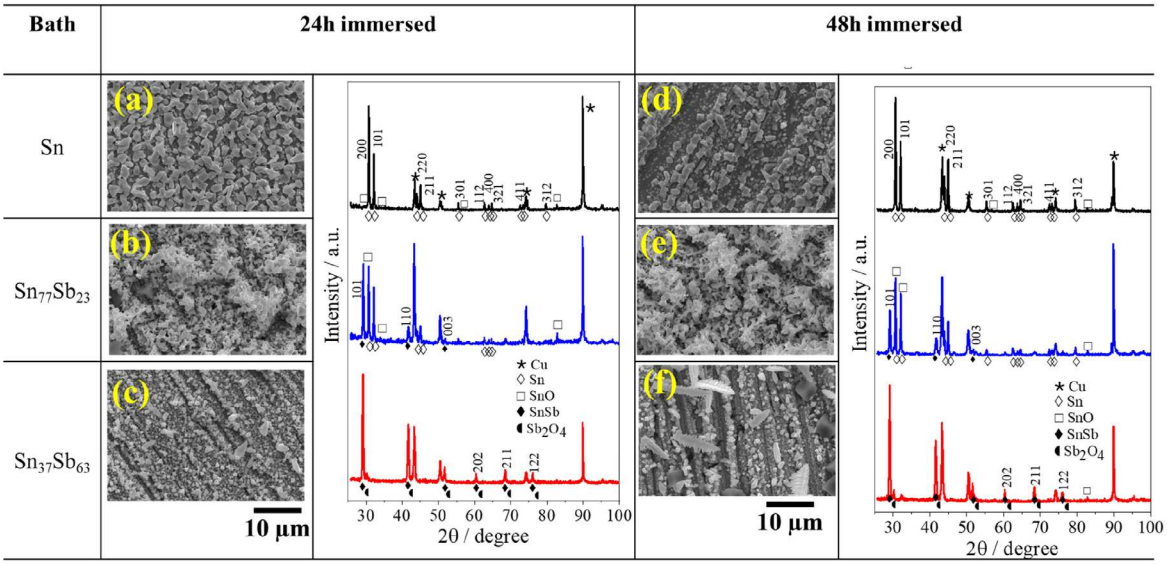

Figure 5. *SEM images and DRX results for Sn (a-d), $Sn_{77}Sb_{23}$ (b-e) and $Sn_{37}Sb_{63}$ (c-f) at different immersion times (24 and 48 h) in 0.1 mol dm^{-3} NaCl at 298 K*

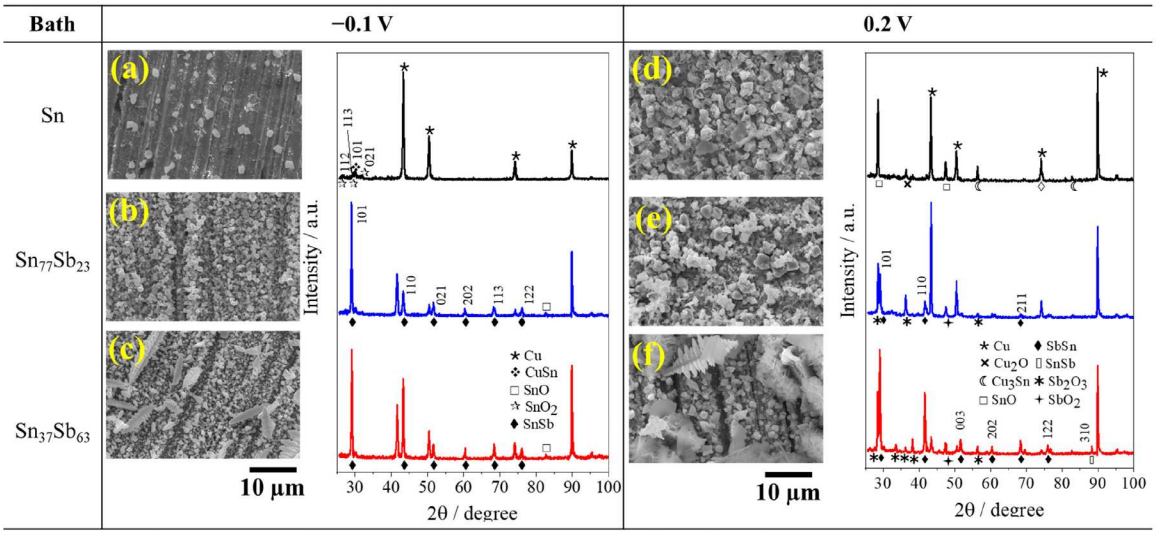

Figure 6. *SEM images and DRX results for Sn (a-d), $Sn_{77}Sb_{23}$ (b-e) and $Sn_{37}Sb_{63}$ (c-f) after 1 h at polarization on –0,1 V (a-c) and 0,2 V (d-f) in 0.1 mol dm^{-3} NaCl at 298 K*

$Sn_{23}Sb_{77}$ and $Sn_{37}Sb_{63}$ coatings. Identifiable peaks related to the SbO_2 and Sb_2O_3 phases were also detected. For the coatings containing only Sn (Figures 6a and 6d), it was observed that the negative potential ended up removing the grains observed in Figure 5. In contrast, at 0.2 V, a morphology like that obtained in Figure 5 was observed.

Electrochemical impedance spectroscopy (EIS)

EIS experimental data were collected for Sn, $Sn_{37}Sb_{63}$, and $Sn_{77}Sb_{23}$ coatings at 298 K in open circuit potential after 1 h of immersion in 0.1 mol dm^{-3} NaCl. Figure 7 presents the Nyquist diagrams obtained. The EIS diagrams were obtained at open circuit potential after 1 h of immersion of the samples in 1 mol L^{-1} NaCl. The potentials of –0.37, –0.30, and –0.24 V, determined by OCP after 1 h, were applied to Sn, $Sn_{77}Sb_{23}$, and $Sn_{37}Sb_{63}$ during the EIS experiment. The evolution of open circuit potential values with immersion time is shown in Figure 3S (Supplementary Information).

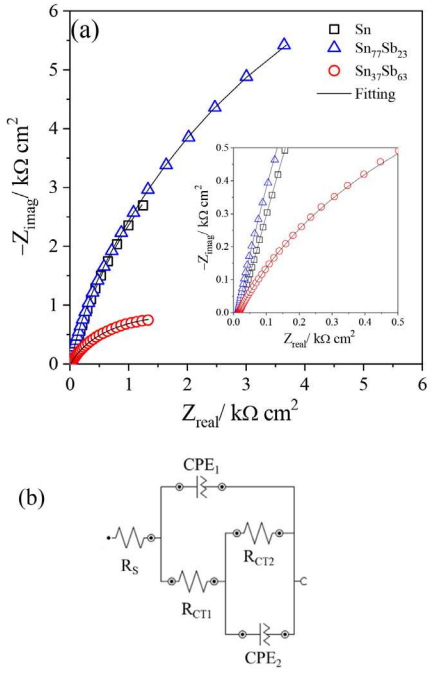

Figure 7. *(a) Nyquist diagrams of coatings in 0.1 mol dm^{-3} NaCl at 298 K and obtained after 1 h of immersion. Empty symbols indicate experimental results, and the lines indicate the fitting values using the EEC model. (b) Shows an example of better visualization at high frequencies. The EEC model was used to explain and fit the experimental EIS results*

Since the highest corrosion resistance is associated with the largest capacitive arc, the EIS data indicate that, among the tested samples, the one with the highest Sb content ($Sn_{37}Sb_{63}$) is more susceptible to corroding in a neutral medium and that the binary coating with a higher Sn content ($Sn_{77}Sb_{23}$) presents the greatest corrosion resistance. These data corroborate the R_p values displayed in Table 3.

The $Sn_{77}Sb_{23}$ coating was analyzed during 24 h of immersion in 0.1 mol dm^{-3} NaCl. The data corresponding to immersion times of 1, 2, 4, and 24 h are presented in Figure 8. Nyquist diagram profile showed no change from 4 to 24 h. A change in the impedance diagrams is observed for the first four hours, indicating an increase in susceptibility to corrosion of this coating in the first four hours. For immersion time between 4 and 24 h, no significant changes in the EIS diagrams are observed, suggesting that the corrosion resistance of the $Sn_{77}Sb_{23}$ reaches a constant value with the immersion time, which is attributed to the formation of SnO and Sb_2O_4 on the coating surface, acting as a barrier against the corrosion of the tested sample.

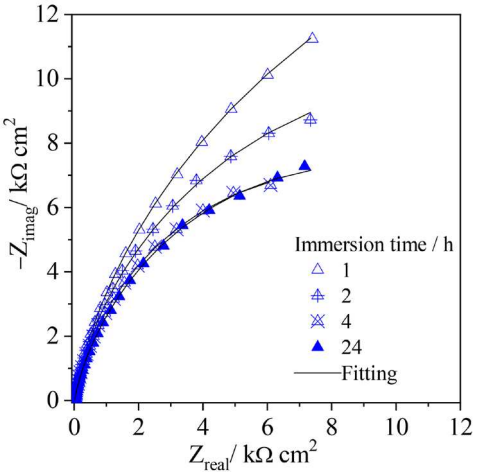

Figure 8. *Nyquist diagrams of $Sn_{77}Sb_{23}$ in 0.1 mol dm^{-3} NaCl at 298 K in different immersion times. Empty symbols indicate experimental results and filled symbols indicate the fitting values using the EEC model*

EIS data (Figure 4S, Supplementary Material) reveal the presence of two-time constants regardless of the analyzed coating. Analysis of the Nyquist diagrams shows capacitive time constants with elongated characteristics, indicating the overlap of two-time constants. A first-time constant is observed in the high to medium-frequency region, and the second-time constant is characterized in the low-frequency region (below 0.1 Hz). A similar result was reported by Dias *et al*.[36]

The X-ray diffraction (XRD) obtained after experiments in 0.1 mol dm^{-3} NaCl reveal the formation of oxides as corrosion products. This result allows for the association of the two-time constants with the oxides/electrolyte interface and the coating/oxides interface. The resistance and capacitance of the corrosion product layer are linked to the time constants in a high frequency region. The capacitance and resistance of the electrical double layer between the interface of corrosion products and coating are linked to the time constants in a low frequency region.

Taking into consideration the coating surface characteristics and the formation of oxides, the proposed model (Figure 7b) comprises the solution resistance, R_S, in series with two parallel elements: charge-transfer resistance (R_{CT}) and constant phase element (CPE). The first-time constant (R_{CT1}-CPE_1) couple corresponds to the oxides/electrolyte interface, while the second-time constant (R_{CT2}-CPE_2) couple, characterized in the low-frequency region, is associated with the coating/oxides interface. This configuration aligns with observations from other studies of Sn-based coatings in the literature.[39-41] The CPE is essential as it accounts for the distribution of relaxation times arising from physical, chemical, or geometrical inhomogeneity.[42,43]

Equation 4 describes the CPE impedance (Z_{CPE}), which is characterized by a non-ideal double-layer capacitance.

$$Z_{CPE} = \frac{1}{Y_o (j\omega)^{\alpha}} \quad (4)$$

where j is an imaginary number, ω is the angular frequency of sinusoidal perturbation, and Y_o is the capacity parameter that considers the combination of properties related to the surface and electrochemical species and proportional to the electroactive area.[40] The parameter α is the dimensionless non-linearity coefficient that ranges between 0 and 1. A value of 1 corresponds to an ideal capacitor, 0 corresponds to a resistor, and 0.5 can be associated with diffusion phenomena. Additionally, a value of −1, indicating inductive behavior.[44,45]

The quality of the fit was assessed using chi-squared values, which ranged of 10^{-4} to 10^{-5}. Considering fitting criteria such as the "number of model parameters" and "chi-square values",[39] the NOVA software version 2.1.5 was utilized to develop the electric equivalent circuit (EEC) model and determine the values of its components, resulting in a very good approximation to the experimental data. EEC parameter values obtained by modeling the experimental data of Sn, $Sn_{37}Sb_{63}$, and $Sn_{77}Sb_{23}$ coatings after 1 h of immersion are presented in Table 4. EEC parameter values for the $Sn_{77}Sb_{23}$ coating, analyzed for 24 h of immersion, are presented in Figure 8.

Figure 9 illustrates a decrease in R_{CT2} with increasing immersion time. This trend may be attributed to the release of Sn^{2+} ions into the solution, which reduces the corrosion resistance of the coating. A slight increase in R_{CT1} value accompanies this decline in resistance. The action of the chloride ion results, to some extent, in the dissolution of the passivation film of the coating. Concurrently the passivation film is repaired due to the corrosive processes of the coating. This behavior corroborates the values of the first-time constant (R_{CT1}-CPE_1) couple, as they exhibited little variation with immersion time. For SnSb electrodeposited alloys (Figures 2b and 2c), the SEM images reveal that the electrodeposited coating is granular, and it is possible to observe the occurrence of smaller hexagonal and circular grains in the presence of Sb, making the coatings more homogeneous and with a larger surface area.

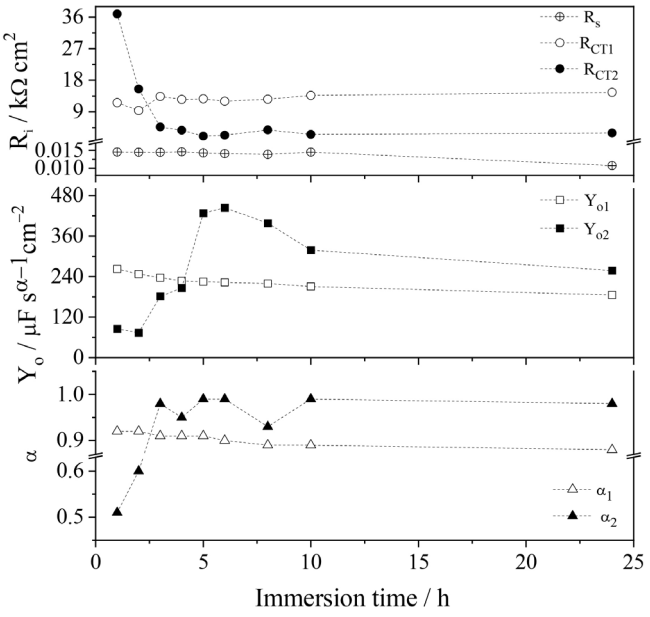

Figure 9. *Relationship between parameters obtained from the EIS result of $Sn_{77}Sb_{23}$ in 0.1 mol dm^{-3} NaCl at 298 K across different immersion times*

This result aligns with the capacity parameter (Y_o) observed in the $Sn_{37}Sb_{63}$ and $Sn_{77}Sb_{23}$ coatings, as they exhibited higher values. The α values obtained for the $Sn_{37}Sb_{63}$ and $Sn_{77}Sb_{23}$ coatings after 1 h of immersion in 0.1 mol dm^{-3} NaCl support diffusion phenomena, with values close to 0.5. The diffusion phenomena observed at low frequencies suggest rapid coating corrosion, likely due to the inadequate formation of an efficient protective film. R_{CT2} values for the Sn and $Sn_{77}Sb_{23}$ coatings were 12.6 and 10.4 kΩ cm^2, respectively, while the $Sn_{37}Sb_{63}$ coating exhibited the lowest value at 2.7 kΩ cm^2. Consistent with the polarization curves, the results obtained from EIS suggest a correlation between corrosion resistance and the percentage of Sn, indicating an increase in corrosion resistance with higher Sn content.

The XRD data reveals a single Sn matrix, with Sb appearing in intermetallic forms such as SnSb dispersed within the Sn matrix. The proportion of intermetallics increases with Sb content, potentially forming multiple galvanic couples that can affect the resulting corrosion resistance.[36,46,47]

Table 4. Parameters obtained by fitting the experimental result of the EIS on the different coatings using the EEC model

Coating	R_S / (Ω cm^2)	R_{CT1} / (kΩ cm^2)	Y_{o1} / (μF $s^{(\alpha-1)}$ cm^{-2})	α_1	R_{CT2} / (kΩ cm^2)	Y_{o2} / (μF $s^{(\alpha-1)}$ cm^{-2})	α_2
Sn	16	1.15	55.2	0.85	12.5	1.32	0.95
$Sn_{77}Sb_{23}$	14	10.5	538.9	0.88	7.43	422.2	0.85
$Sn_{37}Sb_{63}$	26	1.46	2744.4	0.71	2.7	515.0	0.45

R_S: solution resistance; R_{CT}: charge-transfer resistance; Y_o: capacity parameter; α: dimensionless non-linearity coefficient.

The formation of Sn-based oxides and hydroxides has been extensively reviewed in the literature. Kapusta and Hackerman[48] elucidate the pathways leading to the formation of $Sn(OH)_2$ and SnO, corresponding to Equations 5 and 6, respectively. The redox potentials of these half-reactions exhibit proximate values and are contingent upon pH variations.[49]

$$Sn_{(s)} + 2OH^-_{(aq)} \rightleftharpoons Sn(OH)_{2(s)} \quad (5)$$

$$Sn_{(s)} + 2OH^-_{(aq)} \rightleftharpoons SnO_{(s)} + H_2O_{(l)} + 2e^- \quad (6)$$

Since $Sn(OH)_2$ can be considered as an H_2O-containing SnO. Dehydration of $Sn(OH)_2$ can indeed result in the production of SnO, as indicated by Equation 7.[36,39] This transformation occurs specifically when the Sn-based surface is exposed to a dry atmosphere.[50] However, the experimental conditions in the present study do not involve a dry atmosphere. The formation of SnO, validated by the XRD spectrum presented in Figure 5, is attributed to reaction 7.

$$Sn(OH)_{2(s)} \rightarrow SnO_{(s)} + H_2O_{(l)} \quad (7)$$

The literature suggests the formation of $Sn(OH)_4$ and SnO_2 according to Equations 8 and 9, respectively.[36,39-42] However, these compounds were not observed in the XRD spectrum provided in Figure 5. Kapusta and Hackerman[48] indicate that these reactions exhibit slow kinetics, and an increase in the anodic potential may promote the formation of these compounds.

$$SnO_{(s)} + 2OH^-_{(aq)} \rightleftharpoons Sn(OH)_{4(s)} + 2e^- \quad (8)$$

$$Sn(OH)_{4(s)} + 2OH^-_{(aq)} \rightarrow SnO_{2(s)} + 2H_2O_{(l)} \quad (9)$$

The experimental investigation conducted in 0.1 mol dm^{-3} NaCl was performed under open circuit potential conditions. The absence of $Sn(OH)_4$ and SnO_2 as corrosion products on the $Sn_{77}Sb_{23}$ coatings can be attributed to this specific experimental setup.

CONCLUSIONS

SEM and EDS analyses demonstrated that the morphology of the electrodeposits exhibited a uniform distribution of dendritic clusters, and the occurrence of grains with different sizes was evident with increasing Sb content (63%). Characterization by XRD revealed the presence of crystalline phases of Sn, Sb, SbSn and intermetallic phases Cu_2Sb, Cu_6Sn_5 and $Cu_6(Sn,Sb)_5$. Polarization tests in 0.1 mol L^{-1} NaCl medium determined R_p values equal to 4597, 14692 and 1805 kΩ cm^2. Immersion tests were carried out for 24 and 48 h, and it was observed that the morphology of $Sn_{77}Sb_{23}$ did not change with the immersion time. XRD analyses for the coatings showed the presence of SnO, SnSb and Sb_2O_4 for both immersion times. When polarizing the coatings in NaCl for 1 h, SnO_2, SnSb and SnO phases were observed for –0.1 V and SnO, Cu_2O, Sb_2O_3, SnSb, Sb_2O_3 for 0.2 V. By EIS, the R_{CT1} values for the Sn, $Sn_{77}Sb_{23}$ and $Sn_{37}Sb_{63}$ coatings were 1.15; 10.5 and 1.46 kΩ cm^2, respectively. R_{CT2} values were 12.5; 7.43 and 2.7 kΩ cm^2. Consistent with the R_p values, the results suggested a correlation between corrosion resistance and the percentage of Sb, indicating increased corrosion resistance for $Sn_{77}Sb_{23}$.

SUPPLEMENTARY MATERIAL

Complementary material for this work is available at http://quimicanova.sbq.org.br/, as a PDF file, with free access.

ACKNOWLEDGMENTS

This study was financed in part by Coordenação de Aperfeiçoamento de Pessoal de Nível Superior - Brasil (CAPES), Conselho Nacional de Desenvolvimento Científico e Tecnológico (CNPq) and Fundação Cearense de Apoio ao Desenvolvimento Científico e Tecnológica (FUNCAP). A. N. C. gratefully acknowledges the funding provided by CNPq (proc. 305103/2022-9). P. L. N. thanks the financial support received from CNPq (proc. 302825/2022-3). N. G. S. thanks CNPq (proc. 141171/2021-9). A. A. C. A. thanks CAPES for her grants. The authors thank the Central Analítica-UFC/CT-INFRA/MCTI-SISANO/Pró-Equipamentos CAPES and Laboratório de Raios-X (UFC) for their support.

REFERENCES

1. Wang, R. Y.; Yuan, Z. F.; Zhao, H. X.; Yang, X.; Hao, Y. H.; *Trans. Nonferrous Met. Soc. China* **2023**, *33*, 1839. [Crossref]
2. Wang, X.; Zhang, L.; Li, M. L.; *J. Mater. Sci.: Mater. Electron.* **2022**, *33*, 2259. [Crossref]
3. Lakshmi, D.; Jayapandi, S.; Nalini, B.; Selvin, P. C.; *Semicond. Sci. Technol.* **2020**, *35*, 045008. [Crossref]
4. Huang, H. H.; Fan, X.; Singh, D. J.; Zheng, W. T.; *J. Mater. Chem. C* **2019**, *7*, 10652. [Crossref]
5. Schneider, M.; Langklotz, U.; Körsten, O.; Gierth, U.; *Mater. Corros.* **2023**, *74*, 920. [Crossref]
6. Lucas, F. W. S.; Lima, F. H. B.; *ChemElectroChem* **2020**, *7*, 3733. [Crossref]
7. Gamburg, Y. D.; Zangari, G.; *Theory and Practice of Metal Electrodeposition*, 1st ed.; Springer: New York, 2011.
8. Li, A.; Bai, X.; Xie, Y.; Xia, P.; Bao, H.; He, M.; Zeng, X.; Yang, W.; Li, X.; *Chemosphere* **2023**, *336*, 139097. [Crossref]
9. He, Z.; Yu, C.; Liu, J.; Miao, Z.; Wang, Y.; *Coatings* **2023**, *13*, 866. [Crossref]
10. Liu, S.; Ma, L.; Zhen, C.; Li, D.; Wang, Y.; Jia, Q.; Guo, F.; *Appl. Energy* **2023**, *352*, 121997. [Crossref]
11. Schulze, M. C.; Belson, R. M.; Kraynak, L. A.; Prieto, A. L.; *Energy Storage Materials* **2020**, *25*, 572. [Crossref]
12. Han, C.; Liu, Q.; Ivey, D. G.; *Electrochim. Acta* **2008**, *53*, 8332. [Crossref]
13. Huang, F. F.; Huang, M. L.; *J. Electrochem. Soc.* **2018**, *165*, D152. [Crossref]
14. Hashimoto, H.; Nishimura, T.; Umetsu, Y.; *Mater. Trans.* **2003**, *44*, 1624. [Crossref]
15. Smith, E. L.; Abbott, A. P.; Ryder, K. S.; *Chem. Rev.* **2014**, *114*, 11060. [Crossref]
16. Endres, F.; Abbott, A.; Macfarlane, D. R.; *Electrodeposition from Ionic Liquids*, 2nd ed.; John Wiley & Sons: New Jersey, 2017.
17. Chu, Q.; Wu, A.; Tan, T.; Guo, H.; Xiong, P.; Huang, S.; He, Y.; *Appl. Surf. Sci.* **2021**, *550*, 149322. [Crossref]
18. Abbott, A. P.; *Curr. Opin. Green Sustainable Chem.* **2022**, *36*, 100649. [Crossref]
19. Brandão, A. T. S. C.; Anicai, L.; Lazar, O. A.; Rosoiu, S.; Pantazi, A.; Costa, R.; Enachescu, M.; Pereira, C. M.; Silva, A. F.; *Coatings* **2019**, *9*, 798. [Crossref]
20. Gao, Y.; Hu, W.; Gao, X.; Duan, B.; *Surf. Eng.* **2014**, *30*, 59. [Crossref]
21. Anicai, L.; Petica, A.; Costovici, S.; Moise, C.; Brincoveanu, O.; Visan, T.; *Coatings* **2019**, *9*, 800. [Crossref]
22. Su, Z.; Xu, C.; Hua, Y.; Li, J.; Ru, J.; Wang, M.; Xiong, L.; Zhang, Y.; *Int. J. Electrochem. Sci.* **2016**, *5*, 3325. [Crossref]
23. Ma, J.; Prieto, A. L.; *Chem. Commun. (London)* **2019**, *55*, 6938. [Crossref]

24. Abtew, M.; Selvaduray, G.; *Materials Science and Engineering: R: Reports* **2000**, *27*, 95. [Crossref]
25. Cheng, S.; Huang, C. M.; Pecht, M.; *Microelectron. Reliab.* **2017**, *75*, 77. [Crossref]
26. Rasband, W.; *ImageJ*, version 0.4.0; National Institutes of Health, USA, 2021.
27. *HighScore Plus*, version 5.2; PANalytical B.V., Almelo, Netherlands, 2021.
28. Vieira, L.; Schennach, R.; Gollas, B.; *Electrochim. Acta* **2016**, *197*, 344. [Crossref]
29. Rosoiu, P. S.; Costovici, S.; Moise, C.; Petica, A.; Anicai, L.; Visan, T.; Enachescu, M.; *Electrochim. Acta* **2021**, *398*, 139339. [Crossref]
30. Sousa, N. G.; Oliveira, R. V.; Alcanfor, A. A. C.; Feitosa, F. X.; de Sant'Ana, H. B.; Schwarzacher, W.; de Lima Neto, P.; Monteiro, N. K. V.; Correia, A. N.; *J. Mol. Liq.* **2024**, *390*, 122973. [Crossref]
31. Anicai, L.; Petica, A.; Costovici, S.; Prioteasa, P.; Visan, T.; *Electrochim. Acta* **2013**, *114*, 868. [Crossref]
32. Alcanfor, A. A. C.; da Silva, L. P.; de Oliveira, R. C.; Paulo, G. A.; Sousa, C. P.; Campos, O. S.; Dias, D. F.; Feitosa F. X.; de Sant'Ana, H. B.; Monteiro, N. K.V.; Correia, A. N.; de Lima Neto, P.; *J. Mol. Liq.* **2024**, *399*, 124416. [Crossref]
33. Azpeitia, L. A.; Gervasi, C. A.; Bolzán, A. E.; *J. Electroanal. Chem.* **2023**, *944*, 117637. [Crossref]
34. Zhao, J.; Sun, K.; Liang, G.; Xu, C.; Zhao, J.; Xue, F.; Zhou, J.; *J. Mater. Res. Technol.* **2021**, *15*, 6726. [Crossref]
35. Park, M. S.; Needham, S. A.; Wang, G. X.; Kang, Y. M.; Park, J. S.; Dou, S. X.; Liu, H. K.; *Chem. Mater.* **2007**, *19*, 2406. [Crossref]
36. Dias, M.; Verissimo, N. C.; Regone, N. N.; Freitas, E. S.; Cheung, N.; Garcia, A.; *Corros. Eng., Sci. Technol.* **2021**, *56*, 11. [Crossref]
37. Shen, H. M.; Han, X. Y.; Zheng, X. M.; Muniyandi, B.; Wang, J. K.; Kang, Q. L.; Chen, M. G.; Wu, Q.; Zhang, P. Y.; *Electrochim. Acta* **2023**, *438*, 141529. [Crossref]
38. Bu, J.; Ru, J.; Wang, Z.; Hua, Y.; Xu, C.; Zhang, Y.; Wang, Y.; *Adv. Powder Technol.* **2019**, *30*, 2859. [Crossref]
39. Liu, J.; Park, S.; Nagao, S.; Nogi, M.; Koga, H.; Ma, J.; Zhang, G.; Suganuma, K.; *Corros. Sci.* **2015**, *92*, 263. [Crossref]
40. Liao, B.; Cen, H.; Chen, Z.; Guo, X.; *Corros. Sci.* **2018**, *143*, 347. [Crossref]
41. Jaiswal, D.; Kumar, S.; Behera, C. K.; *Mater. Today Commun.* **2022**, *33*, 104627. [Crossref]
42. Łosiewicz, B.; Budniok, A.; Rówiński, E.; Łągiewka, E.; Lasia, A.; *Int. J. Hydrogen Energy* **2004**, *29*, 145. [Crossref]
43. Kramer, M.; Tomkiewicz, M.; *J. Electrochem. Soc.* **1984**, *131*, 1283. [Crossref]
44. Huković, M. M.; Babić, R.; *Corros. Sci.* **2007**, *49*, 3570. [Crossref]
45. Burashnikova, M. M.; Kazarinov, I. A.; Zotova, I. V.; *J. Power Sources* **2012**, *207*, 19. [Crossref]
46. Yan, Q.; Zhang, H.; Man, C.; Pang, K.; Wang, X.; Cui, Z.; Cui, H.; *J. Mater. Eng. Perform.* **2023**, *33*, 11494. [Crossref]
47. Zhang, Q.; Li, Q.; Chen, X.; *RSC Adv.* **2021**, *11*, 1332. [Crossref]
48. Kapusta, S. D.; Hackerman, N.; *Electrochim. Acta* **1980**, *25*, 1625. [Crossref]
49. Pourbaix, M.; *Atlas of Electrochemical in Aqueous Solutions*, 1st ed.; National Association of Corrosion Engineers: Ann Arbor, 1974.
50. Yan, Z.; Xian, A. Ping.; *Metall. Mater. Trans. A* **2013**, *44*, 1462. [Crossref]

ANEXO B – MANUSCRITO 2

Journal of Molecular Liquids 399 (2024) 124416

Contents lists available at ScienceDirect

Journal of Molecular Liquids

journal homepage: www.elsevier.com/locate/molliq

On the role of water in antimony electrodeposition from choline chloride/ethylene glycol/water mixture

Ana Aline C. Alcanfor [a], Leonardo P. da Silva [a], Raíssa C. de Oliveira [a], Gabrielle A. Paulo [a], Camila P. Sousa [a], Othon S. Campos [b], Diego F. Dias [c], Filipe X. Feitosa [d], Hosiberto B. de Sant'Ana [d], Norberto K.V. Monteiro [a], Adriana N. Correia [a,*], Pedro de Lima-Neto [a]

[a] Departamento de Química Analítica e Físico-Química, Centro de Ciências, Universidade Federal do Ceará, Campus do Pici, 60440-900, Fortaleza, CE, Brazil
[b] Departamento de Química e Física, Centro de Ciências Exatas, Naturais e da Saúde, Universidade Federal do Espírito Santo, Campus de Alegre, 29500-000, Alegre, ES, Brazil
[c] Programa de Pós-Graduação em Física, Centro de Ciências, Universidade Federal do Ceará, Campus do Pici, 60440-900, Fortaleza, CE, Brazil
[d] Departamento de Engenharia Química, Centro de Tecnologia, Universidade Federal do Ceará, Campus do Pici, 60455-760, Fortaleza, CE, Brazil

ARTICLE INFO

Keywords:
Antimony electrodeposition
Deep eutectic solvent
Water content
DFT
QTAIM

ABSTRACT

Through experimental research and theoretical calculation, it was investigated the effect of water and temperature on the electrodeposition of antimony (Sb) on a platinum (Pt) electrode. The plating solutions were prepared by the addition of 0.05 mol L^{-1} $SbCl_3$ to the mixtures of choline chloride (ChCl), ethylene glycol (EG) and water (W) in the following molar ratio: 1ChCl:2EG (bath 1), 1ChCl:2EG:0.45 W (bath 2), and 1ChCl:2EG:1.62 W (bath 3). Furthermore, the Sb coatings were electrodeposited at 297 and 338 K. The surface morphologies and crystalline structures of Sb electrodeposits were analysed by scanning electron microscopy (SEM) and X-ray diffraction (XRD), respectively. In addition, to understand the interactions of Sb^{3+} species with the other components of the plating solution, models were created and calculated using density functional theory (DFT) and quantum theory of atoms in molecules (QTAIM). The results of the voltammetric behaviour of Sb^{3+} species indicated that the reduction potential was shifted towards more positive values with increasing water content on the electrolyte, indicating that the water catalyses the electrochemical reduction of the Sb^{3+} species. The values of the diffusion coefficients for the Sb^{3+} species were calculated by applying the Cottrell equation, which increased with the addition of water and temperature increment. The water content and temperature increase affect the surface morphologies of the Sb electrodeposited coatings, which is attributed to the improvement of Sb electrodeposition rate. Moreover, Sb electrodeposited coatings were successfully obtained without adding a complexing agent, indicating that the procedure adopted for the Sb electrodeposition is environmentally friendly. The XRD results revealed the pure phase Sb films. DFT simulations indicated that the Sb-Cl interaction is stronger, which suggests the formation of Sb-Cl complexes. Adding H_2O molecules favours the electron affinity of the systems, and QTAIM results suggested that this additive decreased the electron density of Sb^{3+} ions.

1. Introduction

Antimony (Sb) and Sb-based alloys are promising materials due to the wide range of applications in modern technologies, such as semiconductors [1], thermoelectric [2], electrocatalysts for the CO_2 reduction reaction [3], and recently, increased interest has been given to the development of anodic materials for rechargeable batteries, such as Li/Na-ion batteries [4,5]. In general, electrodeposition is one of the most employed methods to produce Sb coatings, and it stands out for being an effective technique to produce coatings on a large scale, with low cost and easy control of deposition parameters such as coating thickness and coating composition.

The Sb electrodeposition is reported in aqueous baths, either in acid electrolytes [6–10] as well in alkaline solutions [11,12]. However, one of the disadvantages that aqueous solutions can present is a restricted electrochemical potential range that can promote a competition on the

* Corresponding author.
E-mail address: adriana@ufc.br (A.N. Correia).

https://doi.org/10.1016/j.molliq.2024.124416
Received 21 September 2023; Received in revised form 17 February 2024; Accepted 6 March 2024
Available online 7 March 2024

surface of the working electrode between the hydrogen evolution reaction (HER) and the electrodeposition of chemical species of interest [13]. In addition, some metals require complexing agents in aqueous electroplating solutions to facilitate deposition, but some conventional complexing agents are not environmentally friendly, which can lead, in an industrial practice, to a non-suitable wastewater discharge.

Other electrolytes have been employed to overcome the cited disadvantages of aqueous solutions, such as the ionic liquids used for the electrodeposition of Sb and Sb alloys [14–17]. Among advantages, ionic liquids have a wide electrochemical range, good salt solubility and high conductivity. Additionally, the last two decades of the 21st Century saw the increasing use of deep eutectic solvents (DES) as a solvent for the formulation of electroplating solutions for electrodeposition of metals and alloys [18]. In general, DES can be obtained by mixing a quaternary ammonium salt with hydrogen bond donors in appropriate proportions. In addition to offering advantages to ionic liquids, DES are easy to prepare, biodegradable, non-toxic and environmentally friendly, which is very attractive for market prospects. Furthermore, the real potential of DES for the formulation of industrial commercial plating solutions has been evaluated by pilot projects in the Abbott Group [19]. These authors demonstrated that DES has the potential to become actual electrolytes for the industrial electroplating process, with emphasis on the electroplating of Ni, Fe and Zn.

The electrodeposition of Sb from DES based on choline chloride has been studied in mixtures with urea [20,21], oxalic acid [22] and ethylene glycol [23–28]. Additionally, the effect of adding water to DES has been investigated in recent years, especially in the electrodeposition of metals and metal alloys [29–31]. Some researchers have demonstrated that adding water promotes the electrodeposition process of the species of interest and a significant reduction of viscosity in the plating solution, thus producing improvements in electrodeposition processes [32–34]. Furthermore, computational modeling studies have helped to elucidate the influence of temperature and water addition on DES properties [35–37].

Although the electrodeposition of Sb in eutectic solvent medium has been studied, the effect of water addition to the medium has yet to be reported. Thus, this work focuses on studying the effect of water addition and the temperature increase on the electrodeposition of Sb from mixtures containing choline chloride and ethylene glycol in the absence and presence of water. In the theoretical approach, Molecular Dynamics (MD), Density Functional Theory (DFT) and Quantum Theory of Atoms in Molecules (QTAIM) were used to analyse the behaviour of the DES and $SbCl_3$ system with different amounts of H_2O molecules to verify the behaviour of the system without and with additive, analysing the results on the electronic affinity of all systems, in addition to the strength of the interactions, on the type of interactions (intramolecular or intermolecular) of Sb^{3+} ions.

2. Experimental

2.1. Chemicals and viscosity measurements

All chemicals were used without any further purification. The eutectic mixture was prepared by mixing choline chloride (ChCl, Sigma-Aldrich®, ≥99 %) and ethylene glycol (EG, Sigma-Aldrich®, ≥99.8 %) in a molar ratio of 1:2 (1ChCl:2EG) and heated at 353 K until the formation of a colourless liquid [38]. Then, a required amount of water, treated by the Milli-Q system (18.2 MΩ cm), was added to the 1ChCl:2EG to form solutions with a water molar ratio of 0.45 (1ChCl:2EG:0.45 W) and 1.62 (1ChCl:2EG:1.62 W). The plating solutions were prepared by the addition of 0.05 mol/L of anhydrous antimony (III) chloride ($SbCl_3$, Sigma-Aldrich®, ≥ 99 %) in each one of the prepared solvents: 1ChCl:2EG, 1ChCl:2EG:0.45 W and 1ChCl:2EG:1.62 W, to form the baths 1, 2, and 3, respectively. Finally, the viscosity (η) of the electroplating solutions was measured at 297 and 338 K temperatures using an Anton Paar® viscodensimeter model SVM-3000.

2.2. Electrochemical measurements

All electrochemical experiments were carried out using a conventional three-electrode electrochemical cell and carried out at 297 and 338 K. A potentiostat/galvanostat (Autolab PGSTAT30, Metrohm) controlled by NOVA software version 2.1.4 were used for the acquisition and analyses of the electrochemical data. Two Pt electrodes were used as a working electrode for the electrochemical experiments. The first was a disk electrode with a diameter of 0.5 mm (geometric surface area of 0.0019 cm^2), which was used in the cyclic voltammetry and chronoamperometry measurements. The second was a foil, with 0.5 cm^2 of geometric area, which was used to obtain the Sb electrodeposits under potentiostatic control. Before each electrochemical experiment, the working electrodes were sanded on SiC silicon carbide 600 grit sandpaper, washed with Milli-Q water (18.2 MΩ cm), and dried with airflow. The auxiliary electrode was a Pt plate, with 1.0 cm^2, and an $Ag_{(s)}/AgCl_{(s)}$ wire immersed in 1ChCl:2EG mixture was used as the reference electrode. Using 25 mV s^{-1} at 297 and 338 K, the cyclic voltammetry (CV) results were achieved between + 0.6 and –1.5 V to characterize the electrode surface in the choline chloride and ethylene glycol mixture in the absence and presence of water, while the electrochemical reduction of Sb^{3+} species was assessed by scanning the potential between + 0.4 and –0.6 V. Chronoamperometric measurements were made to achieve the diffusion coefficients (D) of the Sb^{3+} species using Cottrell's Equation. The current–time transient curves were obtained by applying 0.4 V for 10 s, followed by a jump to –1.0 V for 60 s.

Lastly, the Sb electrodeposits were obtained by applying the values of cathodic peak potentials derived from the cyclic voltammograms of the Sb^{3+} species in electrolytic solutions in the absence and presence of water, such as –0.35 V; –0.33 V and –0.30 V at 297 K, and –0.29 V; –0.27 V and –0.24 V at 338 K, for the baths 1, 2 and 3, respectively. Finally, the electrodeposition time was fixed in 1800 s, and Faraday's Equation was used to estimate the amount of Sb electrodeposited.

2.3. Morphological and structural characterization

The surface morphology of the Sb electrodeposits was characterized by a field-emission scanning electron microscope (FEG-SEM FEI-Quanta 450). X-ray diffraction (XRD) analyses were conducted using a PANalytical® diffractometer model X-Pert PRO with CoKα (λ = 1.789 Å) radiation, operating at 40 kV and 40 mA in the range 10° to 100°. The experimental data was treated using PANalytical® X'Pert HighScore Plus® software, and the crystalline phases presented in diffractograms were indexed in the crystallography PDF-22004 card files from the International Centre for Diffraction Data (ICDD).

2.4. Computational simulations

To describe the system without water, one molecule of $SbCl_3$, two molecules of EG and one molecule of ChCl were drawn. The number of water molecules (X = 3, 5, 10 and 15) was gradually added to describe the systems with water. To obtain the optimized geometries of the studied systems, the software XTB version 6.5.0 [39] was used, and molecular dynamics simulations were carried out, obtaining 2000 geometric structures (frames). Finally, the Molclus software version 1.9.9.7 [40] was used to rank the energy of the 2000 structures, and the system with the lowest energy was chosen for the geometries optimization at the DFT level. The DFT calculations were carried out in PBE-D3BJ/Def2-TZVP [39,41] and Def2/J auxiliary basis [42] in the ORCA 5.0.4 software [43,44]. The calculation of the vertical electron affinity energy (VEA) [45,46] in (Equation (1) was used to obtain a correlation between the addition of water and the susceptibility of the system to the reception of electrons, thus being associated with the reduction of antimony cation (Sb^{3+}) and addition of H_2O. Finally, the relative VEA was calculated (ΔVEA), where the reference value for energy is that of the system without water (Equation (2).

$$VEA = (G_{neutral}) - (G_{anion}) \quad (1)$$

$$\Delta VEA = (VEA_{SystemA}) - (VEA_{SystemXH_2O}) \quad (2)$$

In these equations, $G_{neutral}$ is the free energy of the uncharged system, G_{anion} is the free energy of the system after adding an electron; $VEA_{SystemA}$ is the electron affinity of the system without water, and $VEA_{SystemXH_2O}$ is the electron affinity of the system with·H_2O molecules.

Bader's "atoms in molecules" (AIM) theory, also referred to as the "quantum theory of atoms in molecules" (QTAIM), is utilized to analyse the electronic density [47]. The electron density gradient vector ($\nabla\rho$) is obtained by calculating the first derivative of ρ is 0 for potential effective electron density over all coordinates. A critical point (CP) is a point in space where each derivative of $\nabla\rho$ is zero ($\nabla\rho = 0$). The second derivatives of electron density are used to differentiate critical points from local minimums, local maximums, or saddle critical points. Four types of stable critical points exist, all having three non-zero eigenvalues. Two negative eigenvalues of the function's Hessian matrix characterize a second-order saddle point. The bond critical point (BCP), commonly found between attractive atomic pairs in electron density analysis, has a classification of (3,-1) [48]. The AIM data were obtained by the MULTIWFN 3.8 software [49] and visualized by the VMD software [50].

3. Results and discussion

3.1. Electrochemical studies

Initially, the cyclic voltammograms (CVs), shown in Fig. S1 (Supplementary Material), were achieved between + 0.6 and –1.5 V, at 25 mV s^{-1} and 297 K (Fig. S1 (a)) and at 338 K (Fig. S1 (b)) to evaluate the addition of water on the electrochemical range of the 1ChCl:2EG mixture. In these CVs, it can be noted that any electron transfer reaction is observed between + 0.6 and –0.8 V. For potentials more negative than –0.8 V, there is an increase in cathodic current density with the addition of water, which can be attributed to the reduction of hydroxyl groups of EG, choline ions (Ch^+) and water molecules [51]. An anodic process around –0.2 V is present for all scans towards more positive values. This process is attributed to the oxidation of water and groups of EG. Therefore, these results indicate that the water and the solvent molecules are simultaneously electrochemical reduced at potentials more negative than –0.8 V. Moreover, for applied potentials more negative than –0.8 V, the current density values, displayed in Fig. S1 (b), are higher than those shown in Fig. S1 (a), which means the electrochemical reduction rates of all chemical species increase with the temperature. These results agree with previously reported works investigating the electrochemical potential window onto Pt electrode on 1ChCl:2EG with water additions [30,31].

The effect of water addition on the electrochemical behaviour of Sb^{3+} species on the Pt electrode was investigated by the CVs shown in Fig. 1. The experiments were conducted at 25 mV s^{-1} between + 0.4 and –0.6 V, at 297 K (Fig. 1(a)) and 338 K (Fig. 1(b)).

According to the results of Fig. 1(a-b), it is observed that all direct scans (scanning towards more negative potentials) presented a cathodic peak (c1), which is attributed to the reduction of the Sb^{3+} to Sb. The peak potentials are located at − 0.35 (bath 1), −0.33 (bath 2), and − 0.30 V (bath 3) at 297 K and − 0.29 (bath 1), −0.27 (bath 2), and − 0.24 V (bath 3) at 338 K, respectively. These results indicate that the water addition in the plating solutions catalyses the electrochemical reduction of the Sb^{3+} species, because, for both temperatures and in all plating solutions, the Sb electrodeposition potential shifts towards more positive values with the increase in the water content in the plating solutions. Furthermore, with increasing the water content from 0 up to 1.62 M ratio, the peak reduction potential c1 of Sb^{3+} becomes less negative from − 0.35 to − 0.30 V at 297 K and from − 0.29 to − 0.24 V at 338 K. These results from Fig. 1(a-b) are listed in Table 1. Also, the cathodic peak current densities (i_{pc}) become increasingly pronounced with a further increase in water content in the electrolytic solution, which means that water improves the Sb electrodeposition rate.

Table 1
Effect of water addition on the voltammetric profiles during the reduction of Sb^{3+}/Sb on Pt electrode.

T / K	Water molar ratio in the plating solutions	E_{pc} / V	i_{pc} / mA cm^{-2}	η / mPa s
297	0.00	−0.35	−2.086	43.198
	0.45	−0.33	−2.438	32.841
	1.62	−0.30	−3.592	20.162
338	0.00	−0.29	−4.054	11.113
	0.45	−0.27	−5.717	8.9119
	1.62	−0.24	−7.108	5.9378

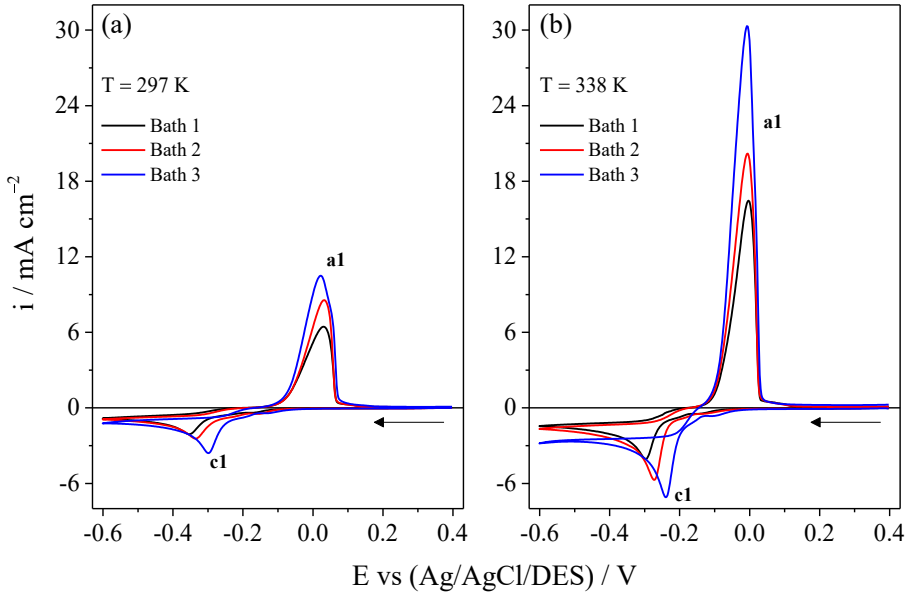

Fig. 1. Cyclic voltammograms obtained on Pt electrode in baths 1, 2 and 3 containing 0.05 mol L^{-1} $SbCl_3$ at 297 K (a) and 338 K (b). All cyclic voltammograms were obtained at 25 mV s^{-1}.

Moreover, Table 1 also displays the viscosity for all tested plating solutions at both working temperatures. It can be noted in this table that at each working temperature, the viscosity decreases with water addition, and consequently, this led to an increase in the plating solution conductivity with the increase of the water content. This fact was confirmed by the increase of the diffusion coefficient values of Sb^{3+} species (D) with the increase in the water content in each investigated temperature, which is displayed in Table 2. The D values were obtained from the experimental chronoamperometric curves, shown in Fig. S2. According to the values listed in Table 2, the D values obtained in this work increase with the addition of water, and the variation of 41 K promotes an increase of one order of magnitude in the D values. Moreover, the D values achieved in this work at 297 K are in the same order of magnitude as those D values published in the literature for eutectic solvents and ionic liquids. Besides that, for the electrolytic solution with the addition of water and at 338 K, the D values present the same order of magnitude as those reported in the literature for aqueous solutions. Therefore, there is a good agreement between the D values reported in this work and those already published in the literature. Thus, the changes in the D values with water content result in higher ionic mobility and, consequently, increase the electrochemical reduction rate of the Sb^{3+} species, which justifies the increase in the cathodic current density values.

For the reverse scan, an anodic peak (a1) is observed in all cyclic voltammograms obtained at 297 K and 338 K. The a1 peak is ascribed to the electrochemical oxidation process of Sb to Sb^{3+} [23,25]. In addition, despite the electrochemical behaviour of the Sb^{3+} species being similar in the absence and the presence of water, it can be noted that the a1 peak is larger than the c1 peak, and it increases more than the c1 peak as the water content increases. The explanation for the a1 peak being larger and higher than the c1 peak is related to the fact that the total amount of Sb electrodeposited on the Pt surface is the sum of the Sb mass electrodeposited in the direct scan with the Sn mass electrodeposited in the reverse scan between –0.6 V and the potential in which the electric current becomes zero. Additionally, the Sb electrodeposition efficiencies (ε_{ed}), which are shown in Table 3, were estimated by the ratio between the electric charge related to electrochemical dissolution of Sb coating (peak a1, Q_{ecd}) and electrodeposition charge (Q_{ec}), which was calculated taking into consideration the electric charge related to the electrochemical reduction of Sb^{3+} species to Sb in the direct scan summed with that related to the formation of Sb coating in the reverse scan. The Table 3 shows that the ε_{ed} values are higher, varying from 91 % up to 95 %. Furthermore, the ε_{ed} values increase with the temperature and water addition, and for each tested temperature, the ε_{ed} values improve with the addition of water, which is explained by the increment in the ionic mobility related to the rise in the water content. Therefore, all these results evidence that the addition of water catalyses the electrochemical reduction of the Sb^{3+} species to form the Sb electrodeposited coating. Lastly, these results are in close agreement with research previously reported in the literature about the influence of water content and temperature for deep eutectic solvent-based electrochemical systems [31,33,34,37].

Table 2
Comparison of diffusion coefficients of Sb^{3+} obtained in this investigation with those already reported in the literature for plating solutions based-formulated in DES, ionic liquids and in water.

Reference	D / $cm^2\ s^{-1}$	System	T / K
[9]	1.051×10^{-5}	H_2SO_4-NH_4F	298
[9]	2.120×10^{-5}	H_2SO_4-NH_4F	318
[50]	3.76×10^{-6}	Citrate Bath	293
[13]	5.27×10^{-6}	6 M HCl	318
[14]	2.98×10^{-7}	EMI–Cl–BF_4	303
[15]	6.07×10^{-7}	[EMIm]BF_4	298
[16]	1.23×10^{-7}	BMP-DCA	308
[51]	1.65×10^{-5}	LiCl–KCl molten salt	673
[52]	2×10^{-7}	1ChCl:2U	353
[26]	4.719×10^{-7}	1ChCl:2EG	333
[22]	8.86×10^{-7}	1ChCl:2EG	343
In this work	1.79×10^{-7}	1ChCl:2EG	297
In this work	3.13×10^{-7}	1ChCl:2EG:0.45 W	297
In this work	4.76×10^{-7}	1ChCl:2EG:1.62 W	297
In this work	1.01×10^{-6}	1ChCl:2EG	338
In this work	1.10×10^{-6}	1ChCl:2EG:0.45 W	338
In this work	1.29×10^{-6}	1ChCl:2EG:1.62 W	338

Table 3
Influences of water molar ratio and temperature on the electrodeposition efficiency of Sb from choline chloride/ethylene glycol/water mixture. The data listed in this table were derived from the cyclic voltammograms shown in Fig. 1.

T / K	Water malar ratio in the plating solutions	Q_{ecd} / C	Q_{ec} / C	ε_{ed} / %
297	0.00	0.061 ± 0.00141	0.067 ± 0.00152	91
	0.45	0.0735 ± 0.00212	0.0795 ± 0.00232	92
	1.62	0.101 ± 0.00283	0.107 ± 0.00354	94
338	0.00	0.120 ± 0.00111	0.130 ± 0.00121	92
	0.45	0.149 ± 0.00151	0.160 ± 0.00142	93
	1.62	0.167 ± 0.00212	0.175 ± 0.00283	95

It is known that the metal ions in DES can form complexes with chloride ions and ethylene glycol. For instance, Hartley et al. [52] investigated the speciation of 25 metal salts in four DES and five imidazolium-based ionic liquids using the EXAFS technique. The authors demonstrated that monovalent metal ions formed two complex species in solution $(MCl_2)^-$ and $(MCl_3)^{2-}$ complexes, while the divalent metal ions (M^{2+}) formed the $(MCl_4)^{2-}$ complexes. Furthermore, these authors also demonstrated that the addition of water did not affect the formation of these complexes. In addition, Oelkers et al. also used the EXAFS technique to identify the occurrence of Sb^{3+} species complexed with Cl^- ions in highly concentrated HCl solution from 25 up to 250 °C and at pressures corresponding to the liquid–vapor equilibrium curve for water [53]. These authors pointed out that the stability of the $SbCl_3$ $[SbCl_4]^-$, $[SbCl_6]^{3-}$ complexes increased with temperature. Besides that, the Potential - pH diagram of the Sb-H_2O system [54] shows that the $[Sb(OH)_6]^-$ and $HSbO_2$ are the soluble complex species at pH 7. Therefore, from this reports [54–56], it is suggested that the mechanism of the electrochemical deposition of Sb is associated with the presence of these Sb complex species in the 1ChCl:2EG:0.45 W and 1ChCl:2EG:1.62 W plating solutions.

3.2. Morphological and structural characteristics of Sb films

Fig. 2 shows the SEM images of the antimony electrodeposits at 297 K (Fig. 2(a-c)) and 338 K (Fig. 2(d-f)) in the baths 1, 2 and 3. For the Sb coating obtained at 297 K and without the addition of water, the surface morphology is uniform without the presence of agglomerates (Fig. 2(a)). For those obtained the in presence of water from baths 2 and 3 (Fig. 2(b) and 2(c)), a dendrite-like morphologies can be observed. Additionally, with increasing water content, dendritic structures predominate. In contrast, for all electrodeposits obtained at 338 K, a hierarchical structure in sheets is observed, as shown in Fig. 3(d-f). For greater clarity of the description of Sb sheets, it is given the magnification of the samples obtained at 338 K in the Fig. S3 (Supplementary Material). The change in the surface morphology of the Sb electrodeposited coatings change with temperature and water content is attributed to the fact that the rate of the mass transport of the Sb^{3+} species from the solution to the electrode surface becomes greater with the increases of the temperature and water content, leading to an improvement in the kinetics of the Sb electrodeposition. The Table 4 shows that the Q_{ec} and, consequently, the Sb electrodeposited masses (m_{ed}) are increasing with the increases of water content and temperature, which is experimental evidence that the kinetics of the Sb electrodeposition became greater when the

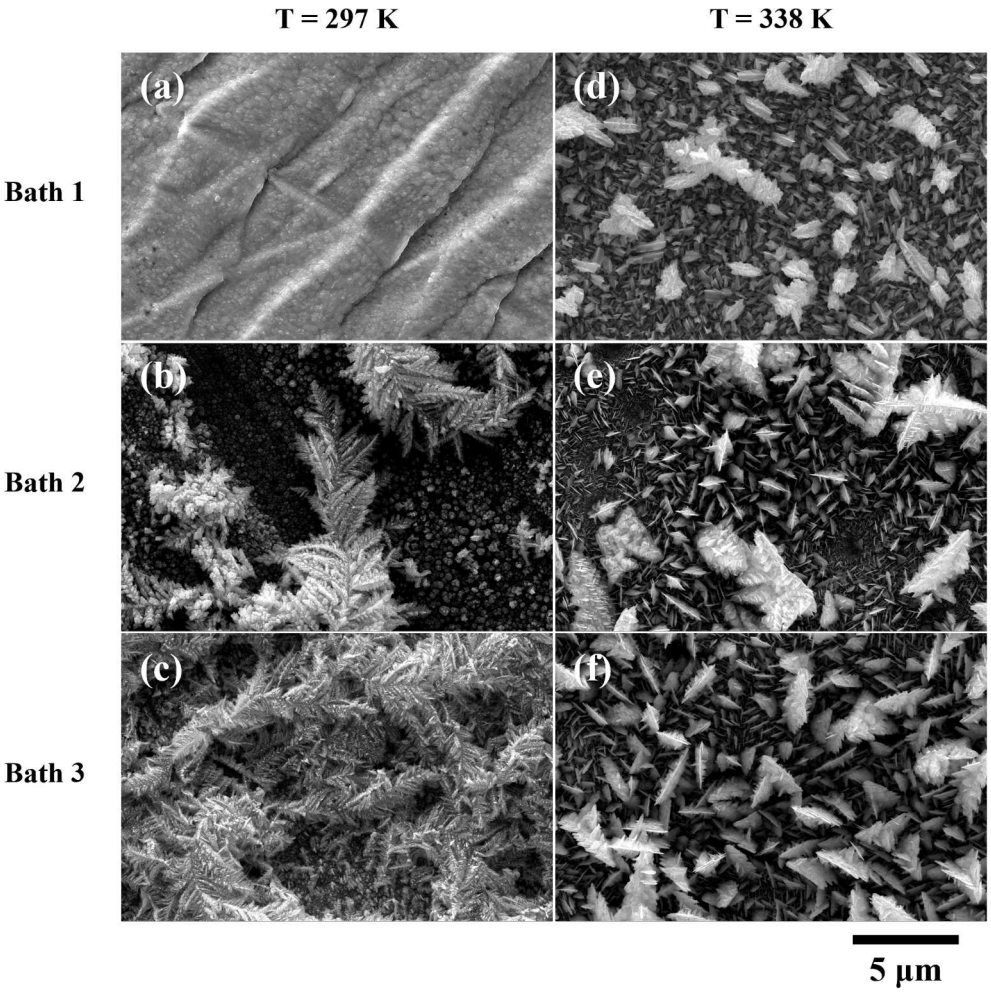

Fig. 2. SEM micrographs of Sb electrodeposits onto Pt electrode obtained at 297 K (a-c) and 338 K (d-f) in baths 1, 2 and 3 containing 0.05 mol L^{-1} $SbCl_3$, and under potentiostatic control at (a) –0.35 V, (b) –0.33 V, (c) –0.30 V, (d) –0.29 V, (e) –0.27 V and at (f) –0.24 V for 1800 s.

temperature and water content are increased. Therefore, the change in the surface morphology of the Sb electrodeposits with water and temperature is attributed to the improvement in the electrodeposition rate of the Sb electrodeposits related to the increase of both water and temperature.

The X-ray diffraction was accomplished to investigate the effect of water content and temperature on the crystalline structure of Sb films. The Fig. 3(a-f) presents the diffraction patterns for the Sb electrodeposits on the Pt surface obtained in baths 1, 2 and 3, at 297 and 338 K. For diffractograms of Fig. 3(a-f), peaks referring to the Sb phase of the rhombohedral crystal structure and space group (R-3mH, #166) at the 2θ positions of 27.57°, 29.29°, 33.45°, 49.15°, 56.92°, 57.00°, 60.73°, 70.26°, 74.74°, 81.87°, 90.81°, 91.57° and 92.07° were indexed. Additionally, Pt peaks referring to the substrate with the face-centered cubic crystal structure (FCC) and space group (Fm-3 m, #225) at the 2θ positions of 46.57°, 54.29°, 80.32° and 98.26° were indexed. The phases of Sb and Pt were identified according to the patterns of ICDD #01–085-1323 and #01–087-0646 card files, respectively. No peaks resulting from contaminations were identified. Fig. 3 shows the diffraction peaks from metallic Sb phases. It can be observed that there is an increase in the number of metallic Sb phases with the addition of water and an increase in the bath temperature. This may suggest that Sb electrodeposition was favoured under these conditions.

3.3. Computational results

The molecular dynamics simulations were carried out using the XTB software, and after ranking the energy of each frame, the frame with the lowest energy was selected. The geometry was then optimized at the DFT- PBE-D3BJ/Def2-TZVP level of theory for System (A) (0 H_2O); System (B) (3 H_2O); System (C) (5 H_2O); System (D) (10 H_2O); and System (E) (15 H_2O) as can be seen in Fig. 4. The simulations work using the molecular dynamics approach tries to carry out its approach with the most faithful numbers of atoms and molecules possible in a box of nanometric dimensions, with numbers of atoms of approximately tens of thousands of units, in a molecular dynamic simulation box [33,37,57]. The simulation of a system is limited and is generally chosen through a relationship between precision and computational cost. An approach involving Density Functional Theory (DFT), such as in the simulation and prediction of material properties, as well as thermodynamic and electronic properties, depending on the levels of approximation and theory chosen, the maximum system size achieved is around 1000 atoms [58]. Increasing the size of the system is impractical due to the high cost associated with DFT (its computational cost is proportional to N^3). Applying a real system in reduced quantities, keeping the proper proportions of $SbCl_3$, ChCl, EG and H_2O, the number of atoms in the system is still around thousands of units. The configurations of the molecules and their respective conformations were obtained using the XTB and Molclus software, thus obtaining the best minimum energies for each system, and starting from this minimum energy conformation, the DFT

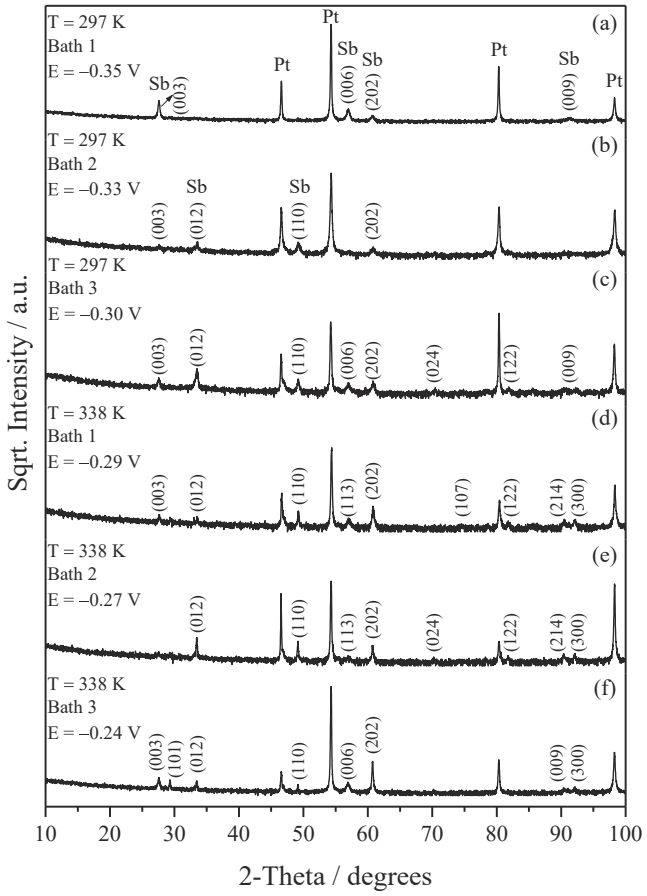

Fig. 3. X-ray diffraction pattern of Sb electrodeposits onto Pt electrode at 297 K (a-c) and 338 K (d-f) in baths 1, 2 and 3 containing 0.05 mol L^{-1} $SbCl_3$, obtained under potentiostatic control at (a) –0.35 V, (b) –0.33 V, (c) –0.30 V, (d) –0.29 V, (e) –0.27 V and at (f) –0.24 V for 1800 s.

Table 4
Electrodeposition potential (E_{dep}), electrodeposition charge (Q_{ed}) and mass of the electrodeposited Sb coating (m_{ed}) at different temperatures and water contents. The Sb electrodeposited mass values were, obtained from Faraday's Equation.

T / K	Water malar ratio in the plating solutions	E_{dep} / V	Q_{ec} / mC	m_{ed} / mg
297	0.00	− 0.35	2.98 ± 0.135	0.08 ± 0.060
	0.45	− 0.33	3.89 ± 0.063	0.11 ± 0.030
	1.62	− 0.30	5.61 ± 0.013	0.15 ± 0.006
338	0.00	− 0.29	34.89 ± 0.190	0.94 ± 0.080
	0.45	− 0.27	37.31 ± 0.120	1.00 ± 0.050
	1.62	− 0.24	39.32 ± 0.130	1.06 ± 0.050

calculations were carried out. Therefore, the aim was to apply a methodology that can describe a qualitative and approximate, but pioneering, result, applying a slight and gradual increase in the number of waters in the system to obtain a correlation of the effect of water in deep eutectic solvent (DES) for the Sb electrodeposition.

To represent each system's electronic reception (reduction), 1, 2 and 3 electrons were added, referring to the reduction of $Sb^{+3,}$ and their respective energies were calculated at the DFT level. The difference between the neutral system and the anion system gives us the electronic affinity of the system (Equation (1). Table 5 provides the data obtained for the VEA of the systems. Table 5 shows that the VEA of the systems increases as the number of waters increases, so the trend is towards adding 1, 2 and 3 electrons. Furthermore, Table 6 shows the ΔVEA (Equation (2), where the system without water is taken as a reference. Therefore, the inclusion of quantities of water in DES systems favours the electrodeposition of metals [33,35,59,60]. The model proposed by computational methods suggests an increase in the electron receptivity of the DES system with the addition of water due to the linear increase in ΔVEA with the increase in water in the system, compared to the system without water. The ΔVEA values for 1 electron are 14.50, 14.78, 22.25, and 24.84 kcal mol^{-1} for System B, C, D, and E, respectively (Table 6). The trend is also observed for 2 and 3 electrons reduction. The tendency for the electronic affinity of systems to increase with increasing water content so that antimony can be favored for electronic reception it may explain its contribution to adding water to favor the electrochemical reduction process of Sb^{3+}. In addition, the coefficient of determination (R^2) between ΔVEA and the number of water molecules added to the systems is shown in Fig. 5. The $R^2 = 0.822$ represents a good correlation between the increase in electron affinity and the increase in water molecules in the systems studied.

QTAIM is a mathematical approach in computational chemistry that aims to provide insights into the nature of chemical bonding and molecular properties. The central concept of QTAIM is using mathematical functions to analyse the electron density in a molecule, which allows the identification of critical points, such as bonding critical points, that define the location of chemical bonds [61]. This study deals only with the antimony cations (Sb^{+3}) critical bond points (BCP). The analysis was carried out using the parameters All-Electron density (ρ_b), Laplacian of the electron density ($\nabla^2\rho_b$) and Energy density (*Hb*). If the $\nabla^2\rho_b$ and Hb are less than zero, this indicates a strong covalent interaction between the antimony and the molecules in the system (EG, ChCl and water). On the other hand, if the values are more significant than zero, there is a weak electrostatic interaction between them. Notably, the interaction can be partially covalent when $\nabla^2\rho_b$ is more significant than zero, but H_b is less than zero [62]. The QTAIM analysis indicates that in all systems $\nabla^2\rho_b$ has a positive value and H_b has a negative value, indicating that the BCP interactions of the molecules in the system (EG, ChCl and water) around Sb^{3+} are partially covalent. Moreover, the electron density values (ρ_b) of the chlorine BCPs (BCPs 1, 2 and 3) have higher ρ_b values ($\approx 7 \times 10^{-2}$ a.u.) than the other interactions in BCPs 4, 5, 6 and 7 ($\approx 2 \times 10^{-2}$ a.u.) (see Tables S1-S5 in the Supplementary Material), as evidenced by the that the Sb-Cl bond lengths are closer than the others (Fig. 4), and, consequently, the Sb-Cl interaction is the stronger which suggest the formation of Sb-Cl bond. The $SbCl_3$ complex has an experimentally favourable formation constant, and possible bonds between EG and H_2O with the $SbCl_3$ complex can also be considered for the system [63–65]. However, the gradual addition of H_2O decreased the electronic density with Sb^{3+}, seen at 0.319 a.u. for System A (without H_2O), and there is a downward trend until 0.311 a.u. for System E (15 H_2O molecules) (see Tables S1-S5 in the Supplementary Material). Plotting the R^2 between the number of water molecules added and the sum of the electronic density ($\Sigma\rho_b$) shown in Fig. 6, we obtained a R^2 of 0.932, indicating a very good correlation. In addition, after the addition of 3 water molecules, shown in Fig. 7, there is a substitution of the bonds of the $SbCl_3$ complex with EG, being replaced by bonds with H_2O, and just as in the 10 H_2O system, there is another substitution of EG for H_2O, and maintaining these bonds with 15 water molecules of H_2O.

The QTAIM results obtained in this study may corroborate the efficiency of water in weakening the interaction of Sb^{3+} ions with the H_2O molecules in the system, thus facilitating its electrodeposition. This can be associated with a more easily displacement of the Sb^{3+} ions in the solution to be deposited on the electrode surface, corroborating the diffusion coefficient results. The idea of the QTAIM study is to associate the mobility of Sb^{3+} to electrodeposition, in which this lower electronic density due to the higher number of H_2O molecules would facilitate the ionic mobility.

The NCI study was carried out to ascertain each system's intermolecular interactions. Comparing each system, initially in the system without water (Fig. 8(a)), a greater amount of green isosurfaces was

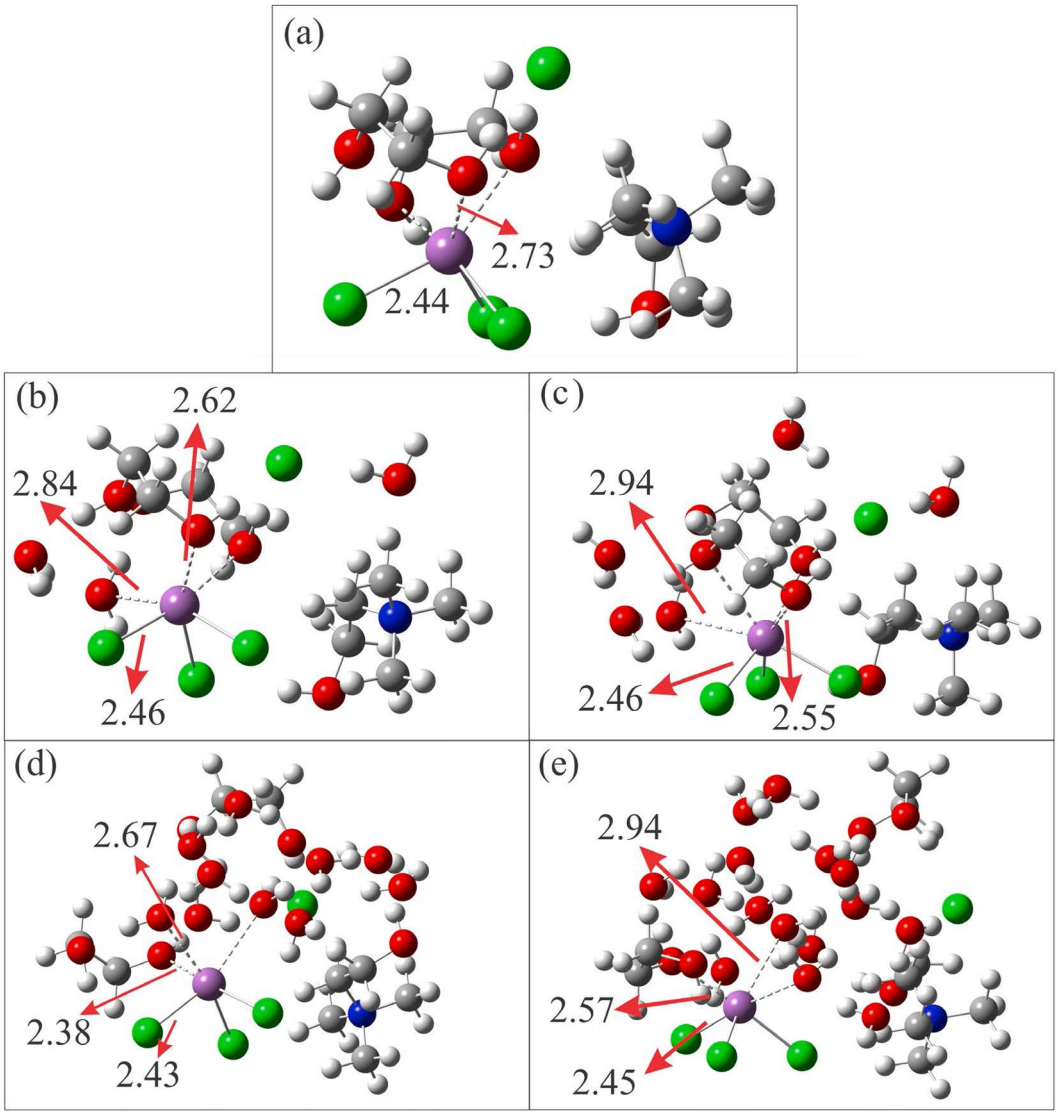

Fig. 4. Optimized geometries of the molecules of the system without H_2O molecules (a), 3 H_2O molecules (b), 5 H_2O molecules (c), 10 H_2O molecules (d), and 15 H_2O molecules (e). Bond lengths are in Angstroms.

Table 5
Absolute VEA values (in kcal/mol) for adding 1, 2 and 3 electrons in the system without H_2O molecules (A), 3 H_2O molecules (B), 5 H_2O molecules (C), 10 H_2O molecules (D), and 15 H_2O molecules (E).

System	VEA 1 e^-	VEA 2 e^-	VEA 3 e^-
A	−18.77	−109.44	−236.56
B	−4.27	−87.03	−223.60
C	−3.99	−79.12	−210.93
D	3.48	−65.38	−187.68
E	6.08	−54.64	−170.05

Table 6
Relative values for VEA (ΔVEA, in kcal/mol) for the addition of 1, 2 and 3 electrons in the system without H_2O molecules (A), 3 H_2O molecules (B), 5 H_2O molecules (C), 10 H_2O molecules (D), and 15 H_2O molecules (E).

System	ΔVEA 1 e^-	ΔVEA 2 e^-	ΔVEA 3 e^-
A	0	0	0
B	14.50	22.42	12.96
C	14.78	30.32	25.63
D	22.25	44.06	48.87
E	24.84	54.80	66.51

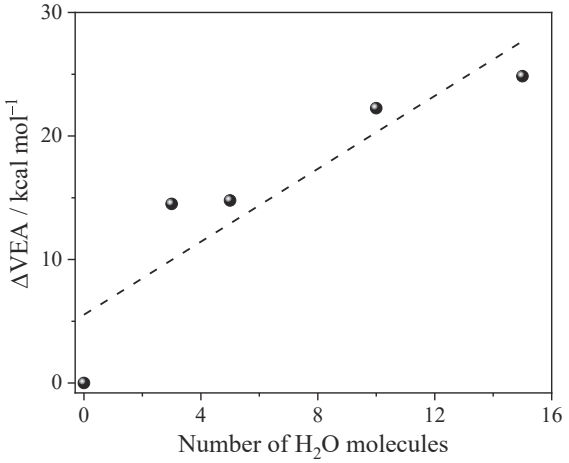

Fig. 5. Plot of ΔVEA (in kcal/mol) in function of the number of H_2O molecules.

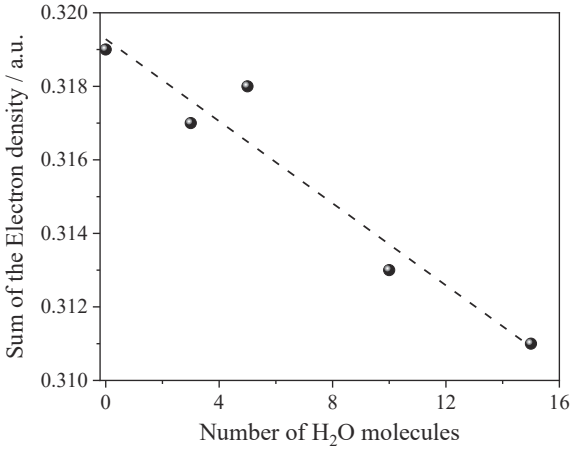

Fig. 6. Plot of sum of the electronic density ($\Sigma\rho_b$) in function of the number of H_2O molecules.

observed, indicating a predominance of Van der Waals forces. With the addition of H_2O to the systems Fig. 8(b), Fig. 8(c), Fig. 8(d) and Fig. 8(e), the most significant number of strong intermolecular interactions is highlighted by the blue density, following an upward trend up to system E (Fig. 8(e)). This is related to the addition of intermolecular interactions of the hydrogen bond type carried out by H_2O - H_2O and H_2O - HO in EG [62]. In addition, H_2O carries out moderate-strength Van der Waals-type interactions with the $SbCl_3$ complex in systems D (Fig. 8(d)) and E (Fig. 8(e)). The increase in H_2O also ensures an increase in the number of strong interactions with the Cl^- ion in DES.

The Cl^- ion performs strong interactions in the system, being related to its negative charge, interacting with the partially positive hydrogens of the hydroxyls of EG (Fig. 8(a)), remaining with the addition of H_2O. The DES urea molecule has moderate Van der Waals interactions in all systems. The map of RDG vs. (λ_2) ρ on the X and Y axes, respectively, Fig. 9, indicates a decrease in the repulsive effect with increasing H_2O, represented with red dots highlighted in the yellow circles, with a higher density of points up to 0. 015 a.u (Fig. 9(a)), the density decreasing with an increase of 3 H_2O (Fig. 9(b)), remaining at an increase of 5 and 10 H_2O (Fig. 9(c-d)), reaching a minimum of 0.010 a.u. at 15 H_2O (Fig. 9

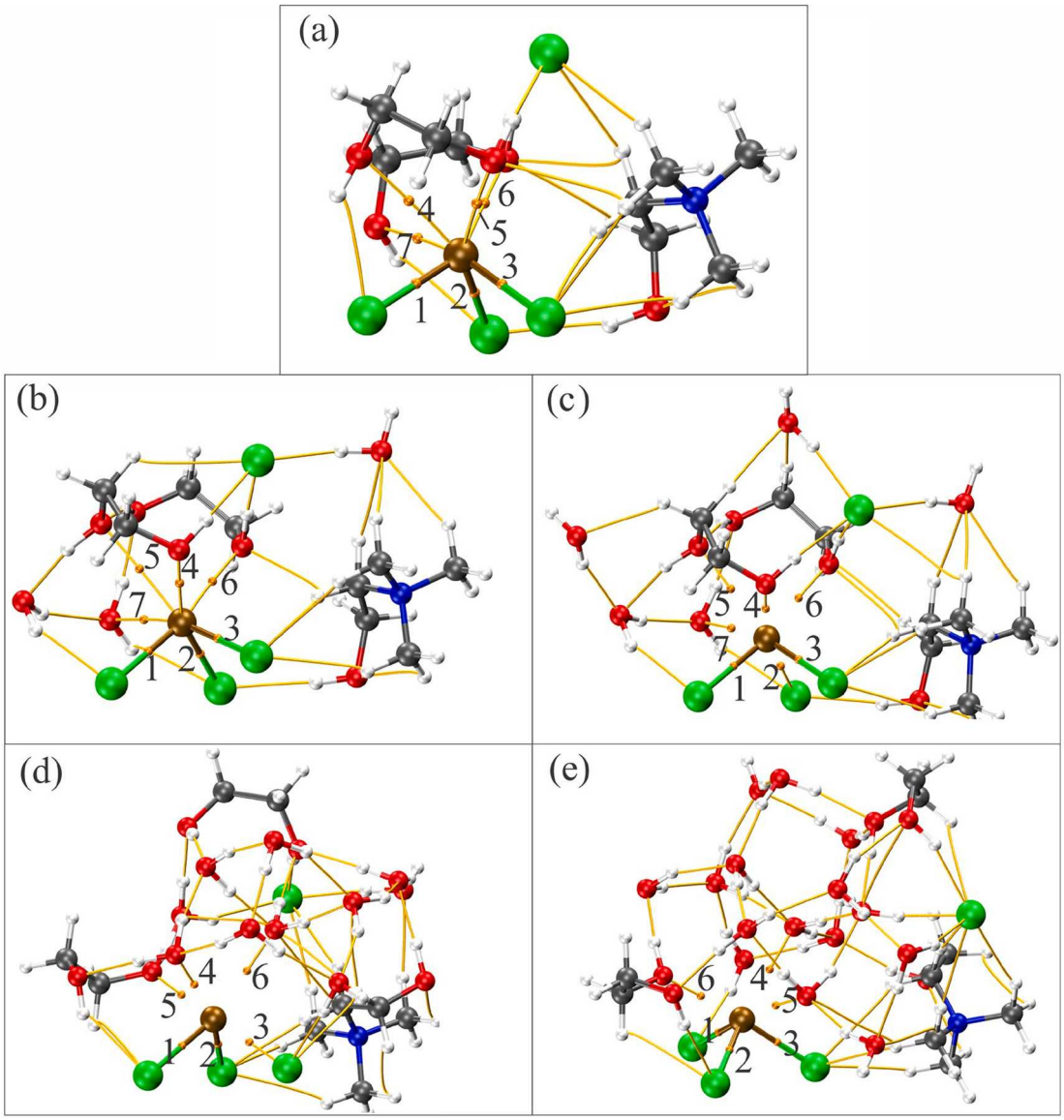

Fig. 7. The molecular graphs Sb^{3+} BCPs of the studied system without H_2O molecules (a), 3 H_2O molecules (b), 5 H_2O molecules (c), 10 H_2O molecules (d), and 15 H_2O molecules (e) were obtained by QTAIM analysis.

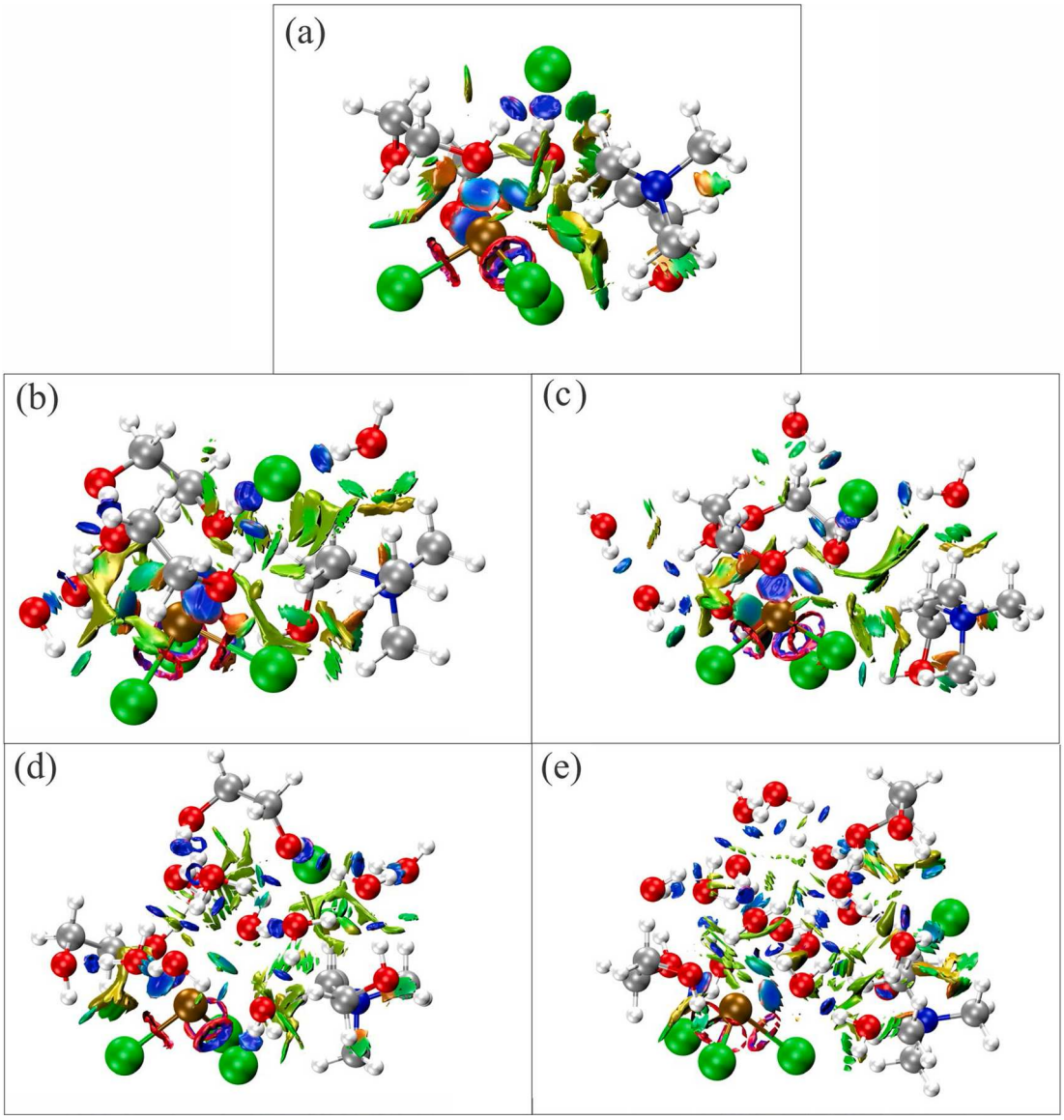

Fig. 8. RDG isosurface for Intermolecular interactions for molecules of the system without H_2O molecules (a), 3 H_2O molecules (b), 5 H_2O molecules (c), 10 H_2O molecules (d), and 15 H_2O molecules (e).

(d)). There was also an increase in the strong intermolecular effect, represented with blue dots highlighted in the purple circles, with a higher density of dots at − 0.040 a.u (Fig. 9(a)), with the density increasing to − 0.045 a.u. with an increase of 3 H_2O (Fig. 9(b)), remaining at an increase of 5 H_2O (Fig. 9(c)), reaching a maximum of value − 0.050 a.u., in the system with 10 and 15 H_2O with RDG 0.2 (Fig. 9(d-e)).

4. Conclusions

The eutectic mixture based on choline chloride-ethylene glycol in the absence and presence of water was successfully used in this study for electrodeposition of Sb on Pt surface at 297 K and 338 K without the necessity to add complex additives. The cyclic voltammogram performed on the Pt electrode of the electrolyte solution containing the Sb^{3+} showed, in the direct scan, a well-defined cathode peak corresponding to the reduction of Sb^{3+}/Sb. SEM analysis showed similar dendritic morphologies for Sb films obtained with water addition at 297 K. Meanwhile, sheet structures for all Sb films at 338 K were obtained. Finally, XRD characterization revealed that the Sb electrodeposits had a rhombohedral crystalline structure with pure phases for all samples. The DFT simulations for DES and $SbCl_3$ systems without H_2O and with varying amounts of H_2O molecules favoured the system in increasing electron affinity. Furthermore, there was a strong tendency for H_2O to be added, causing a decrease in the electronic density of the Sb^{3+} ions with the atoms in all the studied systems. These results indicated a possible explanation for electrodeposition being favoured in this type of system's presence of H_2O molecules. This work is also expected to serve as a basis for obtaining Sb films with varied structures with promising properties and potential applications in the wide range of uses of Sb and its alloys. Lastly, the quantum computational simulations indicated that the Sb-Cl interaction is stronger, which suggests the formation of Sb-Cl complexes and that the addition of water molecules favours the electron affinity of the systems, and QTAIM results suggested that this additive decreased the electron density of Sb^{3+} ions.

CRediT authorship contribution statement

Ana Aline C. Alcanfor: Writing – review & editing, Writing – original draft, Visualization, Validation, Methodology, Investigation, Formal

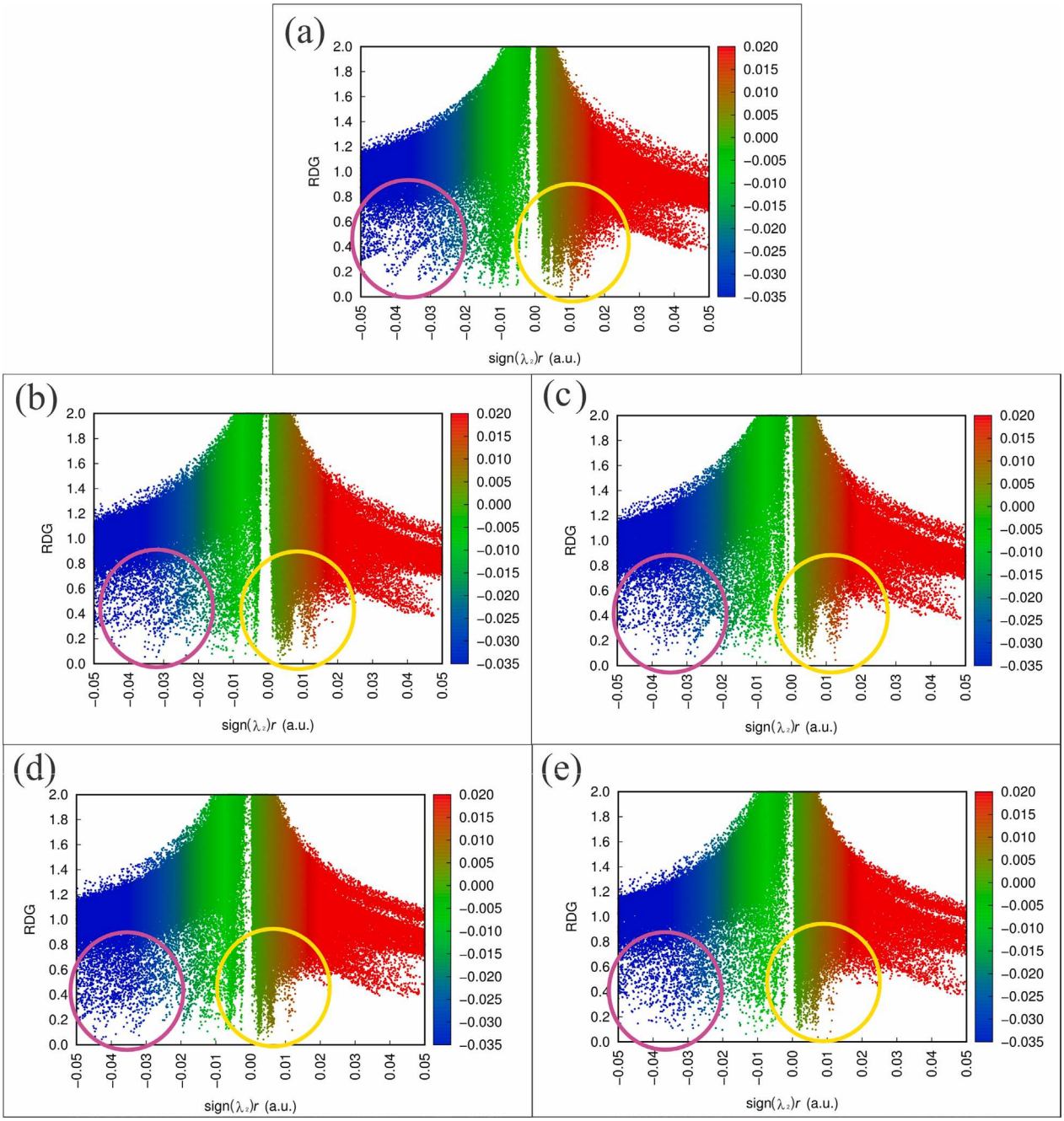

Fig. 9. RDG vs. sign(λ_2)ρ from the results of the NCI of the molecules of the system without H_2O molecules (a), 3 H_2O molecules (b), 5 H_2O molecules (c), 10 H_2O molecules (d), and 15 H_2O molecules (e).

analysis. **Leonardo P. da Silva:** Writing – review & editing, Writing – original draft, Visualization, Validation, Methodology, Investigation, Formal analysis. **Raíssa C. de Oliveira:** Validation, Methodology, Investigation. **Gabrielle A. Paulo:** Validation, Methodology, Investigation. **Camila P. Sousa:** Supervision, Methodology, Conceptualization. **Othon S. Campos:** Writing – review & editing, Validation, Supervision, Formal analysis, Data curation. **Diego F. Dias:** Resources, Investigation, Formal analysis. **Filipe X. Feitosa:** Resources. **Hosiberto B. de Sant'Ana:** Resources. **Norberto K.V. Monteiro:** Conceptualization, Data curation, Formal analysis, Funding acquisition, Methodology, Project administration, Resources, Supervision, Validation, Visualization, Writing – original draft, Writing – review & editing, Writing – original draft, Visualization, Validation, Supervision, Resources, Project administration, Methodology, Funding acquisition, Formal analysis, Data curation, Conceptualization. **Adriana N. Correia:** Writing – review & editing, Writing – original draft, Visualization, Validation, Supervision, Resources, Project administration, Methodology, Funding acquisition, Formal analysis, Data curation, Conceptualization. **Pedro de Lima-Neto:** Writing – review & editing, Supervision, Resources, Investigation, Funding acquisition.

Declaration of competing interest

The authors declare that they have no known competing financial interests or personal relationships that could have appeared to influence the work reported in this paper.

Data availability

No data was used for the research described in the article.

Acknowledgements

This study was financed in part by the Coordenação de Aperfeiçoamento de Pessoal de Nível Superior - Brasil (CAPES) – Finance Code 001. The authors thank the financial support given by the following Brazilian funding agencies: Coordenação de Aperfeiçoamento de Pessoal de Nível Superior (CAPES), Conselho Nacional de Desenvolvimento Científico e Tecnológico (CNPq) and Fundação Cearense de Apoio ao Desenvolvimento Científico e Tecnológica (FUNCAP). A.N. Correia gratefully acknowledges the funding provided by CNPq (proc. 305103/2022-9). P. de Lima-Neto thanks the financial support received from CNPq (proc. 302825/2022-3). Ana. A. C. Alcanfor thanks CAPES for her grants. The authors thank the Central Analítica-UFC/CT-INFRA/MCTI-SISANO/Pró-Equipamentos CAPES and Laboratório de Raios-X (UFC) for their support. The authors also thank Centro Nacional de Processamento de Alto Desempenho (CENAPAD) of the Federal University of Ceará (UFC) for providing computational resources.

Appendix A. Supplementary data

Supplementary data to this article can be found online at https://doi.org/10.1016/j.molliq.2024.124416.

References

[1] A.W. Black, W. Zhang, Y.J. Noori, G. Reid, P.N. Bartlett, Temperature effects on the electrodeposition of semiconductors from a weakly coordinating solvent, J. Electroanal. Chem. 944 (2023) 117638, https://doi.org/10.1016/j.jelechem.2023.117638.

[2] S. Cho, J. Lim, Y. Seo, Fabrication of bismuth-antimony-telluride alloy/poly(3,4-ethylenedioxythiophene) hybrid films for thermoelectric applications at room temperature by a simple electrochemical process, Chem. Mater. 35 (2023) 3196–3205, https://doi.org/10.1021/acs.chemmater.3c00001.

[3] F.W.S. Lucas, F.H.B. Lima, Electrodeposited tin-antimony alloys as novel electrocatalysts for selective and stable carbon dioxide reduction to formate, ChemElectroChem 7 (2020) 3733–3742, https://doi.org/10.1002/celc.202000769.

[4] K. Nieto, D.S. Windsor, A.R. Kale, J.R. Gallawa, D.A. Medina, A.L. Prieto, Structural control of electrodeposited sb anodes through solution additives and their influence on electrochemical performance in na-ion batteries, J. Phys. Chem. c. (2023), https://doi.org/10.1021/acs.jpcc.3c01086.

[5] H.R. Shen, X.Y. Han, X.M. Zheng, B. Muniyandi, J.K. Wang, Q.L. Kang, M.G. Chen, Q. Wu, P.Y. Zhang, One-step electrochemical synthesis and optimization of sb-co-P alloy anode for sodium ion battery, Electrochim. Acta. 438 (2023) 141529, https://doi.org/10.1016/j.electacta.2022.141529.

[6] H. Jung, N.V. Myung, Electrodeposition of antimony telluride thin films from acidic nitrate-tartrate baths, Electrochim. Acta. 56 (2011) 5611–5615, https://doi.org/10.1016/j.electacta.2011.04.010.

[7] J. Schoenleber, N. Stein, C. Boulanger, Influence of tartaric acid on diffusion coefficients of BiIII, SbIII, TeIV in aqueous medium: application of electrodeposition of thermoelectric films, J. Electroanal. Chem. 724 (2014) 111–117, https://doi.org/10.1016/j.jelechem.2014.04.004.

[8] V.A. Majidzade, P.H. Guliyev, A.S. Aliyev, M. Elrouby, D.B. Tagiyev, Electrochemical characterization and electrode kinetics for antimony electrodeposition from its oxychloride solution in the presence of tartaric acid, J. Mol. Struct. 1136 (2017) 7–13, https://doi.org/10.1016/j.molstruc.2017.01.082.

[9] Y. Lin, P. Ning, Y. Cui, C. Zhang, M. Xu, P. Dong, Z. Zhou, Y. Zhang, Electrodeposition behaviour of antimony in H2SO4-NH4F-SbF3 solutions, Int. J. Electrochem. Sci. 14 (2019) 4003–4019, https://doi.org/10.20964/2019.03.33.

[10] L. Hernández-Pérez, J. Carrillo-Abad, V. Pérez-Herranz, M.T. Montañés, M. C. Martí-Calatayud, Effluents from the copper electrorefining as a secondary source of antimony: role of mass transfer on the recovery by electrodeposition, Desalination 549 (2023), https://doi.org/10.1016/j.desal.2022.116322.

[11] W. Liu, T.Z. Yang, Q.H. Zhou, D.C. Zhang, C.M. Lei, Electrodeposition of SB(III) in alkaline solutions containing xylitol, Trans. Nonferrous Met. Soc. China (english Ed. 22 (2012) 949–957, https://doi.org/10.1016/S1003-6326(11)61269-7.

[12] Q. Wang, Y. Wang, Fundamental electrochemical behavior of antimony in alkaline solution, J. Sustain. Metall. 5 (2019) 606–616, https://doi.org/10.1007/s40831-019-00253-7.

[13] L. Hernández-Pérez, J. Carrillo-Abad, E.M. Ortega, V. Pérez-Herranz, M. T. Montañés, M.C. Martí-Calatayud, Voltammetric and electrodeposition study for the recovery of antimony from effluents generated in the copper electrorefining process, J. Environ. Chem. Eng. 11 (2023), https://doi.org/10.1016/j.jece.2022.109139.

[14] M.H. Yang, I.W. Sun, Electrodeposition of antimony in a water-stable 1-ethyl-3-methylimidazolium chloride tetrafluoroborate room temperature ionic liquid, J. Appl. Electrochem. 33 (2003) 1077–1084, https://doi.org/10.1023/A:1026223314259.

[15] W. Yang, H. Cang, Y. Tang, J. Wang, Y. Shi, Electrodeposition of tin and antimony in 1-ethyl- 3-methylimidazolium tetrafluoroborate ionic liquid, J. Appl. Electrochem. 38 (2008) 537–542, https://doi.org/10.1007/s10800-007-9470-6.

[16] Y.-T. Hsieh, Y.-C. Chen, I.-W. Sun, 1-Butyl-1-methylpyrrolidinium dicyanamide room temperature ionic liquid for electrodeposition of antimony, J. Electrochem. Soc. 163 (2016) D188–D193, https://doi.org/10.1149/2.0051606jes.

[17] Y.T. Hsieh, Y.C. Liu, N.C. Lo, W.J. Lin, I.W. Sun, Electrochemical co-deposition of gallium and antimonide from the 1-butyl-1-methylpyrrolidinium dicyanamide room temperature ionic liquid, J. Electroanal. Chem. 832 (2019) 48–54, https://doi.org/10.1016/j.jelechem.2018.10.034.

[18] R. Bernasconi, G. Panzeri, A. Accogli, F. Liberale, L. Nobili, L. Magagnin, Electrodeposition from deep eutectic solvents, Intech Prog. Dev. Lon. Liq. (2017) 235–261.

[19] A.P. Abbott, Deep eutectic solvents and their application in electrochemistry, Curr. Opin. Green Sustain. Chem. 36 (2022) 100649, https://doi.org/10.1016/j.cogsc.2022.100649.

[20] M.L. Mares, F. Golgovici, T. Visan, RDE voltammetry and impedance spectroscopy studies of sb, Te and SbTe Electrodeposition from Choline Chloride - Urea Ionic Liquids, Chalcogenide Lett. 10 (2013) 259–272.

[21] A.C. Rastogi, N.R. Janardhana, Properties of CuSbS2 thin films electrodeposited from ionic liquids as p-type absorber for photovoltaic solar cells, Thin Solid Films 565 (2014) 285–292, https://doi.org/10.1016/j.tsf.2014.06.031.

[22] A.S. Catrangiu, I. Sin, P. Prioteasa, A. Cotarta, A. Cojocaru, L. Anicai, T. Visan, Studies of antimony telluride and copper telluride films electrodeposition from choline chloride containing ionic liquids, Thin Solid Films 611 (2016) 88–100, https://doi.org/10.1016/j.tsf.2016.04.030.

[23] Z. Su, C. Xu, Y. Hua, J. Li, J. Ru, M. Wang, L. Xiong, Y. Zhang, Electrochemical preparation of sub-micrometer sn-sb alloy powder in ChCl-EG deep eutectic solvent, Int. J. Electrochem. Sci. 11 (2016) 3325–3338, https://doi.org/10.20964/110446.

[24] N. Su, S. Guo, F. Li, D. Liu, B. Li, Electrodeposition of p-type Sb2Te3 films and micro-pillar arrays in a multi-channel glass template, Materials (basel). 11 (2018), https://doi.org/10.3390/ma11071194.

[25] J. Bu, J. Ru, Z. Wang, Y. Hua, C. Xu, Y. Zhang, Y. Wang, Controllable preparation of antimony powders by electrodeposition in choline chloride-ethylene glycol, Adv. Powder Technol. 30 (2019) 2859–2867, https://doi.org/10.1016/j.apt.2019.06.027.

[26] Y. Sun, S. Cheng, Z. Mao, Z. Lin, X. Ren, Z. Yu, High electrochemical activity of a Ti/SnO2–Sb electrode electrodeposited using deep eutectic solvent, Chemosphere 239 (2020) 124715, https://doi.org/10.1016/j.chemosphere.2019.124715.

[27] J. Bu, J. Ru, Y. Hua, Z. Wang, Y. Zhang, X. Geng, W. Zhang, Electrochemical behavior of SB(III)/SB during the preparation of sb particles in deep eutectic solvent, Ionics (kiel) 27 (2021) 3119–3127, https://doi.org/10.1007/s11581-021-04048-3.

[28] Z. Zhang, Z. Wang, Y. Sun, S. Jiang, L. Shi, Q. Bi, J. Xue, Preparation of a novel Ni/Sb co-doped Ti/SnO2 electrode with carbon nanotubes as growth template by electrodeposition in a deep eutectic solvent, J. Electroanal. Chem. 911 (2022) 116225, https://doi.org/10.1016/j.jelechem.2022.116225.

[29] S. Liu, Z. Tan, J. Wu, B. Mao, J. Yan, Electrochemical interfaces in ionic liquids/deep eutectic solvents incorporated with water: a review, Electrochem. Sci. Adv. (2022) 1–9, https://doi.org/10.1002/elsa.202100199.

[30] A.Y.M. Al-Murshedi, J.M. Hartley, A.P. Abbott, K.S. Ryder, Effect of water on the electrodeposition of copper on nickel in deep eutectic solvents, Trans. Inst. Met. Finish. 97 (2019) 321–329, https://doi.org/10.1080/00202967.2019.1671062.

[31] P.E. Valverde, T.A. Green, S. Roy, Effect of water on the electrodeposition of copper from a deep eutectic solvent, J. Appl. Electrochem. 50 (2020) 699–712, https://doi.org/10.1007/s10800-020-01408-1.

[32] M. Lukaczynska, E.A. Mernissi Cherigui, A. Ceglia, K. Van Den Bergh, J. De Strycker, H. Terryn, J. Ustarroz, Influence of water content and applied potential on the electrodeposition of ni coatings from deep eutectic solvents, Electrochim. Acta. 319 (2019) 690–704, https://doi.org/10.1016/j.electacta.2019.06.161.

[33] J.R. Bezerra-Neto, L.L. Bezerra, N.G. Sousa, L.P.M. dos Santos, E.S. Marinho, N.K. V. Monteiro, A.N. Correia, P. de Lima-Neto, Molecular approach about the effect of water on the electrochemical behaviour of Ag+ ions in urea-choline chloride-water mixture, J. Mol. Model. 26 (2020), https://doi.org/10.1007/s00894-020-04587-y.

[34] Q. Xiang, C. Xu, X. Chen, S. Wang, J. Lu, J. Li, Y. Hua, Effect of water on electrodeposition behavior of zinc in a ChCl-urea-ZnO deep eutectic system, J. Solid State Electrochem. 26 (2022) 2353–2363, https://doi.org/10.1007/s10008-022-05250-7.

[35] J.R. Bezerra-Neto, N.G. Sousa, L.P.M. Dos Santos, A.N. Correia, P. De Lima-Neto, The effect of water on the physicochemical properties of an ethylene glycol and choline chloride mixture containing Cu2+ ions: electrochemical results and dynamic molecular simulation approach, Phys. Chem. Chem. Phys. 20 (2018) 9321–9327, https://doi.org/10.1039/c7cp05911f.

[36] S. Rozas, M. Atilhan, S. Aparicio, A density functional theory based tight-binding study on the water effect on nanostructuring of choline chloride + ethylene glycol deep eutectic solvent, J. Chem. Phys. 156 (2022), https://doi.org/10.1063/5.0091665.

[37] D.M.L. Pinheiro, L.L. Bezerra, A.A.C. Alcanfor, F.X. Feitosa, N.K.V. Monteiro, A. N. Correia, P. de Lima Neto, H.B. de Sant'Ana, Ag+ ion in choline chloride and

glycerol mixture: evaluation of electrochemical properties and molecular modelling approaches, J. Mol. Liq. 371 (2023) 121053, https://doi.org/10.1016/j.molliq.2022.121053.
[38] A.P. Abbott, D. Boothby, G. Capper, D.L. Davies, R.K. Rasheed, Deep eutectic solvents formed between choline chloride and carboxylic acids : versatile alternatives to ionic liquids, J. Am. Chem. Soc. 126 (2004) 9142–9147.
[39] C. Bannwarth, S. Ehlert, S. Grimme, GFN2-xTB - an accurate and broadly parametrized self-consistent tight-binding quantum chemical method with multipole electrostatics and density-dependent dispersion contributions, J. Chem. Theory Comput. 15 (2019) 1652–1671, https://doi.org/10.1021/acs.jctc.8b01176.
[40] T. Lu, Molclus program, Beijing Kein Res, Cent, Nat. Sci. China (2016).
[41] F. Weigend, R. Ahlrichs, Balanced basis sets of split valence, triple zeta valence and quadruple zeta valence quality for H to rn: design and assessment of accuracyElectronic supplementary information (ESI) available:[DETAILS]. see https://doi.org/10.1039/b508541a, Phys. Chem. Chem. Phys. 7 (2005) 3297–3305.
[42] F. Weigend, Accurate coulomb-fitting basis sets for H to rn, Phys. Chem. Chem. Phys. 8 (2006) 1057–1065, https://doi.org/10.1039/b515623h.
[43] F. Neese, Software update: the ORCA program system, version 4.0, Wiley Interdiscip, Rev. Comput. Mol. Sci. 8 (2018) 1–6, https://doi.org/10.1002/wcms.1327.
[44] F. Neese, F. Wennmohs, U. Becker, C. Riplinger, The ORCA quantum chemistry program package, J. Chem. Phys. 152 (2020), https://doi.org/10.1063/5.0004608.
[45] A.P. Gaiduk, T.A. Pham, M. Govoni, F. Paesani, G. Galli, Electron affinity of liquid water, Nat. Commun. 9 (2018) 4–9, https://doi.org/10.1038/s41467-017-02673-z.
[46] Y. Takahata, D.P. Chong, Density-functional calculations of molecular electron affinities, J. Braz. Chem. Soc. 10 (1999) 354–358, https://doi.org/10.1590/S0103-50531999000500003.
[47] R.F.W. Bader, S.G. Anderson, A.J. Duke, Quantum topology of molecular charge distributions, J. Am. Chem. Soc. 101 (1979) 1389–1395, https://doi.org/10.1021/ja00500a006.
[48] C.F. Matta, R.J. Boyd, An Introduction to the Quantum Theory of Atoms in Molecules, 2007. https://doi.org/10.1002/9783527610709.ch1.
[49] T. Lu, F. Chen, Multiwfn: a multifunctional wavefunction analyzer, J. Comput. Chem. 33 (2012) 580–592, https://doi.org/10.1002/jcc.22885.
[50] W. Humphrey, A. Dalke, K. Schulten, Sartorius products, J. Mol. Graph. 14 (1996) 33–38. https://www.tapbiosystems.com/tap/products/index.htm.
[51] L. Vieira, R. Schennach, B. Gollas, The effect of the electrode material on the electrodeposition of zinc from deep eutectic solvents, Electrochim. Acta. 197 (2016) 344–352, https://doi.org/10.1016/j.electacta.2015.11.030.
[52] J.M. Hartley, C.-M. Ip, G.C.H. Forrest, K. Singh, S.J. Gurman, K.S. Ryder, A. P. Abbott, G. Frisch, EXAFS study into the speciation of metal salts dissolved in ionic liquids and deep eutectic solvents, Inorg. Chem. 53 (2014) 6280–6288, https://doi.org/10.1021/ic500824r.
[53] E.H. Oelkers, D.M. Sherman, K.V. Ragnarsdottir, C. Collins, An EXAFS spectroscopic study of aqueous ANTIMONY(III)-chloride complexation at temperatures from 25 to 250°C, Chem. Geol. 151 (1998) 21–27, https://doi.org/10.1016/S0009-2541(98)00067-9.
[54] A.L. Pitman, M. Pourbaix, N. de Zoubov, Potential-pH diagram of the antimony-water system, J. Electrochem. Soc. 104 (1957) 594, https://doi.org/10.1149/1.2428423.
[55] D. Rajska, A. Brzózka, K.E. Hnida-Gut, G.D. Sulka, Investigation of electrodeposition kinetics of in, sb, and zn for advanced designing of InSb and ZnSb thin films, J. Electroanal. Chem. 882 (2021), https://doi.org/10.1016/j.jelechem.2020.114967.
[56] S. Wei, M. Zhang, W. Han, Y. Yan, Y. Xue, M. Zhang, B. Zhang, Electrochemical behavior of antimony and electrodeposition of mg-li-sb alloys from chloride melts, Electrochim. Acta. 56 (2011) 4159–4166, https://doi.org/10.1016/j.electacta.2011.01.104.
[57] L. Amorim, R.V. de Oliveira, L.L. Bezerra, L.P. Coutinho, P.B.A. Fechine, A. N. Correia, Á.R.L. da Silva, P. de Lima-Neto, N.K.de V. Monteiro, Analysis of Fe2+ and Mn2+ ions in DES and water: a theoretical study using molecular dynamic simulations, QTAIM and NCI-RDG, Colloids Surfaces A Physicochem. Eng. Asp. 674 (2023) 131818, https://doi.org/10.1016/j.colsurfa.2023.131818.
[58] T. Müller, S. Sharma, E.K.U. Gross, J.K. Dewhurst, Extending solid-state calculations to ultra-long-range length scales, Phys. Rev. Lett. 125 (2020) 256402, https://doi.org/10.1103/PhysRevLett.125.256402.
[59] C. Ma, A. Laaksonen, C. Liu, X. Lu, X. Ji, The peculiar effect of water on ionic liquids and deep eutectic solvents, Chem. Soc. Rev. 47 (2018) 8685–8720, https://doi.org/10.1039/c8cs00325d.
[60] J. Zhao, G. Gorbatovski, O. Oll, E. Anderson, E. Lust, Influence of water on the electrochemical characteristics and nanostructure of Bi(hkl)|Ionic liquid interface, Electrochim. Acta. 415 (2022) 140263, https://doi.org/10.1016/j.electacta.2022.140263.
[60] R.F.W. Bader, J.R. Cheeseman, K.E. Laidig, K.B. Wiberg, C. Breneman, Origin of rotation and inversion barriers, J. Am. Chem. Soc. 112 (1990) 6530–6536, https://doi.org/10.1021/ja00174a012.
[62] I. Rozas, I. Alkorta, J. Elguero, Behavior of ylides containing N, O, and C atoms as hydrogen bond acceptors, J. Am. Chem. Soc. 122 (2000) 11154–11161, https://doi.org/10.1021/ja0017864.
[63] G. Li, Y. Xin, X. Lü, Q. Tian, K. Yan, L. Ye, Stability constants of Sb5+ with Cl− and thermodynamics of Sb−S−Cl−H2O system involving complex behavior of sb with cl, Trans. Nonferrous Met. Soc. China. 30 (2020) 3379–3389, https://doi.org/10.1016/S1003-6326(20)65469-3.
[64] Z. Su, Electrochemical preparation of sub-micrometer sn-sb alloy powder in ChCl-EG deep eutectic solvent, Int. J. Electrochem. Sci. (2016) 3325–3338, https://doi.org/10.20964/110446.
[65] E. Rudnik, M. Kostępski, Comparative studies on the codeposition of antimony and tin from acidic chloride and sulfate-chloride solutions, Arch. Metall Mater (2018), https://doi.org/10.24425/122397.